学位論文

Development of Methods for Fluorescence Imaging and Analysis of Mitochondria-mediated Cell Death

（ミトコンドリアを介する細胞死の蛍光イメージングと解析法の開発）

平成 25 年 12 月　博士（理学）申請

東京大学大学院理学系研究科化学専攻

那須　雄介

Acknowledgements

The present thesis was completed under a supervision of Prof. Takeaki Ozawa, Department of Chemistry, School of Science, The University of Tokyo. I would like to express my sincere appreciation for his constant support and guidance throughout my doctor course.

I would like to thank all committee members, Prof. Keisuke Goda, Prof. Mitsuhiko Shionoya, Prof. Naokazu Kano and Prof. Moritoshi Sato, for their patient readings of this dissertation and insightful advice on it.

My thanks as well go to Dr. Yoichi Asaoka, Ms. Misako Namae and Prof. Hiroshi Nishina in Tokyo Medical and Dental University for extensive instruction on *in vivo* experiments.

I would like to express my gratitude to Dr. Go J. Yoshida, Dr. Satoko Arakawa and Prof. Shigeomi Shimizu in Tokyo Medical and Dental University for their valuable suggestions, and helps throughout the present work. The helpful discussion with them was indispensable for starting and enabling this work.

My deep appreciation goes to Dr. Alexander Benke and Prof. Suliana Manley in École Polytechnique Fédérale de Lausanne, who kindly offered discussions and instructions on technique of super-resolution imaging.

My special thanks are due to all members of Analytical Chemistry laboratory for their stimulating discussion in various fields of science. I especially appreciate Dr. Mitsuru Hattori for productive discussion, Mr. Naoshi Hattori for a lot of instructions in experiments, Dr. Rintaro Shimada for quantitative data analysis, Dr. Lingzhi Yang for giving kind advice throughout my doctor course, Mr. Genki Kawamura for contribution to my project, Dr. Hideaki Yoshimura for instruction of figure presentation and my junior students for administration of laboratory. In addition, helpful assists by Mr. Osamu Takenouchi, Dr. Yoshihiro Katsura, Ms. Maki Komiya and Mr. Tomoya Kojima activates my motivation for completing my projects.

Finally, I thank my family for their sincere supports to accomplish this work successfully.

Abstract

Microscopy is a methodology to observe objects of interest with microscope. To date, microscopy have provided us information on specific phenomena in diverse fields of science. Recently, the importance of "*in vivo*" and "super-resolution" imaging with microscopy have been discussed. "*In vivo*" imaging indicates a visualization of targets for less-invasively analyzing live animals. Microscopy requires a sample preparation, such as fixation and embedding, for imaging targets, perturbing the physiological condition of biological sample. Microscopy capable of "*in vivo*" imaging offers a deeper understanding of the universe in organisms. To further elucidate biological phenomena, a spatial resolution in microscopy is of particular interest. "Super-resolution" imaging is an emerging technique to achieve a visualization of targets with resolution beyond a theoretical limit. In this thesis, I describe the development of methodologies related to "*in vivo*" and "super-resolution" imaging.

Apoptosis, which is a natural machinery of cell suicide, have been analyzed by optical and electron microscopy. Because abnormalities in the machinery cause many diseases such as cancer, autoimmune disorder, neurodegenerative disorder and ischemic injury in multicellular organisms, a better understanding of the mechanism of apoptosis is crucially important in developing novel therapeutic reagents for these diseases. Mitochondria often play a central role in the induction of apoptosis. In response to apoptotic stimuli such as UV light, Bak proteins are oligomerized to form a cluster on mitochondrial outer membrane. This Bak cluster induces the release of Smac from mitochondria to cytosol, resulting in the degradation of proteins and DNA, and finally cell death (**Chapter 1**).

Apoptosis occurs in live multi-cellular organisms and thus it is essential to investigate live multicellular organisms in order to elucidate the detailed mechanism of apoptosis. However, most of previously reported methods are not applicable to live animals. To overcome this problem, I aimed to develop a method for visualizing apoptosis in a live animal. The method for visualizing apoptosis *in vivo* is based on spontaneous complementation of a green fluorescent protein (GFP), in which non-fluorescent GFP fragments ($GFP_{1–10}$ and GFP_{11}) are spontaneously associated with each other to recover the fluorescence. The method, which uses two probe proteins ($GFP_{1–10}$ and Smac-GFP_{11}), visualizes apoptosis by detecting Smac release with the fluorescence of complemented GFP. This approach enables less-invasive detection of apoptosis with high signal-to noise ratio, which makes it applicable to *in vivo* apoptosis imaging (**Chapter 2**).

Because the formation of Bak cluster on mitochondria leads to the release of Smac from mitochondria into cytosol and induces apoptosis, there has been a great interest in understanding the character of Bak cluster. However, the cluster is too small to be characterized by optical

microscopy because the size of Bak cluster is smaller than the diffraction limit (～250 nm) of optical microscopy. To prevail against the difficulty, I also aimed to develop a method for characterizing the Bak cluster during apoptosis. The method for the analysis of Bak clusters is based on photo-activated localization microscopy (PALM), which is one of the optical techniques at the spatial resolution beyond the diffraction limit. In this method, photo-activatable fluorescent proteins (PA-FPs) such as mEos3 are used to achieve temporal control of the fluorescence emission. PALM provides spatial resolution down to a few tens of nanometers and it is possible to count the number of molecules in a region of interest since PALM is based on single-molecule detection. Therefore, the method is applicable to the characterization of the size, stoichiometry and localization of PA-FP labeled Bak (**Chapter 3**).

Table of Contents

Chapter 1. General Introduction

Chapter 2. Development of a Method for Visualizing Apoptosis *in vivo*

Abbreviation

2D	Two dimension/two dimensional
3D	Three dimension/three dimensional
ANOVA	Analysis of variance
BCA	Bicinchoninic acid
BH3	Bcl-2 homology 3
BMH	Bismaleimidohexane
CARS	Coherent anti-Stokes Raman scattering
CCD	Charge coupled device
cDNA	Complementary deoxyribonucleic acid
CFP	Cyan fluorescent protein
CMV	Cytomegalovirus
CoV	Coefficient of variation
CT	Computed tomography
DBSCAN	Density-based spatial clustering of application with noise
DMEM	Dulbecco's Modified Eagle Medium
DNA	Deoxyribonucleic acid
dUTP	2'-deoxyuridine 5'-triphosphate
EF1	Elongation factor-1
EM	Electron microscopy
EM-CCD	Electron multiplying charge coupled device
ER	Endoplasmic reticulum
FBS	Fetal bovine serum
FRAP	Fluorescence recovery after photobleaching
FRET	Förster resonance energy transfer
FSG	Fish skin gelatin
FWHM	Full width of half maximum
GAPDH	Glyceraldehyde 3-phosphate dehydrogenase
GFP	Green fluorescent protein
Hb	Hemoglobin
HEPES	4-(2-hydroxyethyl)-1-piperazineethanesulfonic acid
HILO	Highly inclined and laminated optical
HRP	Horseradish peroxidase
IgG	Immunoglobulin G
IPTG	Isopropyl β-D-1-thiogalactopyranoside
IR	Infra-red

$LD_{50/60}$	Lethal dose, 50%, 60 days
MEF	Mouse embryonic fibroblast
MOMP	Mitochondrial outer membrane permeabilization
MRI	Magnetic resonance imaging
mRNA	Messenger ribonucleic acid
MW	Molecular weight
n.s.	Not significant
NA	Numerical aperture
NCBI	National Center for Biotechnology Information
NIR	Near infra-red
PA-FP	Photo-activatable fluorescent protein
PALM	Photo-activated localization microscopy
PCR	Polymerase chain reaction
PET	Positron emission tomography
pI	Isoelectronic point
PS	Phosphatidylserine
PSF	Point spread function
s.e.m.	Standard error of mean
SD, s.d.	Standard deviation
SDS-PAGE	Sodium dodecyl sulfate-polyacrylamide gel electrophoresis
SEM	Scanning electron microscope
SHG	Second-harmonic generation
SIM	Structured illumination microscopy
STED	Stimulated emission depletion
STORM	Stochastic optical reconstruction microscopy
TdT	Terminal deoxynucleotidyl transferase
TEM	Transmission electron microscope
TIRF	Total internal reflection fluorescence
TMR	Tetramethyl rhodamine
TMRE	Tetramethylrhodamine ethyl ester
TP	Two-photon
TUNEL	Terminal deoxynucleotidyl transferase-mediated dUTP nick-end labeling
US	Ultrasound
UV	Ultra violet
YFP	Yellow fluorescent protein
ZGC	Zebrafish gene collection

Chapter 1

General Introduction

1-1. Microscopies for biological samples

Cells, which constitute our bodies, are too small to be observed by naked eyes. To overcome the difficulty, various microscopes have been developed to observe and understand the structural organization of cells since Dutch eyeglass makers, Zacharias Janssen and Hans Janssen, developed a prototype of a microscope in 1590[1]. The methodology to investigate small objects using a microscope is called microscopy. In this section, I focus on two microscopies, "optical" and "electron" microscopy, which have been most often applied to biological specimens including organelle, cell, tissue and whole body.

1-1-1. Optical microscopy

Optical microscopy is the methodology of a microscope using "light" to observe samples. Simply put, an optical microscope is the combination of two convex lens and a light source to magnify and observe specimen (**Figure 1-1**). There are two major factors to characterize a microscope; magnification and resolution. First, the magnification of the microscope (M) is given by

$$M = M_{objective} \times M_{ocular} \tag{1.1}$$

where $M_{\text{objective}}$ and M_{ocular} represent the magnification of the objective lens and the ocular lens, respectively. For example, you acquire the image of the sample at 400x magnification when you use 40x objective lens and 10x ocular lens. Second, the resolution of the microscope (R) is defined as the shortest distance at which the image of two point-like objects can be

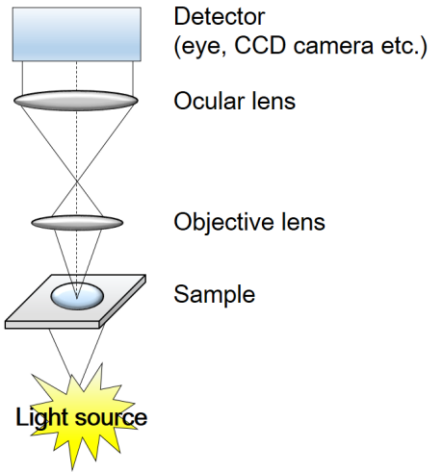

Figure 1-1. Optical microscopy.
The figure shows a simplified schematics of an optical microscopy. Magnified image of the sample is captured on a detector through objective lens and ocular lens.

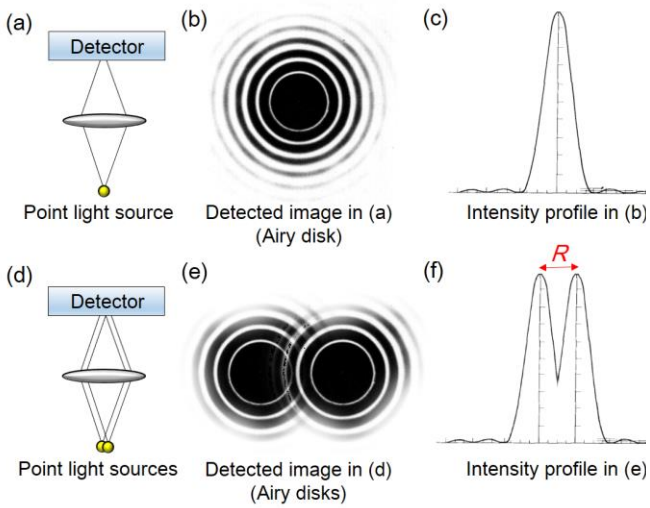

Figure 1-2. Resolution of the microscope.
Point light source is imaged as not a point but a diffraction pattern called an Airy disk. R depends on wavelength of light and the numerical aperture (NA) of the objective lens.

distinguished (**Figure 1-2**). *R*, which is often called the diffraction limit, is given by

$$R = \frac{0.61\lambda}{n\sin\alpha} = \frac{0.61\lambda}{NA} \tag{1.2}$$

where λ represents the wavelength of light, n indicates the refraction index of the medium between the sample and objective lens, α is the half opening angle of the objective lens, and NA is numerical aperture.

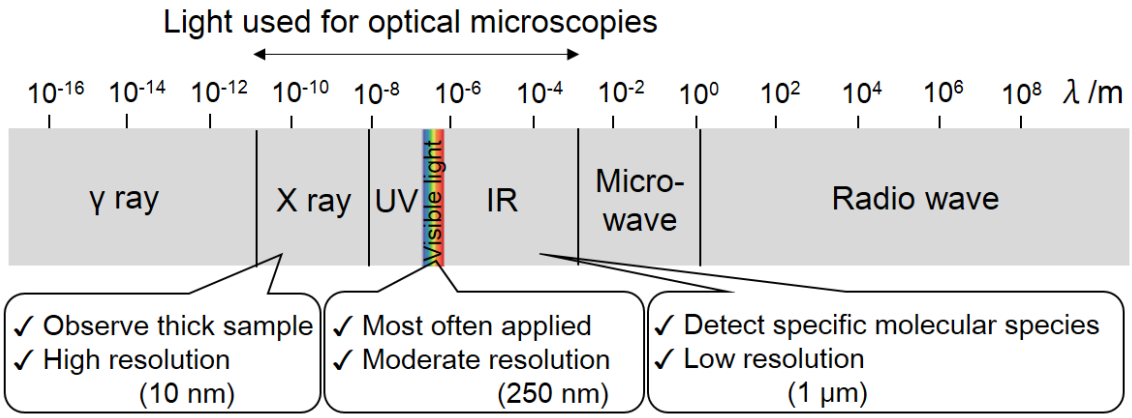

Figure 1-3. Light used for optical microscopies.

In optical microscopy, there are a variety of light wavelength used for the sample illumination or the signal detection; X-ray, ultra-violet (UV), visible light and infra-red (IR), each of which offers different information on the sample (**Figure 1-3**). For example, X-ray microscopy is capable of observing deep inside specimen because X-ray readily penetrate into the sample. Furthermore, the wavelength of X-ray in the microscopy is approximately 1 nm, which offers higher spatial resolution (ca. 10 nm) than optical microscopy using light with other wavelength (see equation (1.2))[2]. Raman microscopy uses IR called Raman scattering which is the light scattered from sample irradiated with excitation light[3]. Raman scattering with specific wavelength corresponds to molecular vibration frequency which is unique to a specific molecular species. Therefore, Raman microscopy is capable of detecting specific molecules such as cytochrome c in mitochondria without labelling. Although Raman microscopy does not require labelling of target molecule, the method using IR as detected

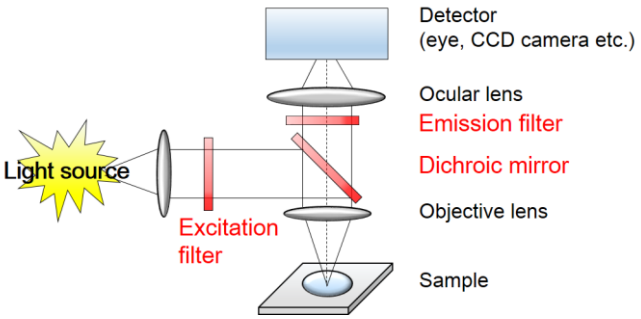

Figure 1-4. Fluorescence microscopy.
Fluorescence microscope is similar to an ordinary optical microscope (see **Figure 1-1**) except that the excitation light from a powerful light source such as a mercury lamp and a laser is passed through filter sets; excitation filter, dichroic mirror and emission filter.

Table 1-1. Fluorescent dyes used in fluorescence microscopy.

Structure	Fluorescent dyes	λ_{ex}/nm	λ_{em}/nm	ε/cm^{-1}M^{-1}*	Q.Y.**
Organic chemicals	Fluorescein	494	518	77,000	0.93
	Rhodamine 6G	525	555	108,000	0.95
	Cy 3	550	570	150,000	0.15
	Cy 5	649	670	250,000	0.28
	Alexa Fluor 488	495	519	71,000	0.92
	Alexa Fluor 647	650	668	239,000	0.33
Fluorescent proteins	BFP	377	446	31,000	0.15
	CFP	433	475	32,500	0.40
	GFP	484	507	56,000	0.60
	YFP	513	527	83,400	0.61
	mCherry	587	610	72,000	0.22
	iRFP***	690	713	85,000	0.059

*Extinction coefficient, **Quantum yield,
*** Filonov, G. S. *et al. Nat. Biotech.* **29**, 757−761 (2011).

signals provide an image with lower resolution (ca. 1 μm) than other optical microscopies.

Fluorescence microscopy detects a fluorescence, the wavelength of which belongs to visible light, emitted from sample exposed with excitation light (**Figure 1-4**). Because the wavelength of a fluorescence (λ_{em}) is longer than that of an excitation light (λ_{ex}), the fluorescence signal is able to be detected separately from the excitation light by using filter sets; excitation filter, dichroic mirror and emission filter. Excitation filter passes only the wavelength that excite the particular fluorescent dye. Emission filter passes only the fluorescence emitted from the dye. Dichroic mirror passes the fluorescence but not the excitation light. Fluorescence microscopy is most often used to detect specific proteins or other molecules labelled with fluorescent dyes in biological samples such as cells and tissues. Various fluorescent dyes have been developed for fluorescent microscopy (**Table 1-1**)[4]. These dyes emit bright fluorescence signal and are capable of specifically labelling to target molecules of interest, thus fluorescence microscopy allows to specifically visualize the target with high

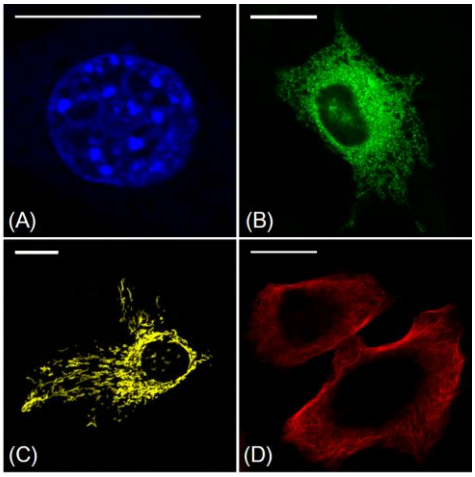

Figure 1-5. Cellular structures visualized by fluorescence microscopy. (**A**) Nucleus labelled with a blue dye, Hoechst33342. (**B**) Endoplasmic reticulum labelled with GFP. (**C**) Mitochondria labelled with YFP. (**D**) Microtubules labelled with Alexa Fluor 647. Fluorescence microscopy specifically visualizes target of interest with a high signal-to-noise ratio. Scale bars; 20 μm.

signal to noise ratio (**Figure 1-5**). Resolution achieved with fluorescence microscopy is approximately 250 nm which is moderate among optical microscopies.

1-1-2. Electron microscopy

Electron microscopy (EM), which was first developed by the German physicist Ernst Ruska and the electrical engineer Max Knoll in 1931, is the methodology of a microscope using "electron" instead of light to observe samples. EM can resolve much smaller structures than is possible with optical microscopies because the wavelength of an electron is a few picometer (10^{-12} m) which is much shorter than light used in optical microscopies. When the wavelength of an electron is 0.004 nm, the resolution should be approximately 0.002 nm in theory, which is 100,000 times that of the fluorescence microscopy. The practical resolution of most modern electron microscopes is approximately 0.1−1 nm (1−10 Å) because of the aberrations of an electron lens and problems of sample preparation. This high resolution comes at costs. First, electron is unable to be regulated by a conventional lens made of glass which are commonly used in optical microscopies. EM solves the difficulty by using magnetic coils to regulate the movement of electrons. Second, electrons are scattered by collisions with air molecules. Therefore, air must be pumped out to create a vacuum around the specimen in EM, which makes it impossible to apply EM to living samples.

There are two modalities in EM; the transmission electron microscope (TEM) and the scanning electron microscope (SEM). TEM is similar to an optical microscope in overall system (**Figure 1-6**). TEM detects the electrons that have passed through

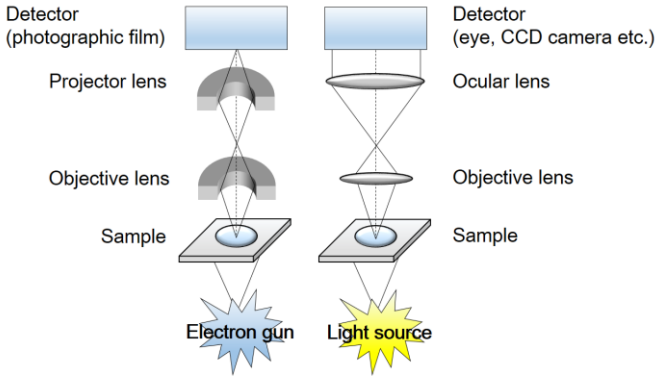

Figure 1-6. Transmission electron microscope (TEM).
Left and right figure show simplified schematics of TEM and an optical microscopy, respectively. The source of electron, so called "an electron gun", is a filament or cathode. Note that TEM has the similar system to optical microscopies except that lens used in TEM are not made of glass but magnetic coils.

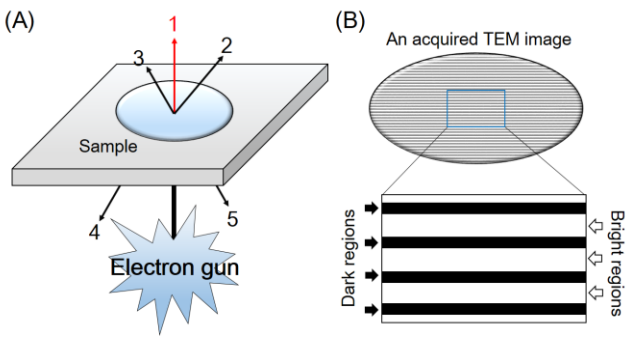

Figure 1-7. Principle of the image acquisition in TEM.
(**A**) After the electron beam is irradiated to sample, various electron fluxes are generated; transmitted electron (1), elastically-scattered electron (2), inelastically-scattered electron (3), back-scattered electron (4), and secondary electron (5). Of them, the transmitted electron is detected to form an image. Of these electrons, transmitted electron is detected in TEM. (**B**) An acquired TEM image has dark region and bright region. This contrast comes from the distribution of the density of electrons which depends on the atomic number of the atoms in the specimen.

the specimen to form an image in which dark regions indicate the area of fewer electrons detected because of the scattering (**Figure 1-7**). Because electrons are scattered by electrons with electrostatic interaction, the dark signal represents the region with high electron density. Contrast in the EM depends on the atomic number of the atoms in the specimen since the atoms with the higher atomic number have more electrons. However, it is difficult to obtain an image with high contrast in biological tissues because they are composed of atoms of very low atomic number such as $_6$C (carbon), $_8$O (oxygen), $_7$N (nitrogen) and $_1$H (hydrogen). To make them visible, they are chemically fixed by osmium tetroxide (OsO_4), which binds to and stabilizes lipid bilayers as well as proteins. Since osmium has large atomic number ($_{76}$Os), cellular structures such as mitochondria and plasma membrane fixed with OsO_4 can be visualized with high contrast in TEM (**Figure 1-8**). Furthermore, TEM requires the sample to be cut into extremely thin section (50−100 nm thick) for the observation because electrons have very limited penetrating power.

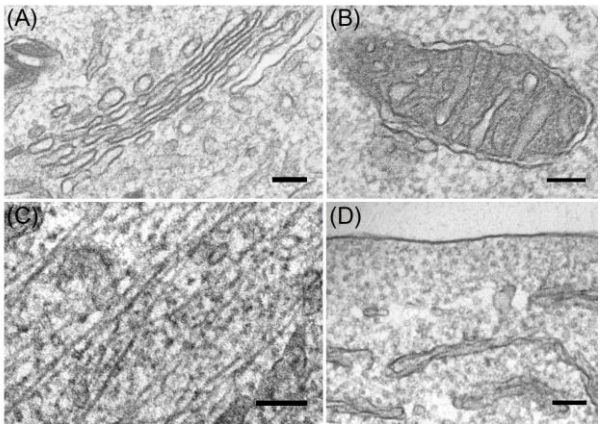

Figure 1-8. TEM images of cellular structures.
(**A**) Golgi apparatus. It consists of a collection of flattened and membrane-enclosed compartments. (**B**) Mitochondrion. It is enclosed by two highly specialized membranes, inner and outer membrane. (**C**) Microtubules. The diameter of the filamentous structures is approximately 25 nm. (**D**) Plasma membrane and endoplasmic reticulum. Scale bars; 100

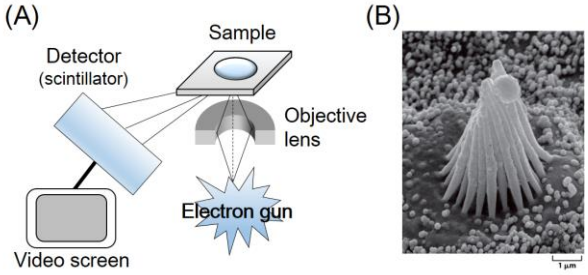

Figure 1-9. Scanning electron microscopy (SEM).
(**A**) A simplified schematics of SEM. Whereas TEM detects transmitted electrons, SEM detects scattered electrons. (**B**) A SEM image of the stereocilia in a hair cell[5]. Since the signal in SEM, which especially detects secondary electrons, depends on the angle of the surface relative to the incoming electron beam, the obtained image shows a three-dimensional appearance.

Another type of EM is SEM which detects backscattered electrons or secondary electrons (**Figure 1-9**). Backscattered electrons are produced by elastic interactions with specimen and have the same energy as the incoming electron beam. Because the extent of backscattering depends on the atomic number of the atoms in the specimen, SEM image acquired by detecting backscattered electrons reflects chemical compositions in the specimen. On the other hand, secondary electrons are derived from inner-shell of the atoms in the specimen by inelastic interactions and have low energy (less than 50 eV). Secondary electrons are produced from only the surface of the specimen (10 nm depth) and the amount of them detected depends on the angle of the surface relative to the incoming beam. Therefore, steep surfaces and edges tend to be brighter than flat surfaces in SEM image acquired by detecting secondary electrons.

1-1-3. Methods for imaging live animals "*in vivo* imaging"

Microscopy is the methodology for magnifying and observing a tiny target which otherwise cannot be seen. To observe the target with high magnification, microscopy especially for biological sample often requires a destructive sample preparation such as lysis, embedding and fixation. These destructive processes are "invasive". Because these invasive preparations could perturb the original condition of the specimen, it is hard to be sure that the image acquired with the microscopy corresponds precisely to the actual structure being examined. To observe the actual condition in the sample, the method for sample preparation should be less- or non-invasive. Furthermore, a living animal (multi-cellular organism) as well as a culture cell (mono-cellular organism) should be analyzed to understand the true biological phenomena. Recently, various microscopies for imaging a living animal based on less-invasive sample preparations have been developed to achieve the purpose[6]. The imaging for analyzing living animals such as mice is called "*in vivo*" imaging. In this section, I focus on optical methods for *in vivo* imaging although several non-optical *in vivo* imaging methods based on nuclear magnetic resonance (magnetic resonance imaging; MRI), positron emission (positron emission tomography; PET), ultrasound (US echo) and photo-acoustic microscopy are also currently available.

X-ray computed tomography (X-ray CT), which is first developed by an English engineer Godfrey N Hounsfield in 1967, is the methodology for imaging inside the specimen by detecting X-ray transmitted through it (**Figure 1-10**)[7]. Contrast in a CT image indicates the level how much X-ray is absorbed in the particular region. X-ray readily penetrates the specimen (see section 1-1-1), which makes X-ray CT capable of visualizing 3D images of whole organs or the whole body in a live animal including human as a clinical application. The spatial and temporal resolution of X-ray CT for clinical use is sub-millimeter and several few seconds, respectively[8]. Although *in vivo* imaging should be less- or non-invasively performed, X-

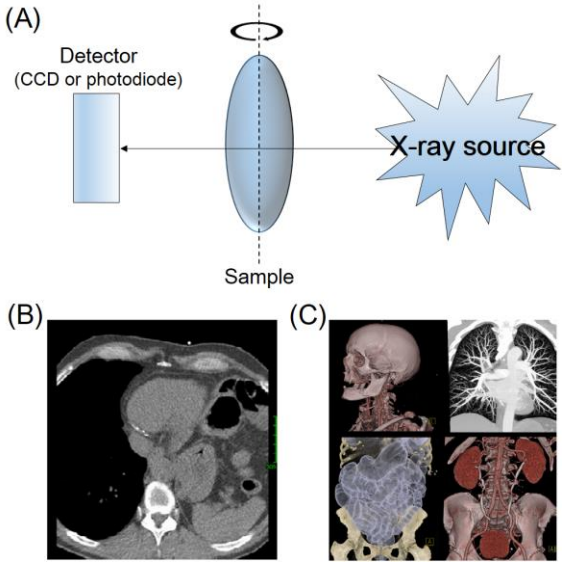

Figure 1-10. X-ray computed tomography (X-ray CT). (**A**) Schematic diagram of X-ray CT. In the system, the sample is placed on a rotating stage between an X-ray source and a detector. The sample is exposed to X-ray from all direction and X-ray transmitted through it is detected as a signal. The signal reflects how much the sample in a particular region absorbs X-ray. The signals are mathematically processed to reconstruct a CT image. (**B**) 2D CT image of human internal organs. (**C**) 3D CT images of human skeleton and organs.

ray can break DNA structure, thus high dose of X-ray radiation is toxic to a live subject. In X-ray CT for clinical use, human is subjected to X-ray of approximately 30 mGy, which is a hundred times less than $LD_{50/60}$ (4 Gy)[9], so the toxicity is very limited. Here, $LD_{50/60}$ represents the radiation dose to kill 50% of individuals 60 days after the irradiation. On the other hand, X-ray microCT, which has been recently developed for basic research to observe living animals except for human being, uses stronger X-ray source. Therefore, X-ray microCT offers 3D images of soft-tissue structures, skeletal abnormalities, and tumors with the resolution of several tens micrometer, which is ten times better than that of clinical CT.

Optical microscopy requires the light for illuminating sample. The requirement makes it difficult to apply optical microscopy except for microscopies using X-ray to *in vivo* imaging because illumination light is absorbed in deep tissue (**Figure 1-11**)[10]. To overcome this limitation, several "non-linear" optical microscopies have been developed; two-photon (TP) microscopy, second-harmonic generation (SHG) microscopy and coherent anti-Stokes Raman scattering (CARS) microscopy[11]. These microscopies are based on non-linear phenomena, where multi photons are absorbed to produce emission signals, and use longer wavelength (700−1000 nm) than conventional optical microscopies using blue or green light (**Figure 1-12**). TP microscopy belongs to fluorescence microscopy and is often used for imaging

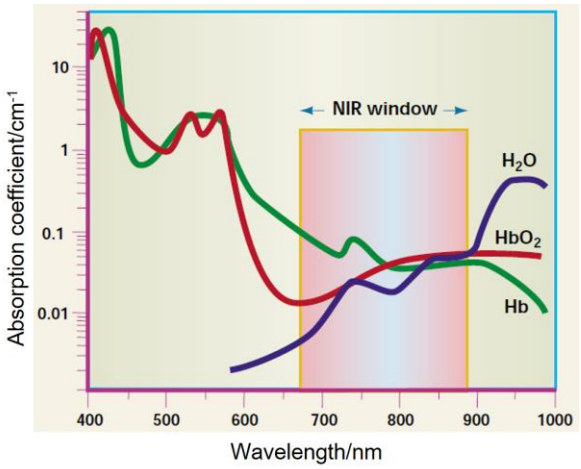

Figure 1-11. Absorbance spectrum in living tissues. Visible light with wavelength shorter than 600 nm is well absorbed by hemoglobin (Hb) in tissues. Near infra-red (NIR) light is suitable for illuminating deep tissue.

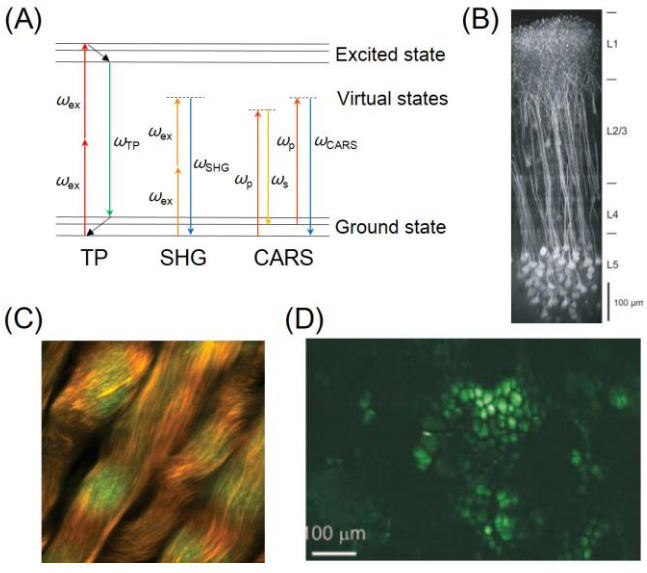

Figure 1-12. Non-linear optical microscopies.

(**A**) Jablonski diagram illustrating TP, SHG and CARS. ω_{ex}: frequency of excitation light, ω_{TP}: frequency of emission light in TP microscopy, ω_{SHG}: frequency of SHG light, ω_p: frequency of pump light, ω_s: frequency of Stokes light, ω_{CARS}: frequency of CARS light. In CARS microscopy, specimen absorbs two kinds of excitation light (pump light and Stokes light) to emit CARS signal. No actual electronic excitation takes place in SHG and CARS. (**B**) TP image of mouse neocortex. Nearly the entire depth of the neocortex is imaged. Scale bar: 100 μm[11]. (**C**) SHG image of rat tendon. Green and Red indicate immature fibril segments and mature fibrils, respectively[12]. (**D**) CRAS image of mouse ear at a depth of 100 μm[13]. Green signal indicates adipocytes.

fluorescent-labelled neurons in live mouse, which cannot been visualized by conventional optical microscopy because of the difficulty with penetration of excitation light. TP microscopy is able to observe maximum 1 mm deep (a few tens micrometer in case of conventional fluorescence microscopy) in animal tissue with resolution of approximately 400 nm. On the other hand, SHG and CARS microscopy do not require fluorescent labelling of target. These methods are called "label-free" imaging. SHG signal is produced from the inversion-asymmetrical or spatially-ordered molecules, so SHG microscopy is often used for investigating collagen fibers or microtubuli in animal tissue with submicron resolution. CARS detects Raman-active vibrational modes within molecules by using two synchronized pulsed lasers, pump light (ω_p) and CARS light (ω_{CARS}). Raman-active molecules have vibrational modes with particular energy (Ω) which corresponds to the difference between ω_p and ω_{CARS}. Thus, CARS is capable of detecting various Raman-active molecules such as lipid, myelin and water in living animal tissue by arranging ω_p and ω_{CARS} with resolution of approximately 300 nm in the lateral plane.

1-1-4. Optical microscopies breaking the diffraction barrier

As I mentioned in section 1-1-1, optical microscopy has the diffraction limit, which is the limit of spatial resolution, theoretically calculated by the equation (1.2). When you use light wavelength of 570 nm and 1.4 NA lens, the diffraction limit is 250 nm which is approximately the size of an intracellular organelle such as mitochondria. Since a German physicist Ernst Abbe recognized the limit about 150 years ago, optical microscopy suffers from the limit for investigating the inner architecture of many subcellular structures which are smaller than the limit. However, several imaging techniques have recently pushed the boundary of the diffraction limit of optical microscopy. These new technologies are termed "super-resolution microscopy". There are two methods in super-resolution microscopy; near-field microscopy and far-field microscopy. This categorization comes from the distance between sample and light source. In this section, I describe the principles of both microscopies.

Near-field microscopy places the light source near the sample (**Figure 1-13**). Because the diffraction limit is applicable to light that has propagated for a distance substantially longer than its wavelength, the microscopy is able to break the limit if the distance between the sample and aperture of light source is shorter than light wavelength. Indeed, near-field microscopy achieved resolution below 100 nm which is twice better than the diffraction limit achievable in conventional optical microscopy[14]. Super resolution achievable in the microscopy is highly attractive for investigating nano-scale structures in cells. However, the requirement that the light source must be physically close to the sample has made it difficult to look interior structures, which limits the application of near-field microscopy in biology.

Another type of super-resolution microscopy is far-field microscopy. Recently, several far-field super-resolution microscopies have been developed for investigating cellular structures;

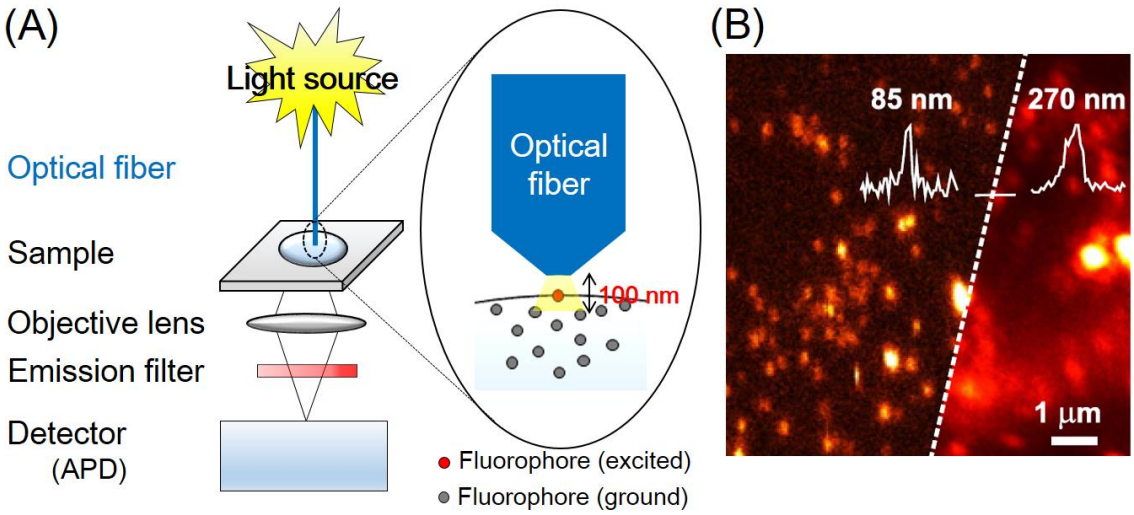

Figure 1-13. Near-field microscopy.

(**A**) Principle of a near-field microscopy. Excitation light is coupled into the optical fiber and is used to excite fluorophores in the sample. The optical near-field generated at the aperture has significant energy only in a layer of 100 nm, thus fluorophores only which localize on the surface are excited. By scanning the fiber, the entire super-resolved image is obtained. (**B**) Visualization of membrane protein labelled with fluorescent dye at cell surface by near-field microscopy[15]. Left and right image were acquired by near-field and conventional fluorescence microscopy, respectively.

structured illumination microscopy (SIM)[16], stimulated emission depletion (STED)[17], photo-activated localization microscopy (PALM)[18] and stochastic optical reconstruction microscopy (STORM)[19]. Although all of them are capable of visualizing targets beyond the diffraction limit, their principles are different from each other. SIM illuminates a sample with a series of sinusoidal striped patterns with high spatial frequency (**Figure 1-14**). This special illumination produces an image called moiré fringe. By applying these excitation patterns in different orientations and all acquired images using computer algorithms, a super-resolution image of the target is generated. This approach improves the lateral resolution by a factor of two beyond the diffraction limit, resulting in the lateral and axial resolution of 100 nm and 300 nm,

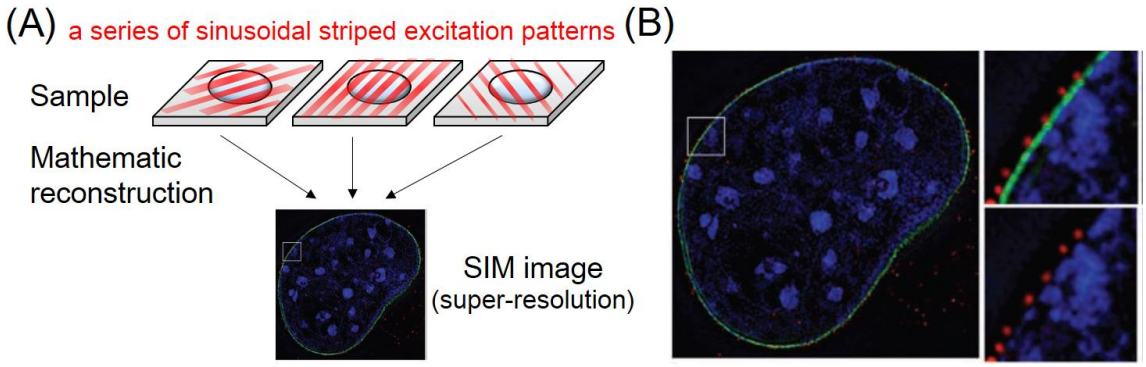

Figure 1-14. Structured illumination microscopy (SIM).

(**A**) Principle of SIM. SIM uses sinusoidal-patterned illumination to excite the sample. Acquired images are computationally processed to reconstruct a SIM image. (**B**) SIM image of cellular nucleus. Blue, green and red indicate DNA, nuclear membrane protein and nuclear pore protein, respectively[20]. Conventional fluorescent dyes are applicable to SIM, which makes it easier to simultaneously observe several targets with multi-color.

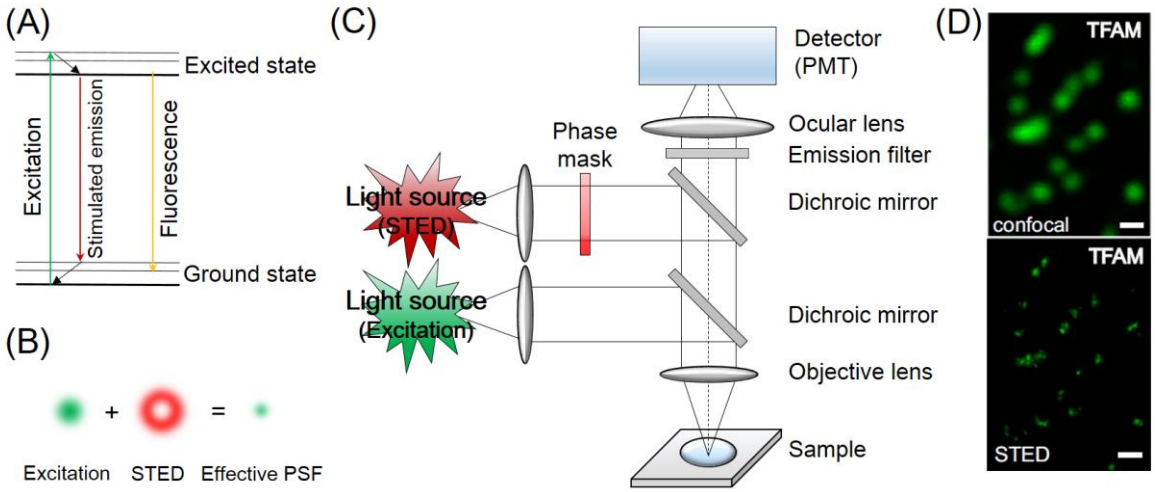

Figure 1-15. Stimulated emission depletion (STED) microscopy.

(**A**) Jablonski diagram illustrating the process of stimulated emission. Stimulated emission happens when the excited fluorophore meets another light with energy comparable to the difference between the ground and excited states. (**B**) When a donut-shaped STED light (red) is overlapped with the excitation light (green), fluorescence from regions near the center is suppressed, resulting in a decreased size of effective point spread function (PSF). (**C**) Schematic diagram of STED microscopy. Excitation and STED light are simultaneously illuminated to the sample. By scanning these lights in all region of the sample, a STED image with super-resolution is acquired. (**D**) STED image of mitochondrial DNA in human fibroblast[21]. Compared to conventional image (upper panel), STED image (lower panel) shows much higher resolution.

respectively. Attractive features of SIM for biological application are that standard dyes can be used and that a target can be imaged with optical sectioning in three dimensions. Other far-field super-resolution microscopies, STED and PALM, limit the applicability of the fluorescent dye, but SIM does not require special dyes. Furthermore, SIM is able to visualize a target in 3D, which is impossible in near-field microscopy.

STED also uses special illumination pattern to achieve super resolution (**Figure 1-15**). The diffraction limit originates from the fact that in principle it is impossible to concentrate excitation light on a spot (point spread function; PSF) which is smaller than the limit. In STED microscopy, this spot of excitation light becomes much smaller by simultaneously illuminating stimulated emission depletion beam which has a donut-like shape with a zero intensity. This is why STED microscopy can break the diffraction limit. The resolution achievable in STED microscopy, R_{STED}, is given by

$$R_{STED} \approx \frac{0.61\lambda}{NA\sqrt{1+\frac{I}{I_S}}} = \frac{R}{\sqrt{1+\frac{I}{I_S}}} \tag{1.3}$$

where I is the peak intensity of STED light and I_S is the saturation intensity for the fluorophore[22]. The level of I and I_S used in STED microscopy is $\sim 10^7$ W/cm^2 and $\sim 10^9$ W/cm^2, resulting in the lateral resolution of approximately 60 nm. Note that the method is capable of imaging a target with super resolution laterally, but the axial resolution is the same as conventional optical microscopy because the production of the small PSF is limited in 2D (xy plane, lateral plane).

The considerable costs of this technology is the limitation of the choice of the appropriate dye, especially in multi-color imaging. The wavelength of STED light needs to by no means fall into the excitation range of the dye used in order to avoid unwanted excitation by STED light. Furthermore, the absorption of STED light by the excited singlet or triplet state of the dye must be avoided to suppress severe photobleaching. Accordingly, the set of suitable dyes is limited.

PALM and STORM are based on single-molecule detection. I discuss PALM in section 1-5-2. Here, I focus on the principle and the application of STORM. STORM uses photo-switchable fluorophores to achieve temporal control of the emission (**Figure 1-16**). These fluorophores can be converted between a fluorescent and a dark state. Duration of the dark state of fluorophores is originally so short that all of them are visualized at the same time, which make it impossible to resolve them individually. However, the duration can be longer by using a reducing agent and an oxygen scavenger system. As a result, each fluorophore is able to be individually visualized and is localized to high precision by Gaussian fitting. The resolution achievable in STORM, R_{STORM}, is given by

$$R_{STORM} \approx \frac{0.61\lambda}{NA\sqrt{N}} = \frac{R}{\sqrt{N}} \tag{1.4}$$

where N represents the number of photons emitted from a fluorophore[22]. This equation indicates that the brighter fluorophore can be localized with higher spatial resolution. N detected in STORM is $\sim 10^3$ in the case of cyanine dyes such as Cy5, resulting in the lateral resolution of approximately 20 nm[23]. Although STORM offers higher spatial resolution than SIM and STED, the method requires as additional processing step to obtain a super-resolution image. This processing after the acquisition of raw data includes three steps; (1) identification of a single fluorophore, (2) Gaussian fitting and (3) the reconstruction of a STORM image. In (1), the algorithm distinguishes a specific fluorescent spot from other spots and identifies it as a single fluorophore. Subsequently, in (2), the algorithm fits 2D Gaussian with an intensity profile of the fluorophore to determine its precise position. Finally, in (3), the localized fluorophore is visualized, reconstructing a STORM image. There are many algorithms currently available to perform these data processing and they shows different characters particularly in (1) and (2). Thus, the quality of the image strongly depends on the algorithm you use for the processing. It is therefore important to understand the content of the algorithm you use when you acquire a STORM image.

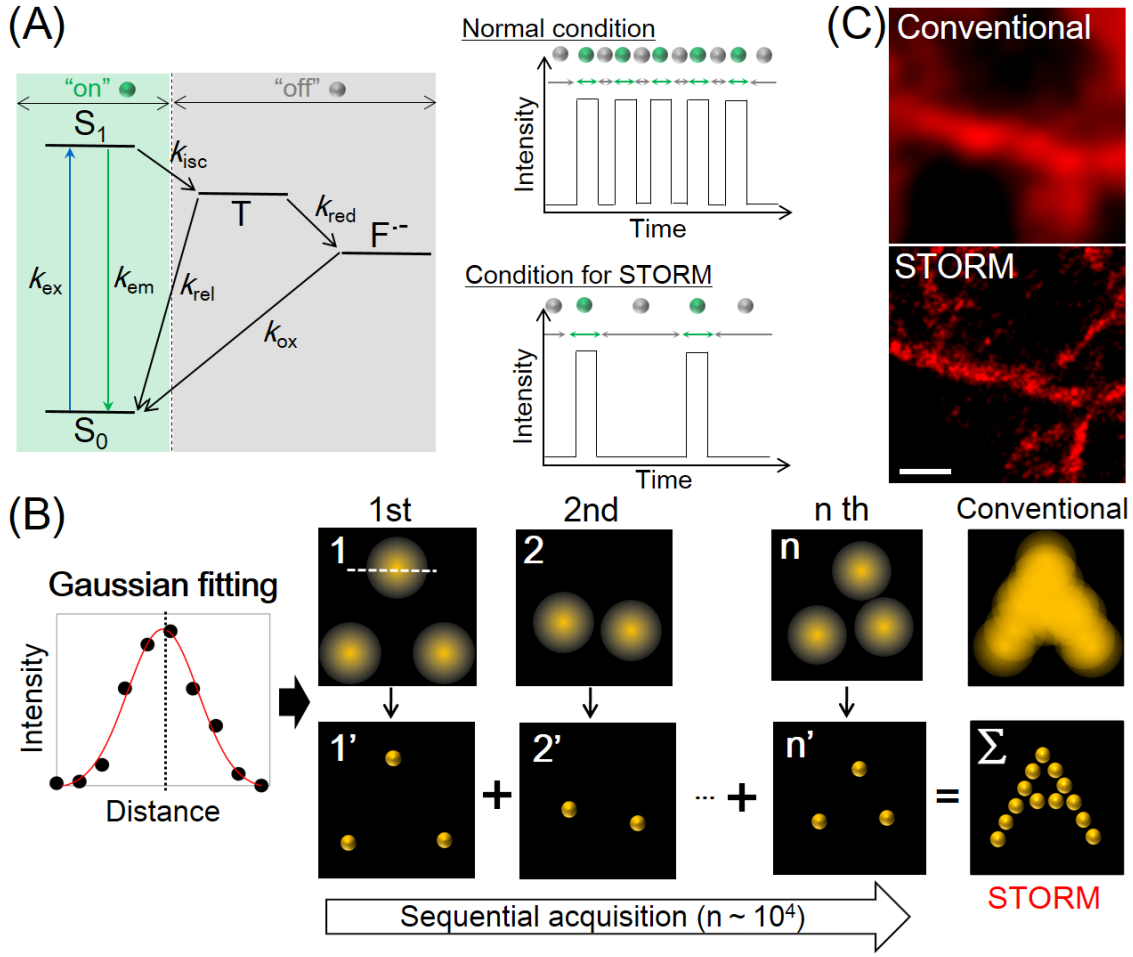

Figure 1-16. Stochastic optical reconstruction microscopy (STORM).

(**A**) Jablonski diagram illustrating the process of the blinking and the fluorescence intensity profiles showing the stochastic blinking of a single fluorophore. The excited fluorophore (S_1) returns to the ground state (S_0) to emit a fluorescence or a dark triplet state (T) by intersystem crossing. In the triplet state, the fluorophore reacts with molecular oxygen to give rise to photobleaching. To avoid it, an oxygen scavenger system, which is the combination of glucose, glucose oxidase and catalase, should be added into the buffer used for STORM. Furthermore, the addition of a reducing agent such as β-mercaptoethanol depletes the triplet state by electron transfer reaction, resulting in the production of radical form ($F^{\cdot-}$). Taken together, the environment including an oxygen scavenger system and a reducing agent makes duration of a dark state longer, which is critically important for STORM. The radical species returns to S_0 by oxidation. These molecular processes shown in the diagram lead to stochastic photo-blinking of a single fluorophore (right figure), which is critically important for STORM. (**B**) Principle of STORM. Because "on" state happens stochastically between fluorophores as I mentioned in (A), only a random and sparse subset of fluorophores are excited by illuminating fluorophores distributed in a sample with excitation light, allowing these molecules to be imaged individually. These imaged molecules are localized to high precision by determining their centers of fluorescence emission using Gaussian fitting. Repeating this process, a STORM image with "super-resolution" is obtained as a summation of rendered images of each fitted molecule in all frames. (**C**) STORM image of microtubule in a human osteosarcoma cell. Compared to conventional image (left), STORM image (right) shows much higher resolution.

1-2. Cell death in living organism

1-2-1. Apoptosis

Cell death plays a critically important role in plant and animal early development, and it continues into adulthood[24]. It is known that this cell death is suicide, in which the cells activate an intracellular death program and kill themselves. The cell death is therefore often called "programmed" cell death. Since Kerr *et al*. observed this cell death and named the phenomenon, "apoptosis" (from the Greek word representing "falling off", as leaves from a tree) in 1972, the idea that animal cells are intrinsically equipped with death program have been proposed[25]. The idea was accepted when the genes dedicated to programmed cell death and its control were identified in the nematode *C. elegans* in early 1990s[26]. Apoptosis is morphologically characterized by DNA fragmentation, cytoplasmic condensation, nuclear pyknosis, chromatin condensation, cell rounding, membrane blebbing and the formation of membrane-bound apoptotic bodies (**Figure 1-17**). The surface of apoptotic cells becomes chemically altered so that macrophages (specialized cells in immune system) or neighboring cells engulfs and digests them before they spill their content. In this way, apoptotic cells are removed without inducing inflammatory response.

Apoptosis functions both in early development and adulthood. For example, more than half of many types of neurons die of apoptosis soon after they are formed in the developing vertebrate nervous system, and the majority of neutrophils (a type of white blood cell) die by apoptosis in the adult human bone marrow. Primarily, the significance of apoptosis is to regulate

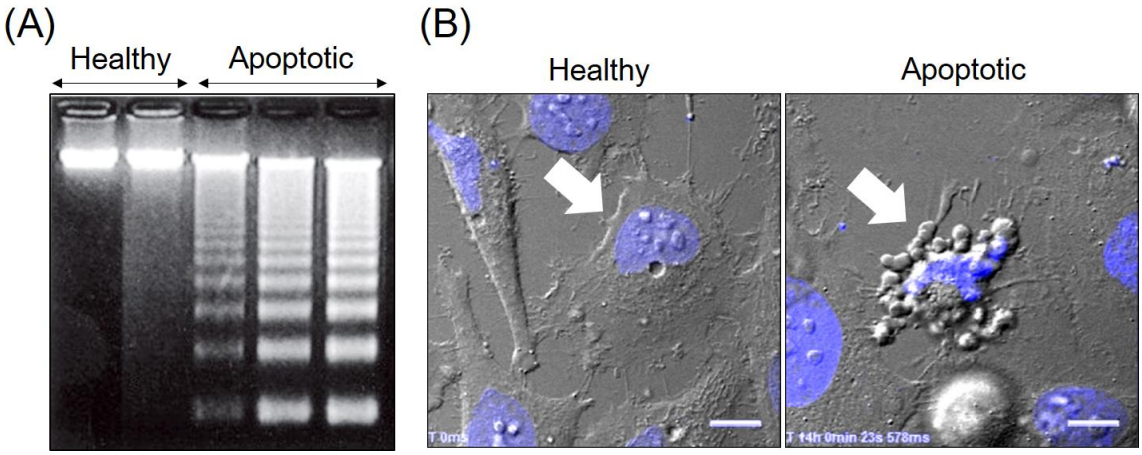

Figure 1-17. Characteristic features of apoptosis.

(**A**) The figure shows electrophoresis of mouse thymus lymphocytes[27]. In healthy condition, a single band, which represents genomic DNA of the sample, is detected. On the other hand, ladder-like bands are detected in apoptotic condition. The result shows DNA fragmentation in apoptotic cells. (**B**) Micrographs of healthy and apoptotic cells. Blue fluorescence indicates nucleus. The apoptotic cell (right panel, arrow) shows nucleus pyknosis (condensation) and the formation of small fragments called apoptotic bodies. These morphological features are the hallmark of apoptosis.

cell number and tissue size by removing unwanted cells that are abnormal, misplaced, nonfunctional, or potentially dangerous to the animal. Thus, apoptosis functions as a quality-control machinery. This important role of apoptosis in animals implies that dysfunction of apoptosis can cause serious diseases. Indeed, most cancers are associated with unusual resistance to apoptosis induction[28]. Furthermore, an increased rate of apoptosis can cause tissue atrophy. For example, elevated level of apoptosis has been identified as a mechanism for the loss of neurons in Alzheimer's diseases. In short, the loss of balance in either direction (decreased or increased apoptosis) can lead to various serious diseases.

1-2-2. Mitochondria-mediated apoptosis

Apoptosis is induced in response to a change in cellular environment by complex molecular mechanisms (**Figure 1-18**). There are two main apoptotic pathways: the extrinsic or the intrinsic pathway. Both pathways differ in the stimulant, but they converge to the activation of protease, caspase-3. In addition, mitochondria plays a central role in inducing apoptosis in both pathways. In the intrinsic pathway, Bak protein, which distributes homogeneously on mitochondrial outer

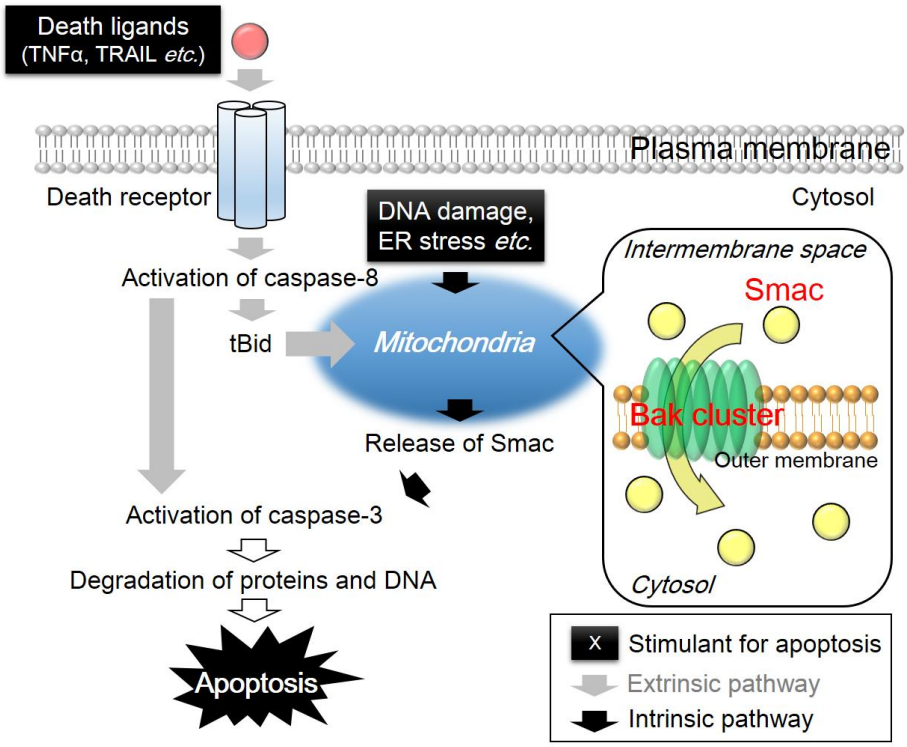

Figure 1-18. Molecular mechanism of apoptosis.

There are two pathways to induce apoptosis. In extrinsic pathway, extracellular proteins called death ligands binding to death receptors trigger apoptosis. After the binding, the receptor activates a protease, caspase-8, producing tBid which acts on mitochondria. In intrinsic pathway, apoptosis is triggered in response to injury or other stresses such as DNA damage. Upon the stimulation, mitochondria form a cluster composed of Bak protein and release protein, Smac, from intermembrane space into cytosol. Subsequently, released Smac activates a protease, caspase-3, which degrades various proteins and DNA, leading to apoptosis. In summary, mitochondria plays a central role in inducing apoptosis.

membrane in healthy condition, is oligomerized to form a cluster. The formation of Bak cluster initiates the release of pro-apoptotic proteins such as Smac from mitochondrial intermembrane space into cytosol. This protein release is called the mitochondrial outer membrane permeabilization (MOMP) and has been regarded as a point of no return for cell survival[29].

1-3. Analytical methods for apoptosis

1-3-1. Detection of apoptosis

As I mentioned earlier, apoptosis is a natural machinery of cell suicide and abnormalities in the machinery cause many diseases such as cancer, autoimmune disorder, neurodegenerative disorder and ischemic injury in multicellular organisms. Therefore, a better understanding of the mechanism of apoptosis is crucially important in developing novel therapeutic reagents for these diseases. To achieve the goal, numerous methods for detecting apoptosis have been previously developed. Here, I describe the methods for analyzing apoptosis based on optical microscopy, electron microscopy and other experimental techniques.

Many methods for detecting apoptosis with optical microscopy have been developed. Terminal deoxynucleotidyl transferase-mediated dUTP nick-end labeling (TUNEL) is used to detect the cut ends of DNA fragments in the nuclei of apoptotic cells with fluorescent microscopy (**Figure 1-19**)[30]. The method can readily and rapidly detect apoptosis in single-cell

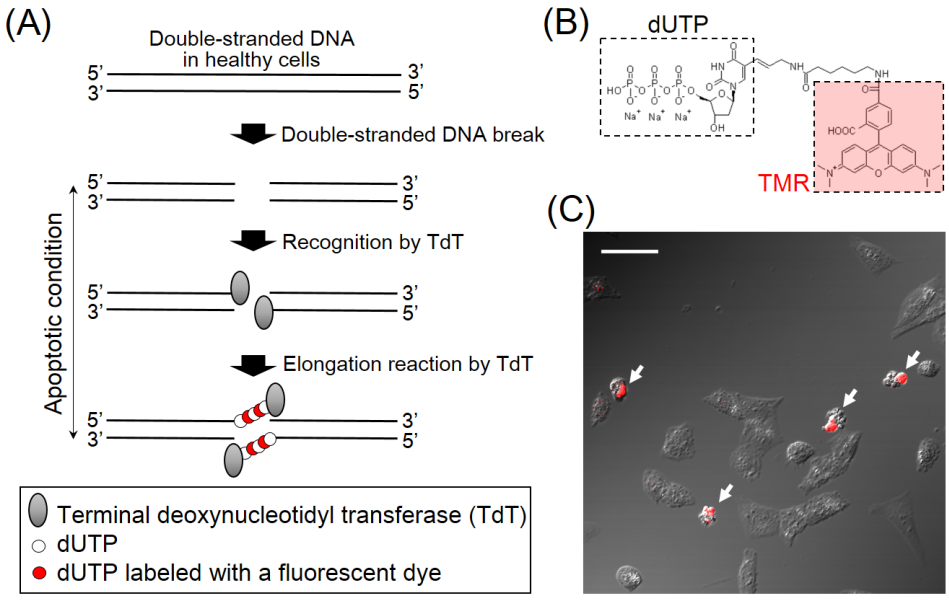

Figure 1-19. TUNEL assay.

(**A**) Principle of TUNEL assay. Terminal deoxynucleotidyl transferase (TdT) specifically recognizes double-stranded DNA break which is a hallmark of apoptosis. Subsequently, TdT catalyzes the addition of fluorescent-labelled deoxyuridine triphosphate (dUTP) to 3'-OH ends of the nick, resulting in the detection of apoptotic cells by fluorescence signal. (**B**) Structure of tetramethyl rhodamine (TMR)-labelled dUTP. (**C**) Fluorescence micrograph of UV-irradiated mouse embryonic fibroblast in TUNEL assay. Red fluorescence represents TUNEL-positive cells in which DNA is broken.

level, but it requires the fixation for sample preparation, which makes it impossible to apply TUNEL assay to living sample. Phosphatidylserine (PS) staining is also applicable to the detection of apoptosis (**Figure 1-20**). PS is one of phospholipids and normally located in the inner leaflet of the lipid bilayer of the cell membrane, but it flips to the outer leaflet in response to apoptotic stimuli. The exposed PS can be visualized with fluorescent dye labelled Annexin V protein, which specifically recognizes PS (K_d = 3.6 ± 1.1 pM)[31]. Thus, the method is able to specifically detect apoptotic cells by fluorescence signal. PS staining is widely applicable to the detection of apoptosis in living sample as well as fixed sample. However, some cell types do not expose PS during apoptosis[32] and the exposure of PS can occur in apoptosis-unrelated conditions[33]. Hence, it is important to combine the method with other methods to investigate apoptosis in order to avoid misled conclusion. Caspase activation was regarded as a universal marker of apoptosis, thus a fluorescent probe for detecting the activation of caspase with fluorescent microscopy has been developed (**Figure 1-21**)[35]. Caspase, which is a protease, cleaves specific amino acids sequence and the method uses this ability of caspase. The method detecting caspase activation is applicable to living sample with subcellular resolution. However, it requires a careful interpretation of obtained data because FRET signals are usually small. Furthermore, the emission spectrum of YFP (acceptor) partially overlaps with that of CFP (donor), which makes it complicated to calculate FRET efficiency.

Electron microscopy (EM) allows the visualization of fine ultrastructural modifications that accompany apoptosis. For example, the chromatin condensation was clearly observed in apoptotic cells by TEM[38]. This morphological feature characteristic of apoptosis only later become visible by optical microscopy. Moreover, the loss of microvilli, which is the finger-like extensions of the plasma membrane on the cell surface, is observed by SEM[39]. It is also difficult to detect this feature by other methods. EM is able to detect the features which otherwise cannot be detected, but sample preparation for EM is very laborious and requires trained personnel (see section 1-1-2).

Immunoblotting (also known as western blotting) is the method using antibody specific for target and has also been widely employed to detect apoptosis-related phenomena, including caspase activation, cleavage of caspase substrates and release of Smac protein from mitochondria into cytosol (see **Figure 1-18**). Caspase changes its conformation upon activation, so it is possible to detect apoptosis by recognizing active caspase with antibody specific for active caspase. As illustrated in **Figure 1-21**, caspase cleaves proteins on specific site and hence the proteins (substrates) cleaved by caspase can be used as the marker of apoptosis. In this experiment, degraded substrates are detected, indicating the induction of apoptosis. In addition, immunoblotting allows the study of subcellular fractions. Release of Smac from mitochondria can be accessed by using Smac-specific antibody in both cytosol fraction and mitochondrial fraction. Immunoblotting is useful method for analyzing apoptosis, but it is not applicable to living sample and the loss of information on localization of the target is inevitable.

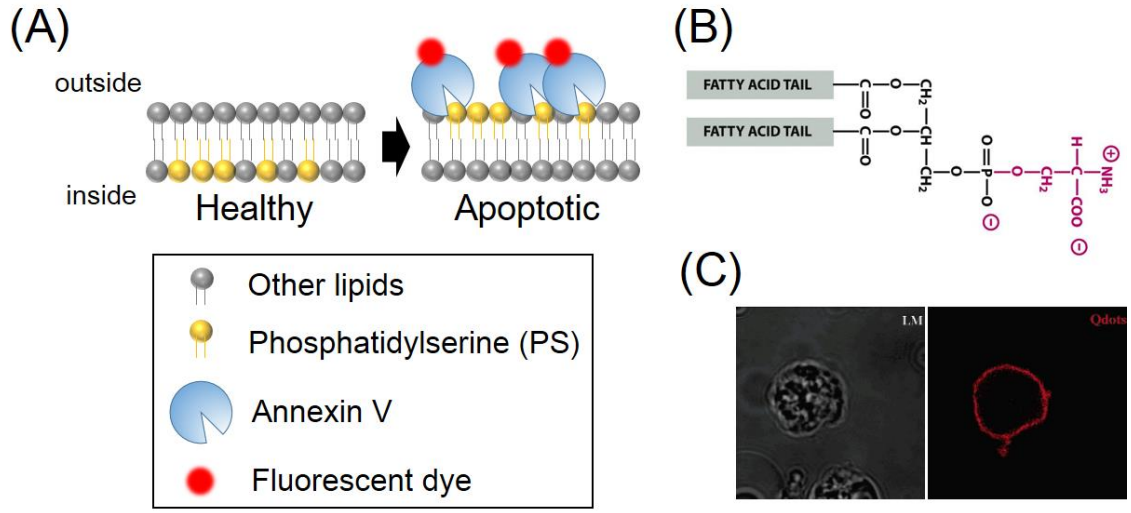

Figure 1-20. Phosphatidylserine (PS) staining.

(**A**) Principle of PS staining for detecting apoptosis. PS is located in the inner leaflet of the plasma membrane in healthy cells, but it flips to the outer leaflet in apoptotic cells. Apoptosis is detected with fluorescence microscopy by observing the fluorescence signal from fluorescent dye fused to Annexin V, which specifically recognizes PS. (**B**) Structure of PS. (**C**) Example of PS staining[34]. Apoptotic human promyelocytic leukemia cells was stained with red fluorescent dye-labelled Annexin V. Periclinal fluorescence indicates that PS exposed on plasma membrane was visualized.

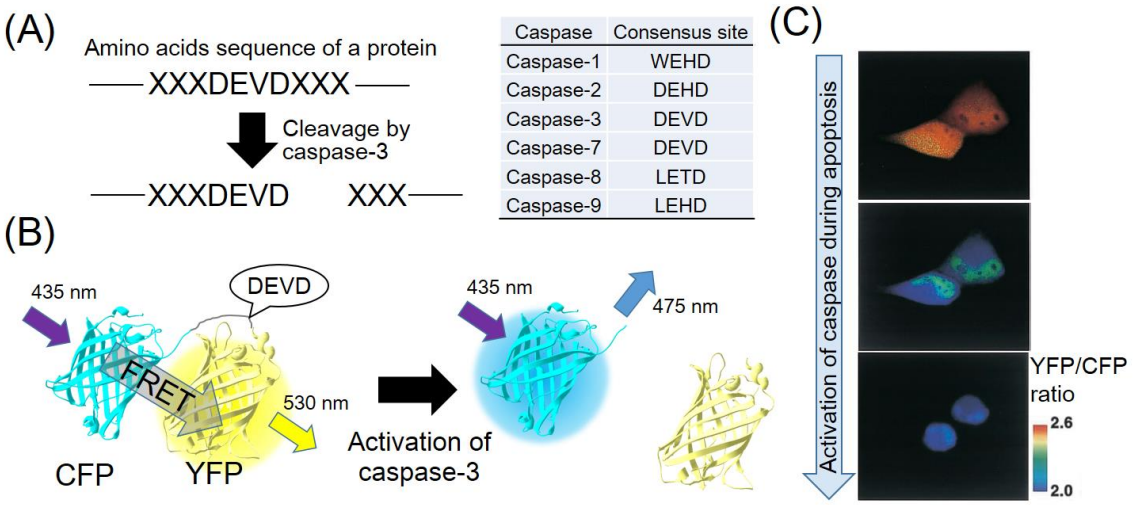

Figure 1-21. Detection of caspase activation by fluorescence resonance energy transfer (FRET).

(**A**) Caspase mainly responsible for apoptosis cleaves specific amino acids sequence (consensus site). Table shows consensus site of each caspase[36]. D: aspartic acid, E: glutamic acid, V: valine, W: tryptophan, H: histidine, L: leucine, X: any amino acids. (**B**) Principle of the detection of caspase activation. The probe is composed of cyan fluorescent protein (CFP) connected with yellow fluorescent protein (YFP) by a short linker containing cleavage site of caspases. In normal condition, fluorescence resonance energy transfer (FRET) occurs, resulting in the detection of emission of YFP. In apoptotic condition, the linker is cleaved by activated caspase and then FRET efficiency dramatically decreases. (**C**) Pseudo-color images represent FRET efficiency (YFP/CFP ratio) in apoptotic cells[37]. As apoptotic process proceeds, fluorescence signal of YFP decreases, leading to the decrease in the ratio (= FRET efficiency).

1-3-2. Characterization of protein clusters responsible for apoptosis

Upon apoptotic stimulation in both extrinsic and intrinsic pathway, Bak protein is oligomerized to form a cluster on mitochondrial outer membrane, leading to the release of Smac from mitochondria into cytosol and the induction of apoptosis. Because the formation of Bak cluster on mitochondria is of crucial importance in inducing apoptosis, the characterization of the cluster is essential in order to understand the mechanism of apoptosis. To date, two methods for characterizing Bak clusters have been mainly reported. First, fluorescence microscopy is used to investigate the localization and the size of Bak clusters (**Figure 1-22A**). In this method, fluorescent-labelled Bak molecules introduced in cells are observed under fluorescence microscopy. The method provides the information on the subcellular localization and the size of Bak clusters in living sample. However, the precise access to the information is prevented by the limitation of spatial resolution in fluorescence microscopy (known as the diffraction limit, see section 1-1-1) because the size of Bak cluster is smaller than the diffraction limit (approximately 250 nm). Second, immunoblotting serves as a method to detect Bak oligomerization (**Figure 1-22B**). In this method, Bak molecules in cells are cross linked with each Bak molecules by cross-linker reagent such as bismaleimidohexane (BMH), and then they are detected by Bak-specific antibody. As a result, dimers and higher order oligomers as well as monomers are detected in apoptotic cells whereas only monomers are detected in healthy cells. Immunoblotting is able to detect Bak oligomers responsible for inducing apoptosis with high sensitivity, but it requires lysate of cell sample, resulting in the loss of the information on the localization. Moreover, it should be kept in mind that the data obtained in immunoblotting represent the average of whole cell population, which does not reflect intercellular heterogeneity such as the variety of the cluster size between cells.

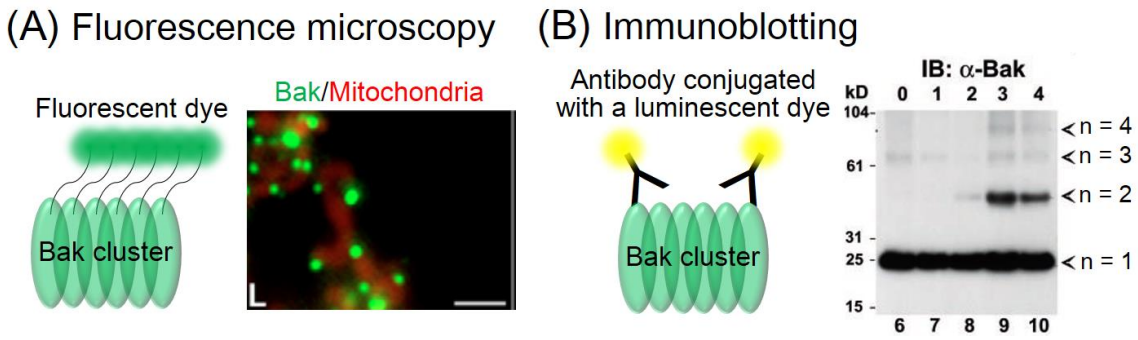

Figure 1-22. Currently available methods for characterizing Bak clusters.

(**A**) Fluorescence microscopy[40]. In this method, a fluorescent-labelled Bak in introduced into cells and its fluorescence is observed under a fluorescence microscope. Punctate fluorescence (green) indicates a cluster composed of Bak molecules on mitochondria (red). Scale bar: 2 μm. (**B**) Immunoblotting[41]. In this method, proteins included in lysate of cells expressing Bak are transferred to a nitrocellulose membrane and treated with Bak-specific antibody conjugated with a luminescent dye. Black bands represent the luminescence signal and n indicates the degree of polymerization. Only monomer is detected in healthy cells (lane 0−1), whereas oligomers are detected in apoptotic cells (lane 2−4).

1-4. Purposes of the present study

1-4-1. Development of a method for visualizing apoptosis *in vivo*

Apoptosis plays an important role in homeostasis in animal body, and its dysfunction causes numerous serious diseases such as cancer. The in-depth investigation of apoptosis and its mechanisms is utmost importance in fundamental and applied biomedical research because the knowledge obtained by the investigation has tremendous implications for the development of novel therapeutic agents. Thus far, dozens of methods have been reported to analyze apoptosis (see section 1-3-1, **Figure 1-23**). However, most of previously reported methods require destructive sample preparation such as fixation and lysis, or are applicable to only culture cell. Destructive methods are not applicable to living sample and the method limited to culture cell is not able to analyze apoptosis with tissue and whole body level. Practically, apoptosis occurs in live multi-cellular organisms, therefore it is essential to investigate live multicellular organisms in order to elucidate the detailed mechanism of apoptosis. To achieve the goal, one of the purposes of this study is the development of a method for visualizing apoptosis in a live animal (*in vivo* imaging).

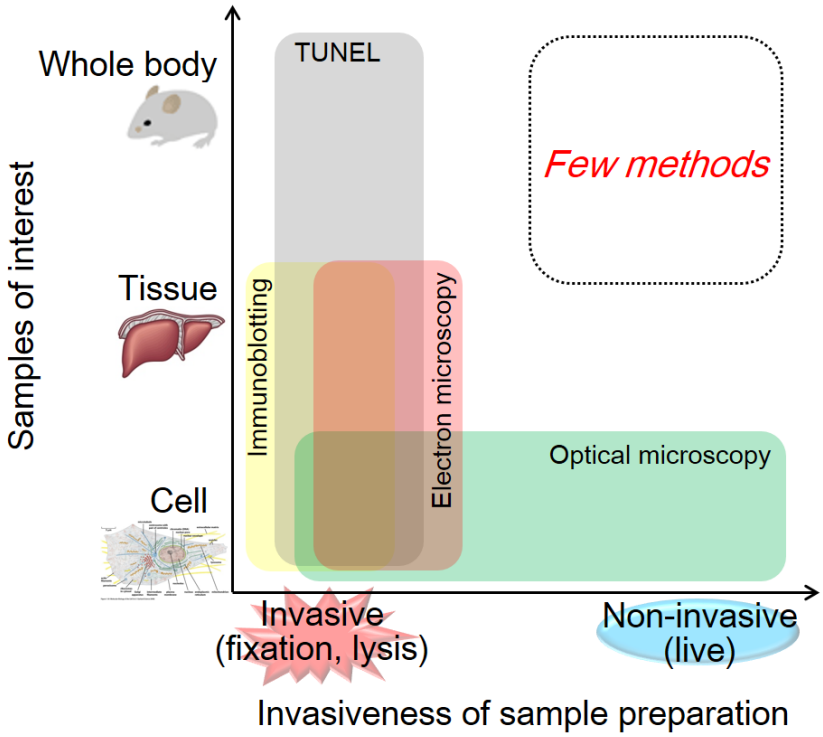

Figure 1-23. Methods for detecting apoptosis.
Sample condition and invasiveness of sample preparation of previously reported methods for detecting apoptosis is depicted. These methods require destructive sample preparation such as fixation and lysis, or are applicable to culture cell. To date, few methods can non-invasively examine apoptosis with whole body level. Detailed principle of each method is described in section 1-3-1.

1-4-2. Development of a method for characterizing protein clustering during apoptosis

The formation of Bak cluster on mitochondria leads to the release of Smac from mitochondria into cytosol, resulting in apoptosis (see section 1-2-2). Thus, there has been a great interest in understanding the character of Bak cluster. However, the cluster is too small to be characterized by optical microscopy because the size of Bak cluster is smaller than the diffraction limit (～ 250 nm) of optical microscopy (**Figure 1-24**). To overcome this problem, one of the purposes of this study is the development of a method for characterizing the size and the localization of Bak cluster during apoptosis.

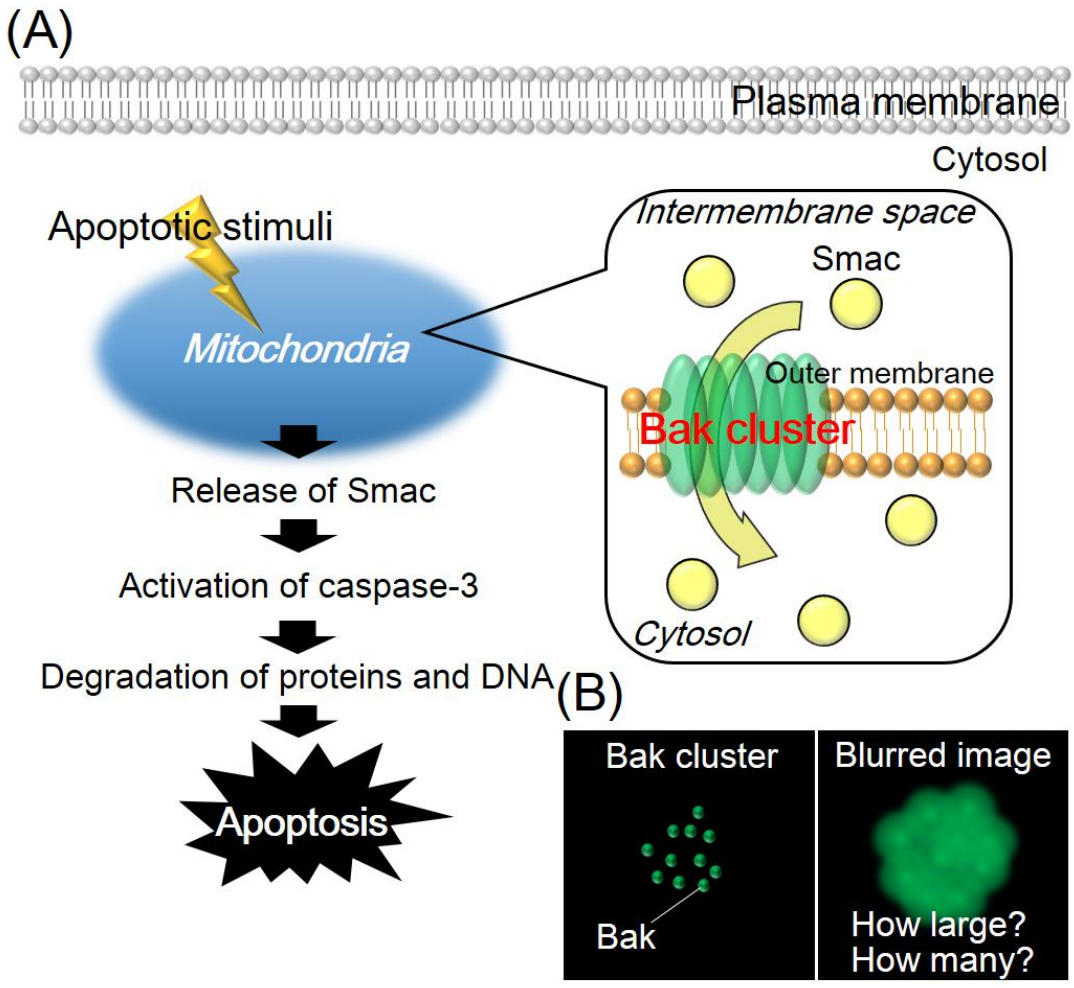

Figure 1-24. Bak cluster is unresolvable by optical microscopy.

(**A**) Signaling pathway during apoptosis. (**B**) Actual distribution of Bak molecules in a cluster (left). Image of the cluster acquired by optical microscopy (right). Conventional optical microscopy, which suffers from the diffraction limit, fails to resolve Bak molecules in the cluster. This is why the size and localization of the cluster cannot be examined by conventional optical microscopy.

1-5. Basic principle used for the present study

1-5-1. Spontaneous complementation of a fluorescent protein

Protein complementation is a reaction in which two-divided protein fragments recover the function by bringing them closely to come together. I used a "spontaneous complementation" of a split fluorescent protein for visualizing apoptosis by detecting apoptosis through Smac release from mitochondria. When a green fluorescent protein (GFP) is divided into two fragments ($GFP_{1–10}$ and GFP_{11}), the fluorescence is lost. Mixing of two fragments of GFP leads to the spontaneous complementation of the GFP irreversibly, resulting in recovery of the fluorescence[42] (**Figure 1-25**). GFP_{11} (C-terminal fragment of GFP) is a small peptide of 17 amino acids, so can be used as an excellent tag for labeling a target molecule because this small tag minimizes the perturbation on folding and solubility of a target molecule. Actually, Stephanie, C. *et al*. demonstrated that GFP_{11} tag is less likely to perturb protein folding and solubility compared to other full-length GFP tags[42].

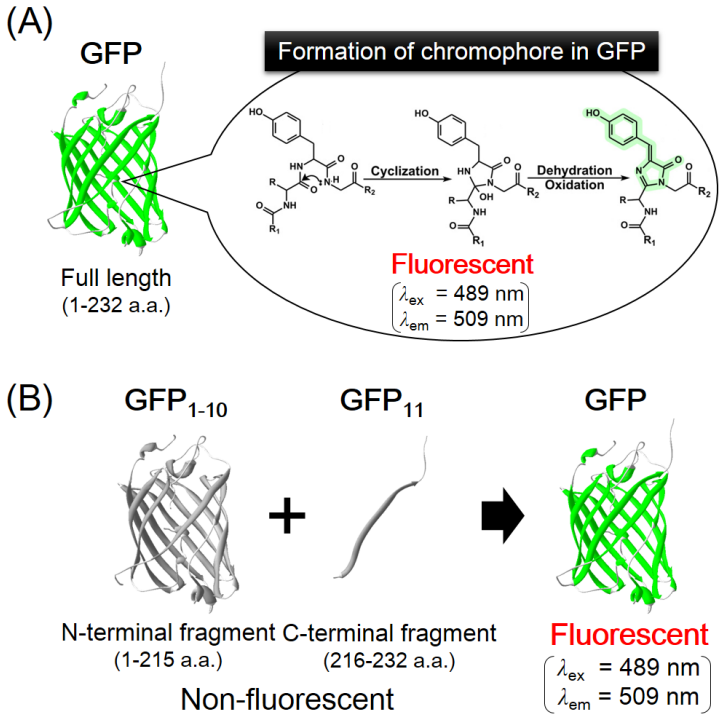

Figure 1-25. Spontaneous complementation of GFP.
(**A**) The β barrel structure of a full length (not split) GFP and the structure of its chromophore[43]. Chromophore of GFP is maturated by several reaction steps of the internal tripeptide Ser65-Tyr66-Gly67. π-electron conjugation, which is the chromophore, is highlighted in green. (**B**) Spontaneous complementation of GFP. Split GFP fragments ($GFP_{1–10}$ and GFP_{11}) fail to form a chromophore and to emit fluorescence. When these fragments are mixed, they are associated with each other to promote the chromophore formation, resulting in the recovery of the fluorescence.

1-5-2. Photo-activated localization microscopy (PALM)

The method for the analysis of Bak clusters is based on photo-activated localization microscopy (PALM), which is one of the optical techniques at the spatial resolution beyond the diffraction limit (**Figure 1-26**). In this method, photo-activatable fluorescent proteins (PA-FPs) such as mEos3 are used to achieve temporal control of the emission. Fluorescent property of mEos3 is converted by violet light called activation light. By illuminating mEos3 molecules distributed in a sample with low intensity of activation light, only a random and sparse subset of mEos3 are activated to red state at any time, allowing these molecules to be imaged individually. These imaged molecules are localized to high precision by determining their centers of fluorescence emission using Gaussian fitting. Repeating this process provides a "super-resolution" image as a summation of rendered images of each fitted molecule in all frames. PALM provides spatial resolution down to a few tens of nanometers. Furthermore, it is possible to count the number of molecules in a region of interest since PALM is based on single-molecule detection. Therefore, PALM is applicable to the characterization of the size, stoichiometry and localization of PA-FP labeled targets.

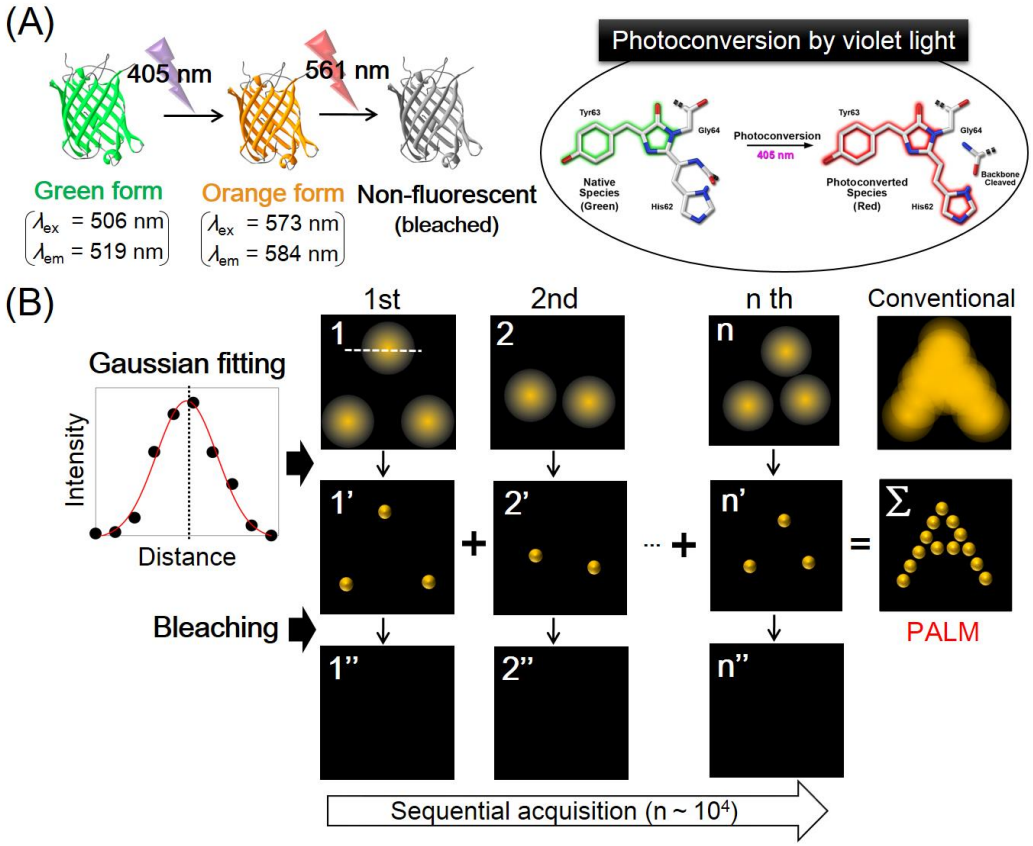

Figure 1-26. Photo-activated localization microscopy (PALM).

(**A**) Fluorescent property and its chemical basis of a photo-activatable fluorescent protein (PA-FP)[44]. PA-FP such as mEos3, which contains His62, Tyr63 and Gly64, changes the color from green to orange in response to violet light that induces cleavage between the amide nitrogen and α-carbon atoms and formation of a longer conjugated system. (**B**) Principle of PALM. The principle is very similar to STORM except that bleaching process included in PALM.

References

1. V.G. Bordo, H.G. Rubahn, *Optics and Spectroscopy at Surfaces and Interfaces* **Chapter 8** (2008).

2. 伊藤敦, *FBNews* **379**, 6−10 (2008).

3. Hamada, K. *et al*. *J*. *Biomed*. *Opt*. **13**, 044027 (2008).

4. 原口徳子, 木村宏, 平岡泰, *生細胞蛍光イメージング*, **第７章・第８章** (2007).

5. Alberts, B. *et al*. *Molecular Biology of the Cell* **Chapter 9** (2008).

6. Allport, J. R. & Weissleder, R. *Exp*. *Hematol*. **29**, 1237−1246 (2001).

7. Paulus, M. J., Gleason, S. S., Kennel, S. J., Hunsicker, P. R. & Johnson, D. K. *Neoplasia* **2**, 62−70 (2000).

8. Kalender, W. A. *Phys. Med. Biol.* **51**, R29−R43 (2006).

9. 国立天文台編, *理科年表* 第 81 冊, 環境部（化学物質・放射線）.

10. Weissleder, R. *Nat*. *Biotech*. **19**, 316−317 (2001).

11. Helmchen, F. & Denk, W. *Nat*. *Methods* **2**, 932−940 (2005).

12. Zipfel, W. R., Williams, R. M. & Webb, W. W. *Nat*. *Biotech*. **21**, 1369−1377 (2003).

13. Evans, C. L. *et al. Proc.Natl.Acad.Sci.USA* **102**, 16807−16812 (2005).

14. Novotny, L. *et al*. *Principles of Nano-optics*, Cambridge University Press (2006).

15. van Zanten, T. S. *et al. Proc. Natl. Acad. Sci. USA* **106**, 18557−18562 (2009).

16. Gustafsson, M. G. *Proc. Natl. Acad. Sci. USA* **102**, 13081−13086 (2005).

17. Klar, T. A. & Hell, S. W. *Opt. Lett.* **24**, 954−956 (1999).

18. Betzig, E. *et al*. *Science* **313**, 1642−1645 (2006).

19. Rust, M. J., Bates, M. & Zhuang, X. *Nat. Methods* **3**, 793−795 (2006).

20. Schermelleh, L. *et al. Science* **320**, 1332−1336 (2008).

21. Kukat, C. *et al. Proc. Natl. Acad. Sci. USA* **108**, 13534−13539 (2011).

22. Huang, B., Bates, M. & Zhuang, X. *Annu. Rev. Biochem.* **78**, 993−1016 (2009).

23. Bates, M., Huang, B., Dempsey, G. T. & Zhuang, X. *Science* **317**, 1749−1753 (2007).

24. Alberts, B. *et al*. *Molecular Biology of the Cell* **Chapter 18** (2008).

25. Kerr, J. F. R., Wyllie, A. H. & Currie, A. R. *Br. J. Cancer* **26**, 239−257 (1972).

26. Yuan, J., Shaham, S., Ledoux, S., Ellis, H. M. & Horvitz, H. R. *Cell* **75**, 641−652 (1993).

27. McIlroy, D. *et al. Genes Dev.* **14**, 549−558 (2000).

28. Martinez, M. M., Reif, R. D. & Pappas, D. *Anal. Methods* **2**, 996−1004 (2010).

29. Tait, S. W. & Green, D. R. *et al*. *Nat. Rev. Mol. Cell Biol.* **11**, 621−632 (2010).

30. Gavrieli, Y., Sherman, Y. & Ben-Sasson, S. A. *J. Cell Biol.* **119**, 493−501 (1992).

31. Tait, J. F. & Gibson, D. *Arch. Biochem. Biophys.* **298**, 187−191 (1992).

32. Zwaal, R. F., Comfurius, P. & Bevers, E. M. *Cell. Mol. Life Sci.* **62**, 971−988 (2005).

33. Fischer, K. *et al*. *Blood* **108**, 4094−4101 (2006).

34. Le Gac, S., Vermes, I. & van den Berg, A. *Nano Lett.* **6**, 1863−1869 (2006).

35. Kepp, O., Galluzzi, L., Lipinski, M., Yuan, J. & Kroemer, G. *Nat. Rev. Drug Discov*. **10**, 221−237 (2011).

36. Nicholson, D. W. & Thornberry, N. A. *Trends Biochem. Sci.* **22**, 299−306 (1997).

37. Takemoto, K., Nagai, T., Miyawaki, A. & Miura, M. *J. Cell Biol.* **160**, 235−243 (2003).

38. Galluzzi, L. *et al. Cell Death Diff.* **16**, 1093−1107 (2009).

39. Rello, S. *et al*. *Apoptosis* **10**, 201−208 (2005).

40. Zhou, L. & Chang, D. C. *J. Cell Sci.* **121**, 2186−2196 (2008).

41. Mikhailov, V. *et al. J. Biol. Chem.* **278**, 5367−5376 (2002).

42. Cabantous, S., Terwilliger, T. C. & Waldo, G. S. *Nat. Biotech.* **23**, 102−107 (2005).

43. Pakhomov, A. A. & Martynov, V. I. *Chem. Biol.* **15**, 755−764 (2008).

44. Shaner, N. C., Patterson, G. H. & Davidson, M. W. *J. Cell Sci*. **120**, 4247−4260 (2007).

Chapter 2

Development of a Method for Visualizing Apoptosis *in vivo*

2-1. Introduction

Multicellular organisms have intrinsic mechanisms for cell death. One such mechanism, apoptosis, plays a crucially important role in early development, homeostasis, and immunity in organisms[1]. Abnormalities in apoptosis cause several incurable diseases including cancer, autoimmunity, and neurodegenerative disorders[2]. Consequently, *in situ* visualization of apoptosis in multicellular organisms is necessary to advance our understanding of the machinery for these apoptosis-related diseases. To date, several methods for visualizing apoptotic cells in animals have been developed. Electron microscopy detects alterations in cell morphology such as blebbing and chromatin condensation, which are distinctive of apoptotic cells[3]. Immunostaining enables visualization of apoptotic cells using antibody specific for proteins involved in apoptosis[4]. However, these methods are applicable only to fixed tissues. Development of new methodologies that enable the detection of apoptosis in live animals has remained a challenge.

Fluorescent proteins are useful tools for visualizing target proteins *in vivo*[5,6]. The proteins label the target in a genetically encoded manner, enabling observation of the target specifically and less-invasively. In addition, the genetically encoded probe can be expressed in any specific tissue such as liver and muscle using tissue-specific promoters. For *in vivo* application, this feature constitutes an attractive advantage over chemical probes. Because of these benefits, several probes based on fluorescent proteins have been developed for detecting apoptosis *in vivo*[7,8], many of which use full-length fluorescent proteins. However, they emit fluorescence irrespective of cellular condition, resulting in high background signals and complicated data analysis. To overcome this difficulty, novel probes that emit fluorescence upon the existence of apoptotic cells are required.

Here I describe a genetically encoded fluorescence-activatable probe for imaging apoptosis *in vivo* based on spontaneous complementation of GFP variant (GFP OPT) fragments[9]. Applying the complementation technique to the early event of apoptosis, I demonstrate that the probe emits fluorescence upon apoptosis in living cells. Useful applicability of the developed probe is shown with living zebrafish.

2-2. Materials and Methods

2-2-1. Construction of plasmids

All genes were amplified by PCR using PrimeSTAR DNA polymerase and customized specific primers. The cDNA of $GFP_{1–10}$ was generated by PCR using a template cDNA of GFP OPT. The cDNA of Smac was amplified from mouse cDNA library. Smac-GFP_{11} was developed by linking cDNA of Smac and GFP_{11} connected to FLAG epitope (DYKDDDDK) generated by oligonucleotide annealing. The cDNA of $GFP_{1–10}$ and Smac-GFP_{11} were subcloned into pCold for *in vitro* experiments, pcDNA4/V5-HisB for culture cell experiments or pBS including EF1 promoter for zebrafish experiments.

2-2-2. Protein purification

An *E. coli* strain BL21 transformed with Smac-GFP_{11} or $GFP_{1–10}$ in pCold vector was incubated at 37°C for 3 h, following at 15°C with 1 mM IPTG (isopropyl β-D-1-thiogalactopyranoside) for 24 h. The cells were harvested by centrifugation at 4°C. Then the pellets were resuspended in 50 mM Tris buffer (pH 7.4) containing 100 mM NaCl and 1% Triton X-100. The cells were lysed by sonication and centrifuged to obtain the crude proteins in the supernatant. The proteins were purified using Ni^{2+} affinity chromatography (GE Healthcare, Little Chalfont, Buckinghamshire, UK) according to the manufacturer's instructions. The fractions containing Smac-GFP_{11} or $GFP_{1–10}$ protein were harvested and then their concentrations were measured based on the bicinchoninic acid (BCA) method using a BCA Assay Kit (Pierce Biotechnology Inc., Rockford, IL). Expression and purity of these proteins were investigated using SDS-PAGE analysis.

2-2-3. *In vitro* complementation assay

Complementation of the purified Smac-GFP_{11} with the purified $GFP_{1–10}$ was measured *in vitro*. A large excess (6.35 nmol) of Smac-GFP_{11} (127 μM in 50 mM Tris buffer containing 100 mM NaCl, pH 7.4) was added to 68.6 pmol of $GFP_{1–10}$ (68.6 μM in 50 mM Tris buffer containing 100 mM NaCl, pH 7.4). The fluorescence spectrum was measured at 25°C using a spectrofluorometer (F-4500; Hitachi Ltd., Japan). Excitation wavelength of this assay was set at 480 nm.

2-2-4. Cell culture, transfection and induction of apoptosis

HeLa cells were cultured in DMEM (high glucose) supplemented with 10% FBS, 100 unit/ml penicillin and 100 μg/ml streptomycin. HeLa cells were incubated at 37°C in 5% CO_2 atmosphere. Z3 cells originated from zebrafish were cultured in L15 medium supplemented with 10% FBS, 100 unit/ml penicillin and 100 μg/ml streptomycin. Z3 cells were incubated at 30°C. Plasmids were transfected into cells with Lipofectamine 2000 reagent. To induce apoptosis, cells were irradiated with UV light (254 nm) using an ultraviolet cross-linker (CL-1000; UVP LLC, Upland, CA). Energy levels of UV irradiation were set at 14 mJ/cm^2 and 200 mJ/cm^2 in experiments of culture cells and zebrafish embryos, respectively.

2-2-5. Western blot analysis

HeLa cells transiently transfected with Smac-GFP_{11} and $GFP_{1–10}$ were seeded in 35 mm dishes. After UV irradiation as apoptotic stimulation, the cells were collected by scratching with scrapers and the cytosolic fractions were separated using a digitonin-based subcellular fractionation technique[10]. The proteins were subjected to SDS–PAGE using 10% polyacrylamide gels and were subsequently transferred to a nitrocellulose membrane. After blocking with 1% skim milk in a TBST buffer (50 mM Tris-HCl pH 8.0, 150 mM NaCl, 0.05% Tween-20), the membrane was blotted with a monoclonal anti-FLAG antibody at dilution 1/1000 overnight at 4°C. The membrane was then washed three times with TBST and incubated with anti-mouse IgG conjugated with horseradish peroxidase (HRP) at dilution 1/5000 for 1 h at 25°C. After washing the membrane three times with TBST, the proteins were detected using SuperSignal West Femto Maximum Sensitivity Substrate and a mini CCD camera (LAS 4000; GE Healthcare, Little Chalfont, Buckinghamshire, UK). Subsequently, the membrane was reprobed by anti-β-actin antibody (Sigma-Aldrich Corp.) followed by an HRP-conjugated anti-mouse IgG antibody for β-actin detection. Western blot analysis of zebrafish embryo was performed as described previously[11].

2-2-6. Immunofluorescence analysis

After UV irradiation for apoptotic stimulation and subsequent treatment with Mitotracker Red CMXRos to stain mitochondria, HeLa cells on a cover glass were fixed with 4% paraformaldehyde in phenol red free DMEM at 37°C for 10 min. The cells were washed with

PBS and were permeabilized with 0.2% Triton X-100 in PBS for 5 min at 25°C. Cells were then washed with PBS and blocked by 0.2% fish skin gelatin (FSG) in PBS for 1 h at 25°C. The buffer was exchanged to 0.2% FSG in PBS containing 1/1000 dilution of mouse anti-FLAG monoclonal antibody and 1/500 dilution of rabbit anti-GFP polyclonal antibody. Subsequently, the cells were incubated with the buffer overnight at 4°C. After washing with PBS, the cells were incubated with 0.2% FSG in PBS containing 1/2000 dilution of a goat anti-mouse antibody conjugated with Alexa488 and 1/2000 dilution of a donkey anti-rabbit antibody conjugated with Alexa647 for 1 h at 25°C. The cells were washed with 0.2% FSG in PBS and mounted on a slide glass with FluorSave Reagent. Fluorescence images of the samples were acquired using a laser scanning confocal microscope. For immunostaining of a zebrafish cell line, Z3 cells were fixed with 4% paraformaldehyde in phenol red free L15 medium at 30°C for 10 min. Subsequent procedures for immunostaining of Z3 cells were the same as HeLa cells except for the absence of anti-GFP primary antibody and anti-rabbit secondary antibody.

2-2-7. Live-cell imaging

HeLa cells expressing Smac-GFP_{11} and $GFP_{1–10}$ were treated with 0.5 μM TMRE. The cells were washed with DMEM. Then an observation medium (HEPES-buffered DMEM phenol red free, 10% FBS, pH 7.2) was added. After UV irradiation as an apoptotic stimulation, fluorescence time-lapse images of the cells were acquired every 5 min using a laser scanning confocal microscope (IX81-FV1000-D; Olympus Corp.) equipped with UPlanSApo 100×, 1.40 N.A. oil immersion objective. The cells on the stage were kept at 37°C using a stage incubator (Tokai Hit Corp.) The acquired images were analyzed using ImageJ software.

2-2-8. Protein alignment and calculation of isoelectronic point

Amino acids sequences of zebrafish Smac (zgc63938 and zgc158776) were obtained from the National Center for Biotechnology Information (NCBI). Alignment of amino acid sequences of Smac protein between mouse and zebrafish was performed using BLAST[12]. Theoretical isoelectronic points (pI) of proteins were calculated using the Compute pI/MW program from the ExPASy[13].

2-2-9. *In vitro* synthesis of mRNA for microinjection

The cDNA of $GFP_{1–10}$ and SmacΔ-GFP_{11}, in which the mitochondrial signal of Smac was

deleted, were subcloned into pCS2+ including SP6 promoter. mRNA of $GFP_{1–10}$ and SmacΔ-GFP_{11} were transcribed *in vitro* and extracted using mMESSAGE mMACHINE Kit according to the manufacturer's protocol. Injection of the mRNAs was performed as described previously[14].

2-2-10. Zebrafish maintenance

Zebrafish were maintained fundamentally as described in "The Zebrafish Book" [15]. For the generation of transgenic zebrafish, the constructs of Smac-GFP_{11} and $GFP_{1–10}$ were linearized by *I-sceI* meganuclease and injected into embryos at the 1–2 cell stage, as described previously[16]. The transgenes in zebrafish were validated by genotyping of extracted genomic DNA.

2-2-11. TUNEL assay

Dechorionated zebrafish embryo was washed with PBS and fixed with 4% paraformaldehyde in PBS overnight at 4°C. The embryo was washed with PBST buffer (0.05% Tween-20 in PBS) and incubated with 100% methanol for 5 min at 25°C. After the methanol was exchanged to fresh 100% methanol, the embryo was incubated overnight at -30°C. The methanol was exchanged to 66% methanol and the embryo was incubated for 5 min at 25°C. Next, 66% methanol was exchanged to 33% methanol and the embryo was incubated for 5 min at 25°C. The embryo was washed with PBST buffer and the embryo was permeabilized with 0.1% sodium citrate/0.1% Triton X-100 for 15 min at 25°C. The buffer for permeabilization was replaced by 1 μg/ml proteinase K in a PBST buffer. The embryo was incubated for 15 min at 25°C. After the embryo was washed with PBST buffer, a Tdt-mediated dUTP nick end labeling (TUNEL) was performed using *In Situ* Cell Death Detection Kit according to the manufacturer's instructions. Nuclei of the embryo were labeled with Hoechst dye. Finally, the embryo was observed with a confocal microscope equipped with UPlanSApo 30×, 1.05 N.A. silicon oil immersion objective for fluorescence imaging.

2-3. Results

2-3-1. Basic concept of fluorescent probes for detecting apoptosis

Smac is released from mitochondria into cytosol during apoptosis[17]. To visualize the event in the apoptosis, I developed genetically encoded fluorescent probes based on the spontaneous complementation of protein fragments derived from GFP OPT; $GFP_{1–10}$ (1–215 residues) and GFP_{11} (216–232 residues)[9]. Reportedly, the nonfluorescent fragment of $GFP_{1–10}$ spontaneously associates with GFP_{11}, resulting in the correct folding and formation of the chromophore. Based on the complementation property of the GFP-OPT fragments, I designed a fluorescence-activatable probe for imaging the release of Smac from mitochondria (**Figure 2-1**). A carboxy terminal end of Smac is connected with GFP_{11} (Smac-GFP_{11}), which is located in the mitochondrial intermembrane space. In contrast, the remainder of $GFP_{1–10}$ localizes in cytosol. The GFP-OPT fragments are separated by the mitochondrial membrane under an unstimulated condition, and are thereby prevented from spontaneous complementation. Upon apoptotic stimulation such as UV light, Smac-GFP_{11} is released from mitochondria into the cytosol, resulting in colocalization with $GFP_{1–10}$. It engenders complementation of the fragments and the recovery of fluorescence. The present approach therefore enables detection of apoptosis via Smac release with a high signal-to-background ratio.

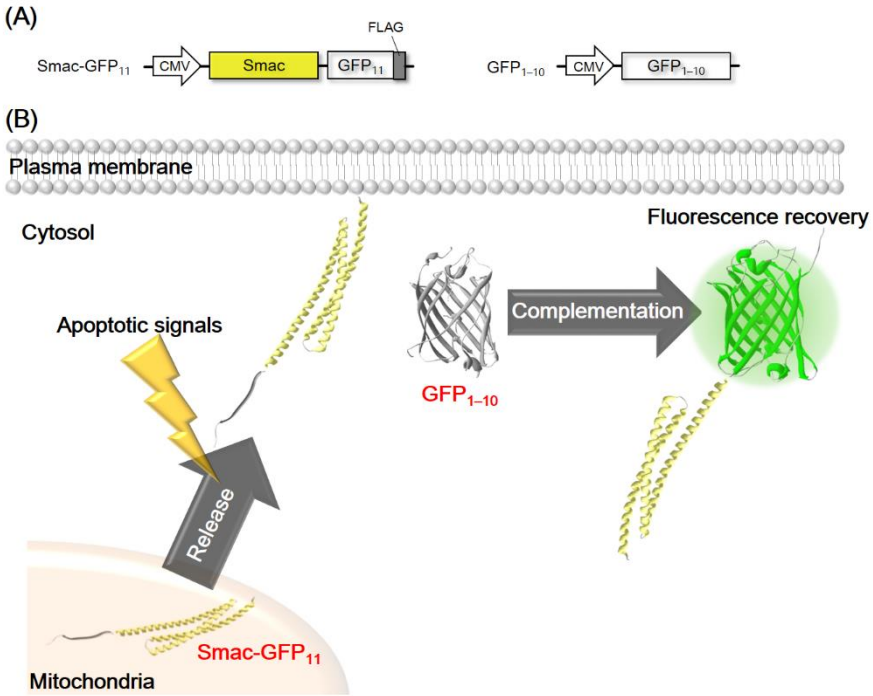

Figure 2-1. Design of the probe.

(**A**) Schematic constructs of the probes. CMV denotes a cytomegalovirus promoter for expression in mammalian cells. Gray square in the construct shows a FLAG tag. (**B**) Upon apoptotic stimulation, Smac-GFP_{11} is released from mitochondria into cytosol. It is spontaneously complemented with cytosolic $GFP_{1–10}$, resulting in the recovery of the fluorescence.

2-3-2. Validation of the spontaneous complementation *in vitro*

I first investigated whether Smac-GFP_{11} spontaneously complemented with $GFP_{1–10}$ or not, and thereby whether the fluorescence was recovered *in vitro*, or not. I purified each recombinant protein of Smac-GFP_{11} and $GFP_{1–10}$, and examined temporal changes in emission spectra upon mixing two fragments. In the assays, the fluorescence was clearly recorded when purified $GFP_{1–10}$ was added to a solution including Smac-GFP_{11} (**Figure 2-2A**). The result demonstrated that spontaneous complementation occurred between Smac-GFP_{11} and $GFP_{1–10}$. The emission spectrum was completely identical to that of full-length GFP OPT (**Figure 2-2A**, inset), indicating that the structure of the chromophore in the complemented GFP OPT was identical to that of full-length GFP OPT. Misfolding or aggregation of a GFP_{11}-tagged protein is known to hinder the complementation of $GFP_{1–10}$[9]. Accordingly, the present results *in vitro* suggested that Smac labeled with GFP_{11} did not misfold nor aggregate in the solution but the short fragment of GFP_{11} was exposed on the surface of Smac as illustrated in Figure 2-1B.

To characterize the kinetics of the spontaneous complementation of the probes, I measured the fluorescence intensities as a function of time after mixing Smac-GFP_{11} and $GFP_{1–10}$ (**Figure 2-2B**, white circles). For the kinetic analysis, I developed a model of the complementation based on two-step reactions according to the previous split-GFP study (**Figure 2-3**, **A and B**)[18]. I found that the model has good agreement with the experimental data (**Figure 2-2B**, curve fitting and **Figure 2-3C**), suggesting that the kinetic pathway of the complementation between Smac-GFP_{11} and $GFP_{1–10}$ resembles that of GFP fragments in the previous studies. In contrast, $GFP_{1–10}$ did not recover fluorescence in the absence of Smac-GFP_{11} (**Figure 2-2B**, black circles), ensuring that the probes are applicable to imaging of the Smac release with a high signal-to-background ratio.

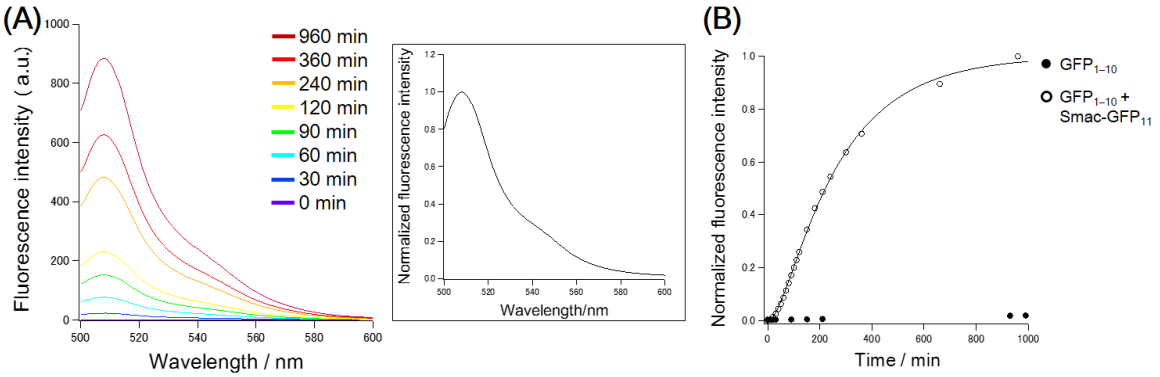

Figure 2-2. *In vitro* characterization of spontaneous complementation of the probes.
(**A**) Temporal changes in emission spectra after mixing of purified $GFP_{1–10}$ (68.6 μM 10 μl, total 68.6 pmol) and Smac-GFP_{11} (127 μM 500 μl, total 6.35 nmol). Inset shows a fluorescence spectrum of full-length GFP OPT. (**B**) Time-dependent fluorescence recovery. Area in the spectra between 500 and 520 nm in (**A**) is shown as a function of time. Fluorescence intensity of $GFP_{1–10}$ only was recorded from 0 min to 210 min and from 930 min to 990 min.

(A)

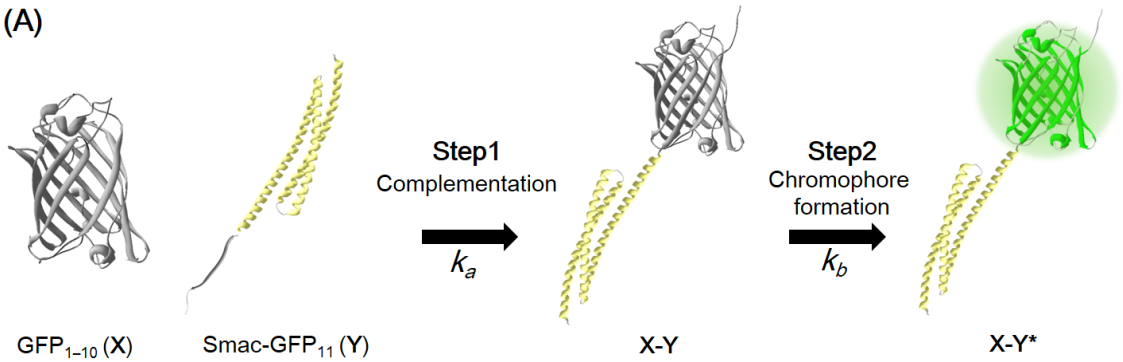

(B)

$$[X]_0 << [Y]_0$$

$$\frac{d[X]}{dt} = -k_a[X][Y] = -k_a'[X] \qquad (k_a' \equiv k_a[Y] \quad \because [Y] \approx const.)$$

$$\frac{d[X-Y]}{dt} = k_a[X][Y] - k_b[X-Y] = -k_a'[X] - k_b[X-Y]$$

$$\frac{d[X-Y^*]}{dt} = k_b[X-Y]$$

$$\therefore \frac{[X-Y^*]}{[X]_0} = 1 - \frac{k_b e^{-k_a't} - k_a' e^{-k_b t}}{k_b - k_a'}$$

(C)

k_a' [min^{-1}]	$t_{1/2,\ step1}$ [min]	k_b [min^{-1}]	$t_{1/2,\ step2}$ [min]	R^2
(2.02 ± 0.14) × 10^{-2}	34 ± 2	(4.15 ± 0.12) × 10^{-3}	167 ± 5	0.99893

Figure 2-3. Kinetic analysis of spontaneous complementation of the probes.
(**A**) Schematic illustration of spontaneous complementation between the probe molecules. k_a and k_b respectively represent the rate constant in step 1 (complementation) and step 2 (chromophore formation). (**B**) Kinetics of the spontaneous complementation shown in (**A**). The equation shown at right represents a solution for the kinetics. (**C**) Summary of the kinetic analysis. Data are represented with standard errors from the curve fitting.

2-3-3. Analysis of the subcellular localization of the probes

Next, I investigated the subcellular localization of the probes. Immunoblot analysis revealed that the amount of Smac-GFP_{11} in cytosol increased on UV stimulation (**Figure 2-4A**), suggesting that Smac-GFP_{11} was released from mitochondria into the cytosol during apoptosis. Additionally, I directly visualized the localization of the probes with immunostaining analysis (**Figure 2-4B**). The subcellular localization of Smac-GFP_{11} was merged with the localization of mitochondria in the absence of apoptotic stimulation, revealing that the labeling with GFP_{11} did not interfere with the mitochondrial localization of Smac. In contrast, Smac-GFP_{11} upon UV irradiation showed cytosolic localization. Taken all together, these results indicated that Smac-GFP_{11} was released from mitochondria into cytosol upon apoptotic stimulation.

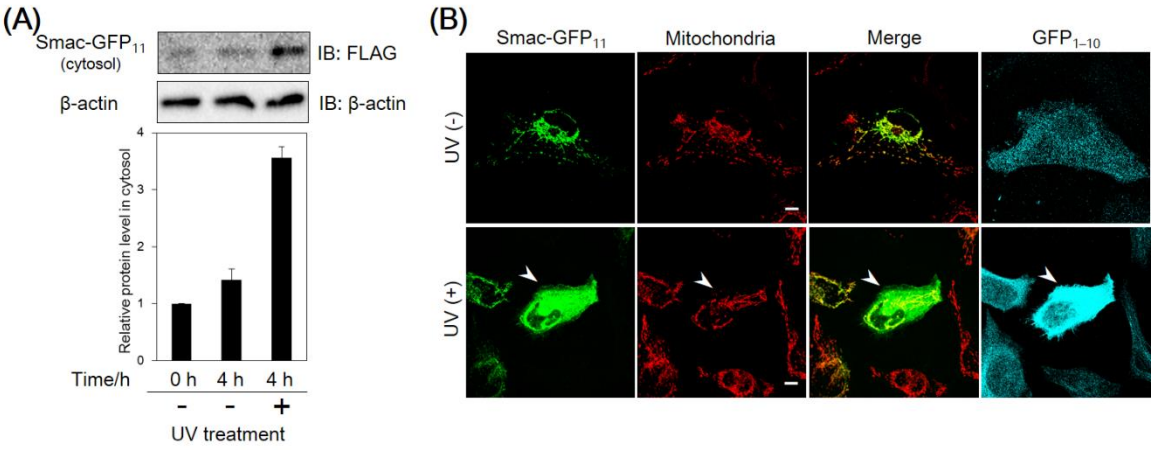

Figure 2-4. Subcellular localization of the probes.

(**A**) Western blot analysis of Smac-GFP_{11} in the cytosolic fraction. HeLa cells expressing Smac-GFP_{11} were subjected to the analysis in the absence and presence of UV stimulation. Data are presented as mean ± s.e.m. (n = 3). (**B**) Immunostaining of the probes expressed in HeLa cells. Mitochondria were visualized by MitoTracker CMXRos dye. Smac-GFP_{11} and $GFP_{1–10}$ were detected, respectively, using anti-FLAG antibody and anti-GFP antibody. Arrowheads indicate the cell in which Smac-GFP_{11} localizes in cytosol. Scale bars: 10 μm.

2-3-4. Imaging of apoptosis in live cells

To validate the applicability of the probes in living cells, I generated HeLa cells transiently expressing Smac-GFP_{11} and $GFP_{1–10}$, and implemented a time-lapse imaging of the cells after UV stimulation (**Figure 2-5** and **Figure 2-6**). Fluorescence of the complemented GFP OPT emerged at approximately 4 h post UV irradiation and the intensity gradually increased in the cells. The cell morphology remained intact when the fluorescence was emerged, suggesting that Smac was released from mitochondria at an early stage of apoptosis. The cell was fragmented at approximately 14 h after UV irradiation, indicating that the cell underwent apoptosis. In addition to the fluorescence imaging of the probes, I visualized the nucleus DNAs by the Hoechst dye and the mitochondrial membrane potential by the tetramethylrhodamine ethyl ester (TMRE) dye. The multi-color imaging revealed the loss of mitochondrial membrane potential and the condensation of nucleus, phenomena of which are the hallmark of apoptosis[1]. Consequently, these results demonstrated that the probes enabled the detection of apoptosis in the cellular milieu.

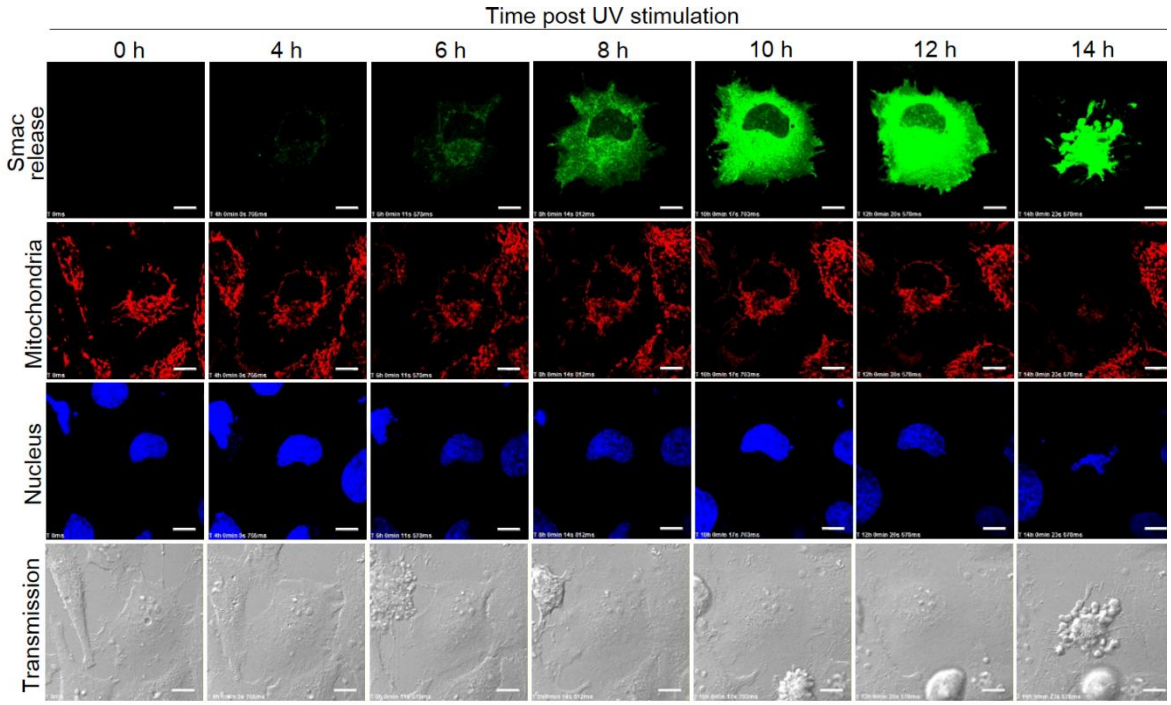

Figure 2-5. Detection of apoptosis in single living cells.

Time-lapse imaging of Smac release (complemented GFP OPT), mitochondrial potential (TMRE dye), nuclei (Hoechst dye) and transmission after UV stimulation. Scale bars: 10 μm.

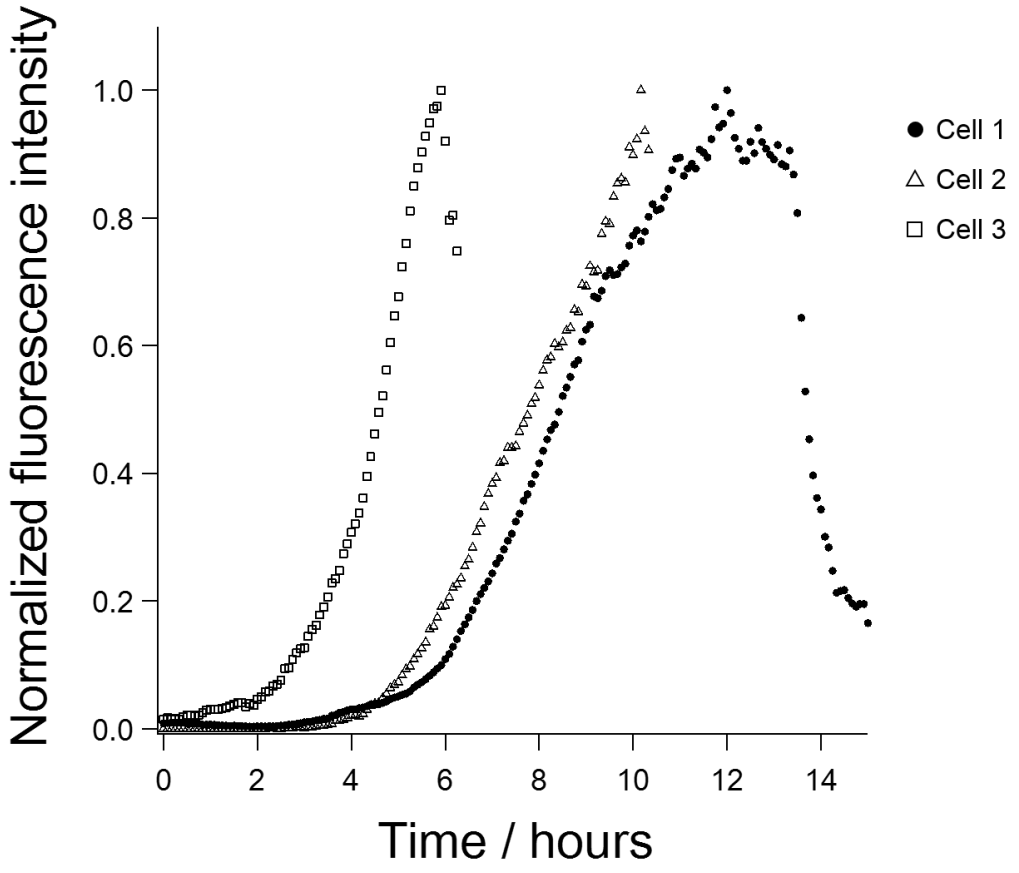

Figure 2-6. Temporal changes in the intensity of the fluorescence during apoptosis.

Fluorescence intensities in UV-stimulated cells were plotted. Cell 1 indicates the cell shown in Figure 2-5.

2-3-5. Imaging of apoptosis in live zebrafish embryos

Zebrafish (*Danio rerio*) has been widely used as a model organism to study apoptosis because the apoptotic signaling pathway is evolutionarily conserved in mammals and zebrafish.[19] Furthermore, the transparent body of zebrafish is suitable for the application of the fluorescence-based probes. Consequently, I chose zebrafish for *in vivo* application of the fluorescent probe. Smac used in the present probe is derived from mouse (*Mus musculus*), whereas zebrafish bears two Smac homologs[19]. To test whether the probe examined in *in vitro* and cell culture experiments is also applicable to zebrafish, I compared amino acid sequences of Smac between mouse and zebrafish (**Figure 2-7**). The alignment analysis revealed that the sequence identity in the mitochondrial signals between mouse and zebrafish is 40% or less. However, isoelectric point (pI) of the mitochondrial signal from mouse Smac is similar to that from zebrafish Smac. In addition, the signal sequence is positively charged (**Figure 2-7**, table), which is a property of many mitochondrial targeting signals leading into mitochondria[20]. Based on this notion, I hypothesized that the present probe derived from mouse Smac might localize in mitochondria in zebrafish. To test this hypothesis, I investigated the subcellular localization of the probe in a zebrafish cell line (Z3 cells) by immunostaining (**Figure 2-8**). The localization of Smac-GFP_{11} was merged with that of mitochondria. Additionally, results show that spontaneous complementation between $GFP_{1–10}$ and GFP_{11} occurred in zebrafish embryo (**Figure 2-9**). Consequently, I concluded that the developed probe is applicable to zebrafish for detecting apoptosis *in vivo*.

```
Smac_mouse          ----------------------MAALR-----SWVTRSVCSLFRYRQRFPVLANSKKRCFSELIKPWHKTVLTG
Smac_zebra63938     MQAVKNCGLCASGSFLKGRTDFLLARRNMAVLRMSAACVQLLKHKTSVLCNSSVHQRILQRLPNVARSNAVPF
Smac_zebra158776    ---------------FII-LTSMAAYRRKLFAAGLSYAASLLSSGGS---CQAG---RRLFLLPGIFRKHWRTI

Smac_mouse          -FGMTLCAVPIAQKSEPHSLSNEALMRRAVSLVTDSTSTFLSQTTYALIEAITEYTKAVYTLVSLYRQYTSLI
Smac_zebra63938     SVGTGLCAVPFTQQVE--NLSHESLIRRASCLVTDSANTYLSQTTLALVDALTQYAKALHTLISLQKRYIASI
Smac_zebra158776    SVTGAICAVPFLQKPE--NLSHEDLVRRASSLVTDSANTFLSQTTLALIDSFTGYIKAVNILVELHKQYEASI

Smac_mouse          GKMNSQEEDEVWQVIIGARVEMTSKQQEYLKLETTWMTAVGLSEMAAEAAYQTGADQASITARNHIQLVKSQV
Smac_zebra63938     GKLSPVEEDSIWQVIIGQRVEVSDRLEECKRFESNWMNAINICELSAEAAYNSGAEHACTATKTNLQVAQSKV
Smac_zebra158776    SKFTPEEENAIWKVILGQRQEVIGRRKNCTHFESCWMTAVNLSQQAAEAAFNAGADQASVAAQSSLQVAQSQV

Smac_mouse          QEVRQLSQKAETKLAEAQTKELHQKAQEVSD---EGADQEEEAYLRED
Smac_zebra63938     EEIRKISKEAEKKLAETKAEEIQRMAEYASSIDIHDLEDVPEAYLRED
Smac_zebra158776    EQVKQLMLEAEIQLKDSKAEYSERLQVALS-----EDEDIPDAYLRED
```

		Sequence alignment		pI
		Sequence identity	*E*-value	
Full length	mouse	-	-	6.15
	zebra63938	44%	7×10^{-62}	6.99
	zebra158776	47%	3×10^{-49}	5.88
Mitochondrial signal	mouse	-	-	10.97
	zebra63938	n.s.	n.s.	11.62
	zebra158776	40%	0.37	11.38

Figure 2-7. Alignment of the amino acid sequences of Smac between mouse and zebrafish.
In zebrafish, there are two *Smac* genes coding Smac protein: zebrafish gene collection (ZGC) 63938 and 158776. The sequence highlighted in the red box corresponds to the mitochondrial targeting signal. Blue box shows the predicted mitochondrial targeting signal in zebrafish Smac. The table presents results of the alignment and the calculation of isoelectric point (pI). Comparison of full-length Smac sequences provided a small *E*-value, suggesting that two *Smac* genes in zebrafish had a similar apoptotic function to *Smac* gene in mouse. n.s., not significant.

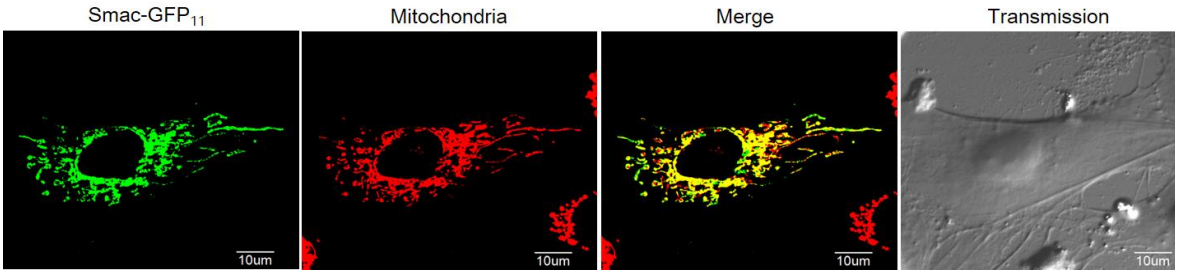

Figure 2-8. Subcellular localization of the probe in zebrafish cell line.

Immunostaining of the probe expressed in Z3 cells. Mitochondria were visualized by MitoTracker CMXRos dye. Smac-GFP_{11} was detected using anti-FLAG antibody. Scale bars: 10 μm.

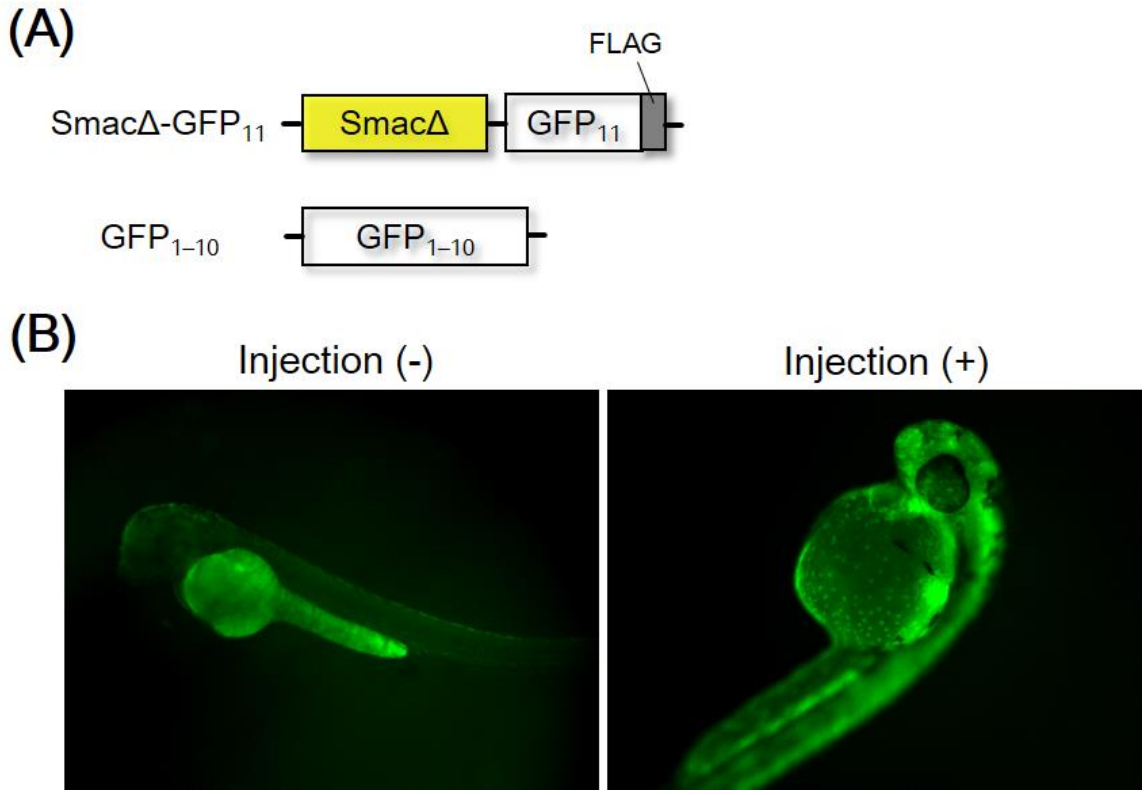

Figure 2-9. Spontaneous complementation *in vivo*.

(**A**) Schematics of mRNAs injected into zebrafish embryos. Zebrafish embryo was injected with synthesized mRNA of $GFP_{1–10}$ and SmacΔ-GFP_{11}, in which mitochondrial targeting signal of Smac was deleted. Both $GFP_{1–10}$ and SmacΔ-GFP_{11} were expressed in cytosol, allowing the spontaneous complementation between them under physiological conditions. (**B**) Fluorescence images of the embryos under a fluorescence stereomicroscope. Yolk in the embryo exhibited autofluorescence.

To detect apoptosis in zebrafish embryo, I generated a transgenic zebrafish in which Smac-GFP_{11} and $GFP_{1–10}$ were expressed ubiquitously (**Figure 2-10**). Fluorescence images of the zebrafish embryo were acquired before and after UV stimulation (**Figure 2-11**). No fluorescence signal of GFP OPT was detected before UV irradiation, whereas bright punctate fluorescence was observed in the embryo after the irradiation. These puncta were observed in the sub-brain region, suggesting that the fluorescence emitted from cells in the brain. To verify that the punctate fluorescence indicated apoptotic cells, I performed the Tdt-mediated dUTP nick end labeling (TUNEL) assays which visualized DNA fragmentation as a marker of apoptosis (**Figure 2-11C**)[21]. Some punctate fluorescent cells in UV-stimulated embryo were merged with the TUNEL-positive cells, demonstrating that the punctate fluorescence indicated apoptotic cells. In this assay, TUNEL-positive cells without fluorescence of GFP OPT were detected, suggesting the existence of apoptosis via signaling pathway other than Smac release in UV-stimulated zebrafish[22]. I also observed TUNEL-negative cells which emitted the fluorescence of GFP OPT. TUNEL detects DNA fragmentation at a late stage during apoptosis[1]. Therefore, the TUNEL-negative fluorescent cells might originate from the cells at an early stage during apoptosis. Collectively, these results demonstrate that the probes enabled detection of apoptotic cells *in vivo*.

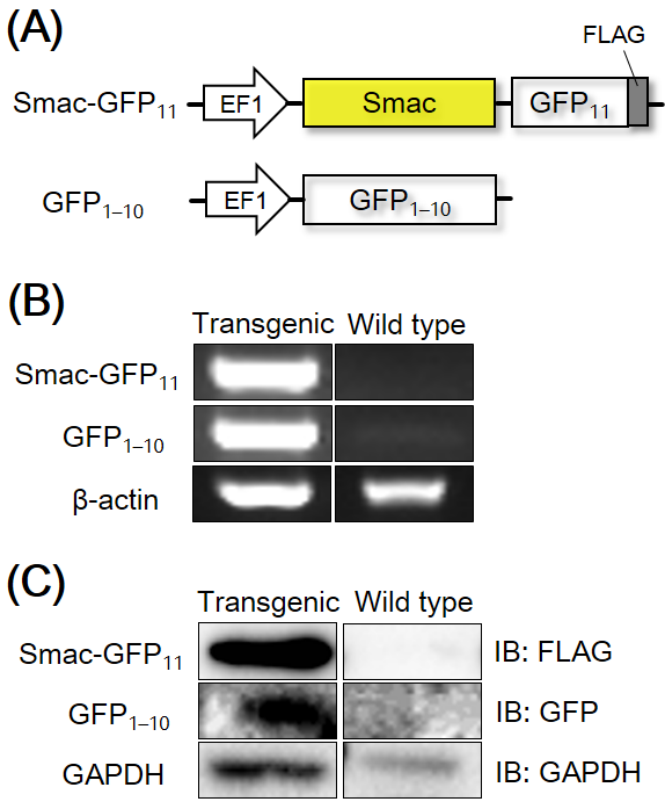

Figure 2-10. Development of the transgenic zebrafish.

(**A**) Schematic constructs of the probes. EF1 denotes an elongation factor-1 promoter for ubiquitous expression in zebrafish. (**B**) Genotyping of zebrafish by polymerase chain reaction (PCR) using the probe-specific primers. β-actin was used as an internal control. (**C**) Western blot analysis for investigating the expression of the probes in zebrafish. Glyceraldehyde 3-phosphate dehydrogenase (GAPDH) was used as an internal control.

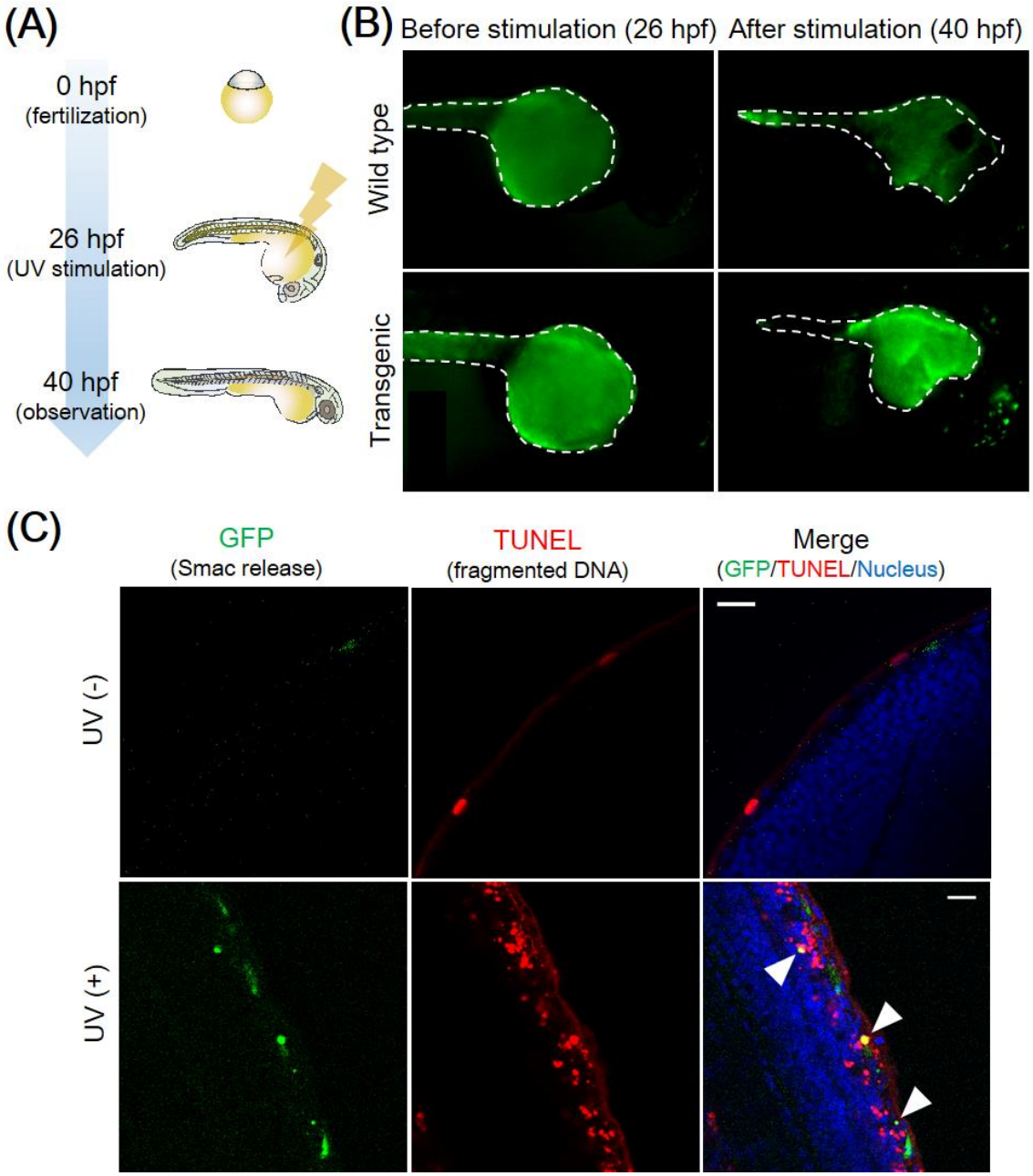

Figure 2-11. Detection of apoptosis in living zebrafish embryo.

(**A**) Schematic procedure for detection of apoptosis in zebrafish embryo: yolk is shown as yellow; hpf, hours post fertilization. (**B**) Fluorescence images of live zebrafish embryos. White dotted lines show the region of yolk emitting autofluorescence. (**C**) TUNEL assay in transgenic zebrafish. Fluorescence images of Smac release (complemented GFP OPT) and TUNEL in transgenic zebrafish. Nuclei were visualized by Hoechst dye. Arrowheads indicate the cells in which the fluorescence of GFP OPT was merged with that of TUNEL. Scale bars: 20 μm.

2-4. Discussion

I developed a fluorescence probe for visualizing apoptotic cells *in vivo* using spontaneous complementation of GFP-OPT fragments. A strong advantage of the probe is that apoptotic cells can be visualized *in vivo* with a high signal-to-background ratio because the fluorescence is activatable only upon the Smac release. A few reports have described genetically encoded fluorescence-based probes for detecting apoptosis in living animals[7,8]. A representative probe is based on Förster resonance energy transfer (FRET), which serves as a useful tool by measuring the activity of protease such as caspase-3 responsible for apoptosis. Recent development of various fluorescent proteins has dramatically improved the change in FRET signals, expanding the applicability of FRET-based probe[23]. However, careful interpretation of the data is often needed because of fluorophore crosstalk[24]. In contrast, the present probe enables detection of apoptosis as significant increases in the fluorescence signal. Consequently, it requires no complicated data analysis. Accurate identification of the timing of Smac release during apoptosis is difficult in the present method owing to the slow rate of fluorescence recovery. However, the release of Smac is an early stage of apoptosis, enabling acquisition of the fluorescence signal during apoptosis. This is a strong advantage of the present activatable probe when it is applied for *in vivo* experiments. Recently, an intriguing method of caspase-3 detection based on GFP-fragment complementation has been reported[25]. One fragment was composed of a recognition sequence of caspase-3, which was cyclized by protein splicing. When caspase-3 cleaved the cyclic fragment, it complemented the remainder of GFP fragment, thereby recovering the fluorescence. The concept is elegant but the possible application in living cells and animals remains a challenge. Another approach reported previously is direct visualization of apoptosis-related factors such as phosphatidylserine[7]. In this approach, fluorescent protein-labeled Annexin V allows for visualizing phosphatidylserine in apoptotic cells because of high affinity of Annexin V for the phospholipid. However, the full-length fluorescent protein emits fluorescence even in the absence of phosphatidylserine, yielding high background signals. The probe developed in this study overcomes such background issues using spontaneous complementation of GFP-OPT fragments.

Another benefit of the present probe is the small size of the GFP_{11} tag, which comprises only 17 amino acids. Fluorescence imaging generally requires labeling of a target protein with fluorophores. Consequently, investigation of the functionality of the target is prerequisite before its visualization or imaging in a physiological context. Actually, the release of Smac from mitochondria into cytosol has been investigated by its labeling with a full-length fluorescent protein (FP)[26]. Reportedly, the kinetics of the release of the FP-tagged protein depended on molecular size of the fusion protein[27]. The molecular size of Smac (26.8kDa) is comparable to that of full-length fluorescent protein (27.2kDa in the case of GFP), which suggests that the labeling of Smac with the full-length FP perturbs kinetics of the Smac release during apoptosis.

For this study, I labeled Smac with GFP_{11}, which bears only 1.8kDa, minimizing the perturbation of Smac release. The small tag of GFP_{11} for the target enables less-invasive imaging of apoptosis in living cells and animals. On the other hand, overexpression of the probes may perturb the cellular physiology because Smac is a pro-apoptotic protein. To minimize this problem, a technology of genome editing capable of designing endogenous genes may be applicable[28]. Labeling endogenous Smac with the tag of GFP_{11} by genome editing does not disturb the expression level of Smac, thereby improving adverse effects on the normal physiology.

2-5. Conclusion

In conclusion, I developed a genetically encoded fluorescence probe for imaging apoptosis *in vivo* using spontaneous complementation of GFP-OPT fragments. Separately expressing the GFP-OPT fragments in mitochondria and cytosol, I demonstrated that the probes enabled visualization of apoptotic cells with a high signal to background ratio in living cultured cells and animals. The principle of the probe is not limited to the mitochondria-mediated apoptosis. It is also applicable for various events through intracellular organelles. For example, proteases called Cathepsin are released from lysosome into cytosol in an apoptotic pathway[29]. Cytotoxic T lymphocytes induce apoptosis of pathogenic cells by intercellularly releasing proteases called Granzyme into the cells[30]. In such various pathways of apoptosis, the probe design concept drives forward the development of versatile tools for less-invasive imaging of apoptosis *in vivo*, paving the way for additional extensive studies of apoptosis-related diseases using multicellular organisms.

References

1. Danial, N. N. & Korsmeyer, S. J. *Cell* **116**, 205−219 (2004).
2. MacFarlane, M. & Williams, A. C. *EMBO Reports* **5**, 674−678 (2004).
3. Kerr, J. F., Wyllie, A. H., Currie, A. R. *Br. J. Cancer* **26**, 239−257 (1972).
4. Gown A. M., Willingham M. C. *J. Histochem. Cytochem.* **50**, 449−454 (2002).
5. Ozawa, T., Yoshimura, H., Kim, S.B. *Anal. Chem.* **85**, 590−609 (2013).
6. Enterina, J. R., Wu, L., Campbell, R. E. *Curr. Opin. Chem. Biol.* **28**, 10−17 (2015).
7. van Ham, T. J., Mapes, J., Kokel, D. & Peterson, R. T. *FASEB J.* **24**, 4336−4342 (2010).
8. Yamaguchi, Y. *et al. J. Cell Biol.* **195**, 1047−1060 (2011).
9. Cabantous, S., Terwilliger, T. C. & Waldo, G. S. *Nat. Biotechnol.* **23**, 102−107 (2005).
10. Adrain, C., Creagh, E. M. & Martin, S. J. *EMBO J.* **20**, 6627−6636 (2001).
11. Link, V., Shevchenko, A. & Heisenberg, C. P. *BMC Dev. Biol.* **6**, 1 (2006).
12. Altschul, S. F., Gish, W., Miller, W., Myers, E. W. & Lipman, D. J. *J. Mol. Biol.* **215**, 403−410 (1990).
13. Gasteiger, E., Hoogland, C., Gattiker, A., Duvaud, S., Wilkins, M.R., Appel, R. D., Bairoch, A. *The Proteomics Protocols Handbook*; Walker, J. M., Ed.; Humana Press: Totowa, NJ, 571−607 (2005).
14. Seo, J. *et al. J. Cell. Biochem.* **110**, 1022−1037 (2010).
15. Westerfield, M. *The Zebrafish Book: A Guide for the Laboratory Use of Zebrafish (Danio rerio)*; Univ. of Oregon Press: Eugene, OR (1994).
16. Rembold, M., Lahiri, K., Foulkes, N. S. & Wittbrodt, J. *Nat. Protoc.* **1**, 1133−1139 (2006).
17. Czabotar, P. E., Lessene, G., Strasser, A. & Adams, J. M. *Nat. Rev. Mol. Cell Biol.* **15**, 49−63 (2014).
18. Hu, C.-D., Chinenov, Y. & Kerppola, T. K. *Mol. Cell* **9**, 789−798 (2002).
19. Eimon, P. M. & Ashkenazi, A. *Apoptosis* **15**, 331−349 (2010).
20. Chacinska, A., Koehler, C. M., Milenkovic, D., Lithgow, T. & Pfanner, N. *Cell* **138**, 628−644 (2009).
21. Collins, J. A., Schandl, C. A., Young, K. K., Vesely, J. & Willingham, M. C. *J. Histochem. Cytochem.* **45**, 923−934 (1997).
22. Scoltock, A. B. & Cidlowski, J. A. *Exp. Cell Res.* **297**, 212−223 (2004).

23. Ai, H. W., Hazelwood, K. L., Davidson, M. W. & Campbell, R. E. *Nat*. *Methods* **5**, 401−403 (2008).

24. Piston, D. W. & Kremers, G. J. *Trends Biochem*. *Sci*. **32**, 407−414 (2007).

25. Sakamoto, S., Terauchi, M., Hugo, A., Kim, T., Araki, Y., Wada, T. *Chem*. *Commun*. **49**, 10323−10325 (2013).

26. Rehm, M., Dussmann, H. & Prehn, J. H. *J*. *Cell Biol*. **162**, 1031−1043 (2003).

27. Karbowski, M. *et al. J*. *Cell Biol*. **159**, 931−938 (2002).

28. Hwang, W. Y. *et al. Nat*. *Biotech*. **31**, 227−229 (2013).

29. Galluzzi, L., Bravo-San Pedro, J. M. & Kroemer, G. *Nat*. *Cell Biol*. **16**, 728−736 (2014).

30. Lord, J. S., Rajotte, V. R., Korbutt, S. G., Bleackley, C. R. *Immunol. Rev*. **193**, 31−38 (2003).

Chapter 3

Development of a Method

for Characterizing Protein Clustering during Apoptosis

3-1. Introduction

Intrinsic mechanisms of cell death exist in multicellular organisms. One such mechanism, apoptosis, plays a crucial role in early development, homeostasis, and immunity in organisms[1]. Mitochondria often serve as a central organelle in the induction of apoptosis[2]. In response to external stimuli such as cytotoxic chemicals, starvation, and ultraviolet (UV) light, Bak and Bax proteins oligomerize to form clusters on the mitochondrial outer membrane. These clusters are responsible for the release of pro-apoptotic proteins such as cytochrome c and Smac from mitochondria into the cytosol. The release facilitates activation of caspases, leading to the degradation of proteins and DNA, and finally to cell death. Accordingly, the formation of Bak/Bax clusters on mitochondria is essential for the induction of apoptosis. Multiple studies have revealed the molecular mechanisms involved in the oligomerization of each Bak/Bax monomer[3–5]. However, how these clusters permeabilize the membrane to release the pro-apoptotic proteins remains elusive[2]. It is a subject of considerable debate in this question whether the cluster itself serves as a channel-like pore on the mitochondrial outer membrane (proteinaceous pore model) or the cluster disrupts the membrane to form a lipidic pore (lipidic pore model). Investigation of cluster characteristics in the cellular milieu is indispensable for addressing this question, but *in situ* characterization of the cluster has been impeded by the diffraction-limited resolution of light microscopy[6]. For alternative approaches such as electron microscopy, the labeling efficiency is insufficient to observe a significant fraction of Bak/Bax molecules in a cluster[7]. Such low labeling density hampers quantitative characterization of the cluster. Consequently, the challenge lies in devising a methodology that enables to characterize the Bak/Bax cluster *in situ* in a quantitative manner with sufficient spatial resolution.

Techniques of super-resolution fluorescence imaging enable the acquisition of images with resolution beyond the diffraction limit[8–10]. Of these methods, photoactivated localization microscopy (PALM) uses photoactivatable or photoswitchable probes to specifically visualize individual target molecules *in situ*. PALM provides information on localization of the molecule in a pointillistic fashion, allowing the quantitative analysis of closely spaced structures such as protein clusters. Because of these important features, various studies based on PALM have elucidated nanoscopic protein organizations such as bacterial receptor clustering[11], virus protein assembly[12,13], and RNA polymerase clustering[14,15].

I herein demonstrate a PALM-based approach for quantitative characterization of Bak clusters *in situ*. Using a functional, genetically encoded probe to specifically detect physiologically relevant Bak clusters in the absence of an endogenous background, I visualized clusters on mitochondria with nanoscale resolution and analyzed their sizes on a single-molecule level. Results suggest that the apoptotic pore responsible for releasing pro-apoptotic proteins is lipidic rather than proteinaceous.

3-2. Materials and Methods

3-2-1. Cell culture and induction of apoptosis

Wild-type MEF, *bak*$^{-/-}$ *bax*$^{-/-}$ MEF and Plat E cells were cultured in DMEM (high glucose) supplemented with 10% FBS, 100 unit/ml penicillin and 100 μg/ml streptomycin. They were incubated at 37°C in 5% CO_2 atmosphere. To induce apoptosis, MEFs were irradiated with UV light (254 nm) using a CL-1000 ultraviolet cross-linker (UVP).

3-2-2. Construction of plasmids

All genes were amplified by PCR using PrimeSTAR DNA polymerase and customized specific primers. The cDNA of Bak was amplified from mouse cDNA library. cDNA of mEos3 (I102N/H158E/Y189A mutant of mEos2) was generated by performing site-directed mutagenesis on cDNA of mEos2. mEos3-Bak was developed by linking cDNA of mEos3 and Bak with a flexible linker (GGGGS) and subcloned into a retroviral vector, pMX. mEos3-BakΔGD and mEos3-BakΔN were constructed by deleting the corresponding regions (six bases and 60 bases for mEos3-BakΔGD and mEos3-BakΔN, respectively), using KOD Plus Mutagenesis Kit (TOYOBO Co., Japan).

3-2-3. Viral infection and establishment of stable cell lines

For viral infection, the plasmids were respectively transfected into Plat E cells with TransIT-LT1 reagent (Mirus Co., TX). The supernatants of the media containing the viruses were obtained after 48 hours of the transfection and respectively added to *bak*$^{-/-}$ *bax*$^{-/-}$ MEF for stable expression. Infected *bak*$^{-/-}$ *bax*$^{-/-}$ MEF were cultured in 96-well plates in limiting dilutions to obtain the single clones. The clones, which showed the comparable morphology and expression level as compared with wild-type MEF, were selected and used for the experiments.

3-2-4. Live-cell imaging

bak$^{-/-}$ *bax*$^{-/-}$ MEF stably expressing GFP-Bak and Smac-SNAP, which was generated by viral infection, was treated with 3 μM SNAP-Cell TMR-STAR (New England BioLabs Inc.). The cells were washed with DMEM and then put on an observation medium (HEPES-buffered DMEM phenol red free, 10% FBS, pH 7.2). After UV irradiation as an apoptotic stimulation, fluorescence time-lapse images of the cells were acquired every 5 min using a laser scanning

confocal microscope (IX81-FV1000-D; Olympus Corp.) equipped with UPlanSApo 100×, 1.40 N.A. oil immersion objective. The cells on the stage was kept at 37°C using a stage incubator (Tokai Hit). The images were analyzed with ImageJ software by drawing regions around the cell and calculating the standard deviation (SD) of pixel intensities in the regions. Bak clustering index and Smac release index were calculated by dividing SD by the mean intensity of the fluorescence of GFP and TMR, respectively.

3-2-5. Western blot analysis

Cells were collected by scratching with scrapers, treated with lysis buffer (10 mM Tris-HCl pH 7.4, 150 mM NaCl, 5 mM EDTA, 50 mM NaF 0.5% NP-40) for 3 min and then centrifuged for 10 min at 16,000*g* at 4°C. The supernatants were boiled in sample buffer (250 mM Tris-HCl pH 6.8, 10% β-mercaptoethanol, 4% SDS, 10% sucrose) for 5 min. The proteins were subjected to SDS-PAGE using 10% polyacrylamide gels and subsequently transferred to a nitrocellulose membrane. After blocking with 1% skim milk in TBST buffer (50 mM Tris-HCl pH 8.0, 150 mM NaCl, 0.05% Tween-20), the membrane was blotted with a polyclonal anti-Bak antibody (Bak NT; Millipore) at dilution 1/500 overnight at 4°C. The membrane was then washed three time with TBST and incubated with anti-rabbit IgG conjugated with horseradish peroxidase (HRP) (Jackson Immuno Research Laboratories, Inc., West Grove, PA) at dilution 1/5000 for 1 h at room temperature. After washing the membrane three times with TBST, the proteins were detected using SuperSignal West Femto Maximum Sensitivity Substrate (Thermo Scientific, Loughborough, UK) and LAS 4000 mini CCD camera (GE Healthcare, Little Chalfont, Buckinghamshire, UK). After detection, the membrane was probed by anti-β-actin antibody (Sigma) followed by an HRP-conjugated anti-mouse IgG antibody (Jackson Immuno Research Laboratories, Inc., West Grove, PA). The detection of β-actin was then performed using SuperSignal West Femto Maximum Sensitivity Substrate and LAS 4000 mini CCD camera.

3-2-6. Quantification of apoptosis

Cells were seeded in 35 mm dishes at a cellular density of 1.0×10^5 cells/ml. After 24 hours, cells were stimulated with UV light. Cells and medium were collected after 24 hours of UV stimulation and then centrifuged for 2 min at 600*g* at room temperature. After supernatant was removed, 200 μl of DMEM was added to the pellet. The pellet was suspended by gentle pipetting and 200 μl of 0.4% Trypan Blue Solution (Wako) was added. After incubation for 1 min, the samples were subjected to an automatic cell counter (Countess, Invitrogen) to measure the percentages of cell death.

3-2-7. Immunostaining

After UV irradiation as apoptotic stimulation and treatment with Mitotracker Red CMXRos (Invitrogen) to stain mitochondria, cells on a cover glass were fixed with 4% paraformaldehyde (Alfa Aesar, USA) in phenol red free DMEM at 37°C for 10 min. The cells were washed with PBS and permeabilized with 0.2% Triton X-100 in PBS for 5 min at room temperature. The cells were then washed with PBS and blocked by 0.2% fish skin gelatin (FSG) in PBS for 1 h at room temperature. The buffer was exchanged to 0.2% FSG in PBS containing 1/500 dilution of rabbit anti-Bak polyclonal antibody (Bak NT) and incubated overnight at 4°C, shaking gently. After washing with PBS, the cells were incubated with 0.2% FSG in PBS containing 1/2000 dilution of a donkey anti-rabbit antibody conjugated with Alexa647 (Molecular Probes, Inc.) for 1 h at room temperature. The cells were washed with 0.2% FSG in PBS and mounted on a slide glass with FluorSave Reagent (Calbiochem). Fluorescence image of the samples were acquired using a laser scanning confocal microscope.

3-2-8. PALM imaging

After UV irradiation as apoptotic stimulation and treatment with Mitotracker Deep Red FM (Invitrogen) to stain mitochondria, cells on a cover glass were fixed with 4% paraformaldehyde in phenol red free DMEM at 37°C for 10 min. The cells were washed with PBS and imaged using a home-built TIRF microscope constructed on an inverted microscope (IX81; Olympus Corp.) equipped with PlanApo 100×, 1.49 N.A. oil immersion objective (Olympus). Four laser lines with 405 nm (JUNO 405; SOC), 488 nm (CYAN-488; Spectra-Physics), 561 nm (JUNO 561; SOC) and 640 nm (CUBE 640-100C; Coherent) were combined in an external platform. Samples were illuminated in highly inclined and laminated optical sheet (HILO) configuration[16]. Fluorescence emission was detected with an EM-CCD camera (ImagEM; Hamamatsu Photonics) with an image pixel size of 160 nm. Approximately 22,000 frames were acquired with an exposure time of 30 ms per frame. Number of frames acquired was dependent on the regions of highest mEos3 density. mEos3 was activated with 405 nm laser intensity which was intermittently increased during a PALM experiment from 1 mW/cm^2 to 1 W/cm^2 so that the PALM acquisition maintained a low density of photoactivated fluorophores in each frame. Simultaneously, mEos3 was excited with 561 nm laser intensity of ~1 kW/cm^2. Fluorescent signal from mEos3 was directed to the EM-CCD camera using a polychromatic dichroic mirror (Di01-R405/488/561/635, Semrock) and a band pass filter (FF01-609/54, Semrock). The detected signals were localized with PeakSelector software (IDL, courtesy of Harald Hess), using a threshold of 100 photons which was obtained by observing a non-transfected fixed *bak*$^{-/-}$ *bax*$^{-/-}$ MEF. Each fluorescent peak was fitted to a two-dimensional Gaussian distribution by nonlinear least-square fitting to obtain *x* and *y* coordinates.

In PALM, it is highly possible that a single fluorophore emits photons over multiple consecutive frames before being bleached, leading to an overcounting error. Therefore, it is a prerequisite to correct the error by grouping the fluorescent signals localized within the specific spatial threshold into the single molecule. In this grouping analysis, fluorescent molecules localized within 64 nm in consecutive frames were counted as the same molecule. The spatial threshold (64 nm), which corresponds to three times the measured mean localization precision, provides the best assignment[17]. In addition to the grouping analysis using the spatial threshold, a correction of another overcounting error due to blinking of fluorophore is required for an estimation of the number of molecules. To address this issue, I plotted the number of localizations as a function of a temporal threshold in grouping analysis by observing *bak*$^{-/-}$ *bax*$^{-/-}$ MEF transiently expressing mEos3-Bak. The plot within the first 1.5 s was fitted by a distribution given by $P(t) = A(1+n_{blink}\, e^{-t/toff})$, where n_{blink} is the mean number of blinking events per molecule and t_{off} is the time the molecule spends in the dark state[18]. The number of Bak molecule per cluster was obtained by dividing the number of localizations in each cluster by a factor of 1.42 which corresponds to $1 + n_{blink}$. A decimal place of each obtained number was omitted. Grouping analysis using a fixed temporal threshold yields a significantly large error while the normalization by $1 + n_{blink}$ provides a good estimation of number of molecules[19]. PALM images were generated by superimposing the position coordinates of the detected molecules with a width corresponding to their localization precision by using Octane plug-in for ImageJ software[20].

To quantify the degree of Bak clustering relative to homogeneous distribution, the spatial point pattern of Bak distribution obtained by PALM was used to calculate Ripley's K-function with SpPack[21,22]. Ripley's K-function is given by,

$$K(r) = A\sum_{i=1}^{n}\sum_{j=1}^{n}\left(\frac{\delta_{ij}}{n^2}\right) \quad \text{where } \delta_{ij} = 1 \text{ if } \delta_{ij} < r, \text{ otherwise } 0 \tag{1}$$

where A is the area of the analyzed region, n is the number of points, r is the analyzed spatial scale and δ_{ij} is the distance between two points i and j. $K(r)$ represents the normalized number of points encircled by concentric circle with radius r centered on each point. This function, which scales with circle area, was then transformed into the L-function such that the scaling is linear with radius r:

$$L(r) = \sqrt{\frac{K(r)}{\pi}} \tag{2}$$

$L(r)$ equals to r at all r for completely random distribution of points. I hence plotted $L(r) - r$ as a function of r such that a random distribution results in $L(r) - r = 0$ for all r. $L(r) - r$ has positive values for a given r at which the distribution is more clustered than a random distribution. Points at the edge of the analyzed region were weighted to negate edge-related effects[22]. I calculated

99% confidence intervals by simulating 500 spatially random distributions with the same mean molecular density as the data region.

3-2-9. Cluster analysis

To objectively identify Bak clusters, I performed cluster analysis using an existing algorithm, DBSCAN (short for *density-based spatial clustering of application with noise*). DBSCAN is a powerful algorithm for data mining and spatial pattern analysis[23,24]. Identification of Bak clusters with DBSCAN is based on the density distribution of Bak molecules in a dataset obtained in a PALM experiment. Bak localizations with greater than *MinPts* neighbors within a radius ε are connected to their neighbors. These connected localizations are considered to be clustered. Bak localizations which are not connected to any other localizations are considered to be non-clustered noise.

There are two parameters to be decided in DBSCAN: ε and *MinPts*. Because the mean molecular densities in healthy cells were comparable in mEos3-Bak and mEos3-BakΔN, it was possible to meaningfully use the same values of the parameters for these datasets. I chose ε of 20 nm which corresponds to the mean localization precision. *MinPts* should be large enough to separate from noise, but it should not be too large as to overlook a part of clusters. I determined *MinPts* based on datasets in healthy cells which were not considered to contain any physiological Bak clusters and found that *MinPts* = 13 provided the best result in this regard. Finally, I defined the localizations identified with DBSCAN as a cluster containing a minimum number of 18 Bak molecules which was previously shown with a biochemical study[3].

3-2-10. Cluster characterization

After identifying Bak clusters with DBSCAN, I examined a set of different parameters to characterize Bak clusters. Radius of each cluster, R_g, was calculated as the radius of gyration of all localizations within the cluster:

$$R_g = \sqrt{\frac{1}{N}\sum_{i=1}^{N}(\mathbf{r_i} - \mathbf{r_c})^2} = \sqrt{\frac{1}{N}\sum_{i=1}^{N}\left\{(x_i - x_c)^2 + (y_i - y_c)^2\right\}} \quad (3)$$

where N is the number of localizations belonging to each cluster, $\mathbf{r_i}$ (x_i, y_i) is the coordinate of each localization within a cluster, and $\mathbf{r_c}$ (x_c, y_c) is the coordinate of the center of mass. The measurement of R_g is based on two dimensional (2D) projection of three dimensional (3D) cluster. Relationship between R_g and radius of 3D cluster, R, is given by,

$$R = \sqrt{\frac{1}{N}\sum_{i=1}^{N}\left\{(x_i - x_c)^2 + (y_i - y_c)^2 + (z_i - z_c)^2\right\}} = R_g\sqrt{1 + \frac{\sum_{i=1}^{N}(z_i - z_c)^2}{\sum_{i=1}^{N}(x_i - x_c)^2 + \sum_{i=1}^{N}(y_i - y_c)^2}} \quad (4)$$

where z_i and z_c represent the coordinate along z axis of each localization and the center of mass, respectively. Equation (4) indicates the degree of underestimation in the measurement of cluster radius due to the 2D projection. Assuming that the variances of cluster size along x, y and z axes are comparable, I underestimate the radius approximately by 20%.

The fractal dimension, D_f, was defined as:

$$N = k\left(\frac{R_g}{a}\right)^{D_f} = \left(\frac{k}{a^{D_f}}\right)R_g^{D_f} \quad (5)$$

where N is the number of localizations belonging to each cluster, a is the radius of a Bak molecule and k is the structural coefficient[25]. The scattered plot of N with R_g in logarithmic fashion was fitted by a linear model to obtain the slope, which corresponds to D_f.

Local molecular densities were measured by counting the number of localizations within a square with a side of 20 nm.

3-2-11. Correlative microscopy

Cells expressing mEos3-Bak were grown on a gridded glass-bottom dish for 24 hours before fixation. After UV irradiation as apoptotic stimulation, cells were fixed with a conventional buffer (1.5% paraformaldehyde and 3% glutaraldehyde in 0.1 M phosphate buffer, pH7.3) for 15 min at room temperature. The cells were washed with distilled water and set under a TIRF microscope for PALM imaging in which the acquisition procedure was virtually identical to the protocol described above. The grid number, where a cell formed Bak clusters, was registered in PALM imaging for the identification of cells in the subsequent electron microscopy. After PALM imaging, electron microscopy was performed as described previously[26]. Briefly, the cells observed in PALM were fixed by an aqueous solution of 1% OsO_4 for 30 min on ice. The sample was embedded in Epon 812 and thin sections (70−80 nm) were then cut. Each section was stained with uranyl acetate and lead citrate for observation under a Jeol-1010 electron microscope (Jeol) at 80 kV.

3-2-12. Fluorescence recovery after photobleaching (FRAP) analysis

Cells expressing mEos3-Bak or mEos3-BakΔN were grown on a glass-bottom dish for 24 hours before FRAP experiments and put on an observation medium (HEPES-buffered DMEM phenol

red free, 10% FBS, pH 7.2). Fluorescence time-lapse images of the cells were acquired at 250 ms/frame using a laser scanning confocal microscope equipped with UPlanSApo 100×, 1.40 N.A. oil immersion objective. The pinhole size was 500 μm. During the measurement, the cells on the stage was kept at 37°C using a stage incubator. After several frames were acquired, the fluorescence in a circular area of 0.3 μm^2 was bleached with 488 nm at 100% laser power for 200 ms. Fluorescence recovery in the bleached region were recorded for the following 20 seconds. The fluorescence recovery curve, $R(t)$, was created using IGOR Pro software (WaveMetrics) according to following calculations. First, a background signal was subtracted from a whole image using an empty region of the image. Second, the fluorescence intensity in not bleached area on mitochondria as a function of time was calculated ($I_a(t)$). Third, the fluorescence intensity in the bleached area as a function of time was calculated ($I_b(t)$). Finally, $R(t)$ was obtained as $I_b(t)/ I_a(t)$ with the normalization of the intensity before bleaching. The $R(t)$ curves from several different cells were then averaged together to produce the FRAP curves. The FRAP curves were fitted by Jacobson's equation ($R(t) = I_{final} \exp(-2\tau_D/(\tau_D+2t))$) to obtain the diffusion coefficient, D, where I_{final} represents the rate of recovery at $t = \infty$ and τ_D is the diffusion time[27]. D was calculated by using the equation $D = \omega^2/4\tau_{1/2}$, where ω is the $1/e^2$ radius of the Gaussian profile of the fluorescence intensity in the bleached area and $\tau_{1/2}$ indicates the time for the half recovery. ω was measured in a FRAP experiment in a fixed cell, resulting in $\omega = 1.38$ μm. $\tau_{1/2}$ corresponds to $1.27\tau_D$.

3-3. Results

3-3-1. Establishment of a cell line expressing a fluorescently-labeled Bak

To observe Bak clusters *in situ* using PALM, I developed a Bak cluster probe, named mEos3-Bak, in which Bak was labeled with a photoactivatable fluorescent protein, mEos3. mEos3 shows a monomeric property even at high concentration[28]. This property is critically important in order to abrogate the formation of artifactual clusters of a target protein and to observe physiologically functional clusters. Because the C-terminal region (185−200 residue) of Bak is inserted into mitochondrial outer membrane, mEos3 was fused with the N-terminus of Bak to avoid perturbing mitochondrial localization of the probe (**Figure 3-1A**).

The replacement of endogenous Bak by mEos3-Bak is a prerequisite to fully addressing the characterization of Bak clusters. To fulfill this need, *bak*$^{-/-}$ *bax*$^{-/-}$ mouse embryonic fibroblast (MEF), in which endogenous *Bak* and *Bax* genes were knocked out, was stably transfected with *mEos3-Bak*. *Bax* is a close homolog of *Bak* and shares the similar apoptotic function[29]. Subsequently, nine single clones were selected by the limiting dilution and their probe expressions were investigated by western blotting (**Figure 3-1B**). Among the clones, clone 2 showed the expression level of mEos3-Bak similar to endogenous Bak in wild-type MEF. Consequently, the clone 2 was used in the following experiments. The subcellular localization of mEos3-Bak in the cell line was merged with the localization of mitochondria in the absence of apoptotic stimulation, ensuring that the labeling with mEos3 did not interfere with the mitochondrial localization of Bak (**Figure 3-1C**, upper panel). In contrast, mEos3-Bak upon UV irradiation showed a punctate localization on mitochondria, indicative of the formation of Bak clusters (**Figure 3-1C**, lower panel). In conclusion, I established the cell line expressing mEos3-Bak for characterizing Bak clusters.

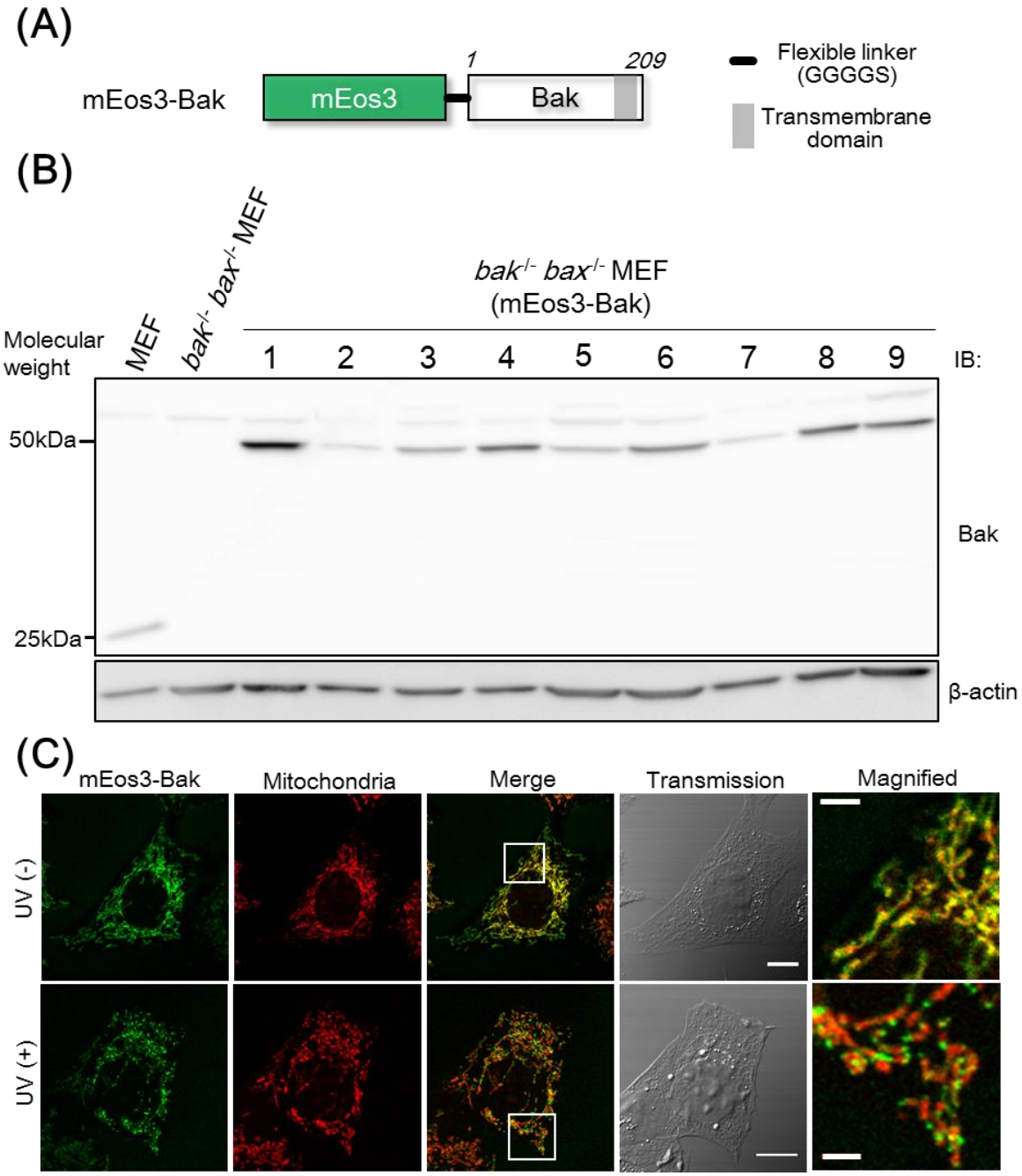

Figure 3-1. Establishment of a cell line expressing a fluorescently-labeled Bak.

(**A**) Schematic construct of mEos3-Bak. mEos3 is fused to Bak at the N-terminus with a flexible linker composed of 5 amino acids (Gly, Gly, Gly, Gly and Ser). Numbers in italics show the residue of amino acids in Bak. Transmembrane region for mitochondrial localization is indicated as gray box (185−200). (**B**) Western blot analysis for investigating the expression of mEos3-Bak in nine cell lines. (**C**) Confocal imaging of the cells in the presence or absence of UV irradiation as apoptotic stimulation. Mitochondria were visualized by MitoTracker CMXRos dye. Magnified images in white boxes (Merge) are shown (right panels). Scale bars: 10 μm (transmission), 2 μm (magnified).

3-3-2. Characterization of the cell line

Next, I tested the functionality of the fluorescent protein by investigating whether mEos3 in the probe was photoconverted from green to red form upon violet light illumination by confocal microscopy. The imaging analysis showed that UV light (254 nm) used as apoptotic stimulation in this study did not produce a red fluorescence whereas violet light (405 nm) converted mEos3 from green to red (**Figure 3-2A**). These results suggest that the probe is applicable to PALM for characterizing Bak clusters during UV-induced apoptosis.

Trypan blue exclusion assay revealed that the engineered cell line showed the susceptibility to UV stimulation at the comparable level to wild-type MEF (**Figure 3-2B**). By contrast, apoptosis was not induced in *bak*$^{-/-}$ *bax*$^{-/-}$ MEF upon UV stimulation. The assay demonstrated that mEos3-labeled Bak constructed as the Bak cluster probe in the cell retained the function to induce apoptosis at a similar level to endogenous Bak expressed in wild-type MEF.

Finally, I investigated whether the Bak connected with mEos3 in the clusters undergoes a structural change to an active form responsible for the induction of apoptosis. Upon exposure to an apoptotic stimulus, cryptic N-terminal residues of Bak are exposed, followed by the formation of a Bak cluster (**Figure 3-3A**)[2]. This structural transition is able to be analyzed by immunostaining with an antibody specific for N-terminus Bak (**Figure 3-3B**). In the immunostaining analysis for the engineered cell line, the fluorescence signal of an active Bak was clearly detected in UV-stimulated cells whereas no active Bak existed in the unstimulated cells (**Figure 3-3C**). Localization of the active Bak was the same as that of mEos3-Bak, indicating that mEos3-Bak in the cluster was an active form. These results, taken together, demonstrated that mEos3-Bak enabled to visualize the physiologically relevant clusters *in situ*.

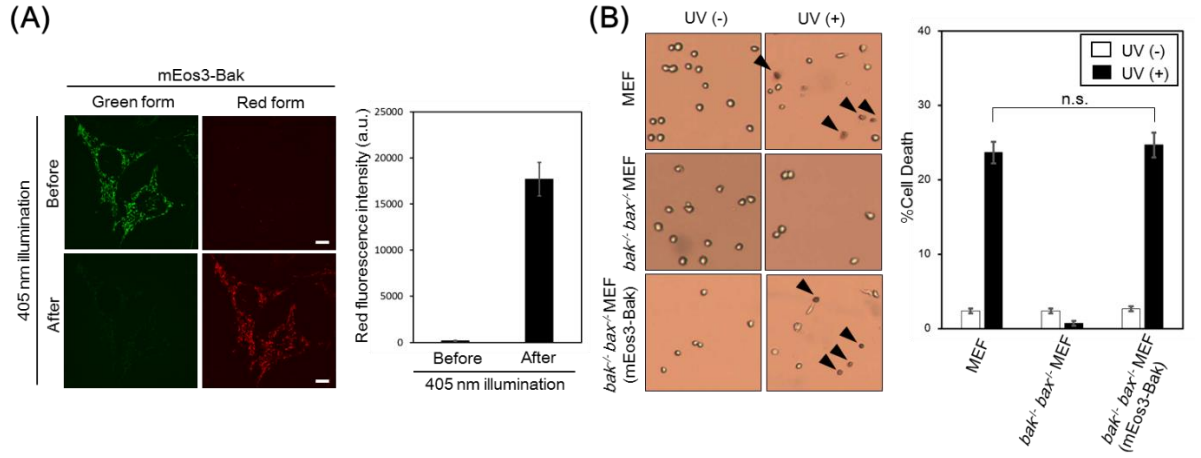

Figure 3-2. Characterization of the cell line.

(**A**) Violet-light-dependent photo-conversion of mEos3-Bak. UV (254 nm) light was irradiated and subsequently fluorescence intensity in red form of mEos3 before and after violet light illumination was measured in three different regions in the cells (right). Scale bars: 10 μm. Data are represented as mean ± s.e.m. (n = 3). (**B**) Trypan blue exclusion assay for examining cell viability upon UV stimulation. Arrowheads indicate dead cells. Statistical analysis was performed with two-tailed unpaired Student's *t*-test. In the analysis, $P > 0.05$ is indicated as not significant (n.s.). Data are represented as mean ± s.e.m. (n = 3).

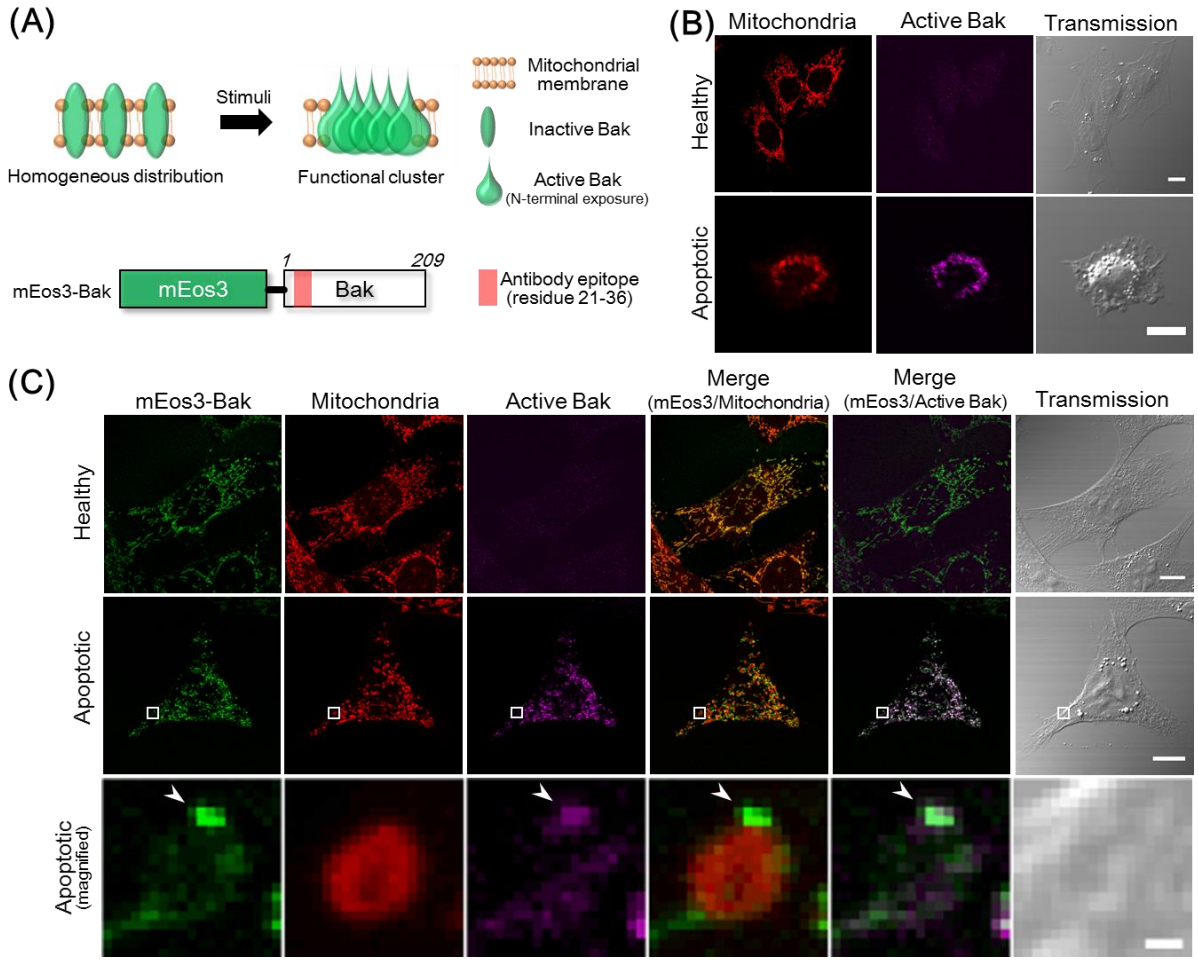

Figure 3-3. Validation of the intramolecular conformational change in the probe.

(**A**) The formation of a functional Bak cluster via an intramolecular conformational change. A red box in the schematic structure of mEos3-Bak indicates the epitope recognized by a Bak antibody used in this immunostaining. The epitope in N-terminal region is cryptic in inactive Bak, but exposed upon apoptotic signals to be active Bak. (**B**) Immunostaining of active Bak in the wild-type MEF expressing endogenous Bak. Scale bars: 10 μm. (**C**) Immunostaining of active Bak in the engineered cell line expressing mEos3-Bak. Magnified images in white boxes (middle) are shown at bottom. Arrowheads indicate a functional Bak cluster. Scale bars: 10 μm (top and middle), 0.5 μm (bottom).

3-3-3. Super-resolution imaging of Bak clusters

To observe Bak clusters responsible for the induction of apoptosis, I identified the stage at which pro-apoptotic proteins were released from mitochondria into cytosol (**Figure 3-4**). In this stage, a cell morphology remains intact but Bak clusters are formed on mitochondria. The established cell line which stably expressed mEos3-Bak was irradiated with UV and subsequently fixed with paraformaldehyde at this stage. Bak clusters were observed by PALM with the mean localization precision of 19.6 nm (**Figure 3-5** and **Figure 3-6A**). A full-width half maximum (FWHM) of the line intensity profile on the mEos3-Bak cluster was 330 nm in the wide-field image, whereas that in the PALM image was 79 nm (**Figure 3-6B**). PALM imaging in combination with electron microscopy revealed that the ultrastructure of mitochondrial membrane was altered in the cells upon formation of Bak clusters (**Figure 3-7**), suggesting that the clustering of Bak proteins was correlated with the perturbation of the integrity of mitochondrial membrane[30].

PALM provided information on the localization of individual mEos3-labeled Bak molecules, by which a super-resolution image was reconstructed (**Figure 3-6A**). In the distribution of mEos3-Bak molecules in apoptotic cells, I found that some Bak molecules contributed to the formation of clusters whereas other Bak molecules were not spatially clustered. This biased distribution of Bak molecules suggests that the cell undergoes apoptosis before the formation of the cluster by all Bak molecules on each mitochondrion. To quantitatively analyze the spatial distribution of Bak molecules, I implemented Ripley's K analysis for measuring the degree of the clustering. As shown in **Figure 3-6C**, the distribution of Bak in a healthy cell was random, whereas Bak in an apoptotic cell showed heterogeneous localization on mitochondria. Ripley's K analysis also suggested that Bak molecules formed a cluster by significantly changing the distribution during apoptosis.

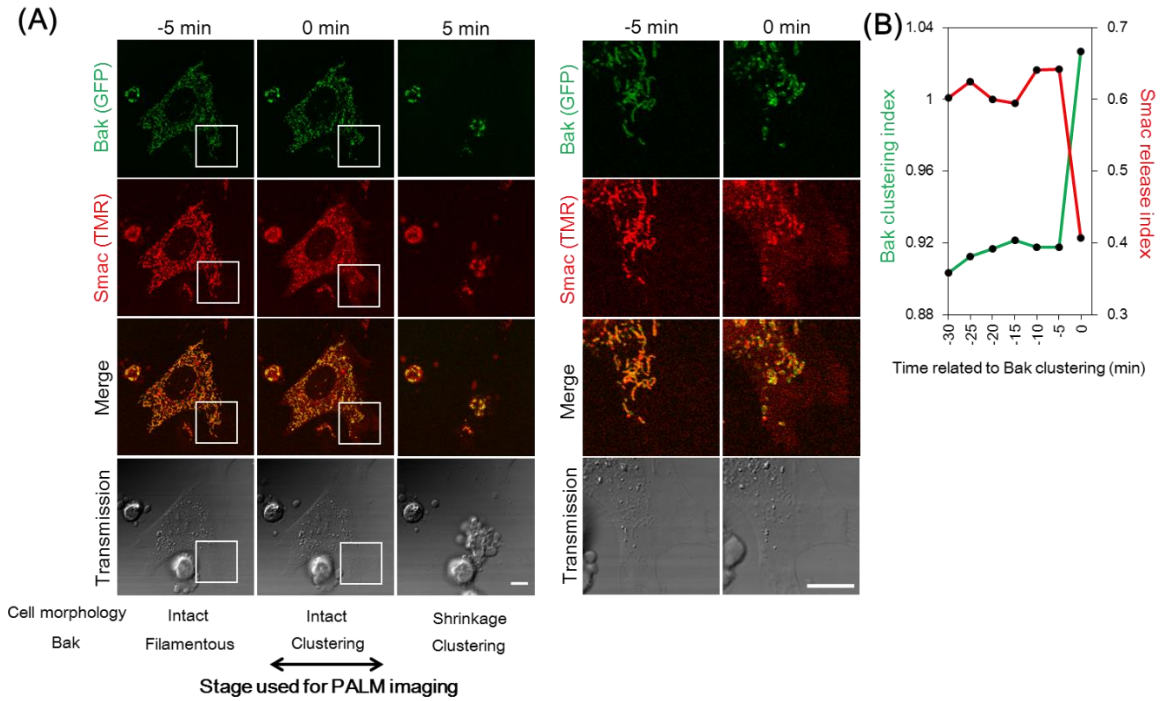

Figure 3-4. Time-lapse imaging of the formation of Bak clusters and the release of Smac during apoptosis.

(**A**) Dynamics of Bak and pro-apoptotic protein Smac in a UV-stimulated *bak*$^{-/-}$ *bax*$^{-/-}$ MEF stably expressing GFP-Bak and Smac-SNAP. Magnified images in the white boxes are shown (right). Punctate localization of GFP-Bak and cytosolic localization of Smac-SNAP at time 0 indicate the formation of Bak clusters and the release of Smac from mitochondria, respectively. The stage, at which a cell morphology remained intact but Bak clusters were formed, was used for PALM imaging. Scale bars: 5 μm. (**B**) Quantitative analysis of the dynamics of Bak and Smac observed in (**A**).

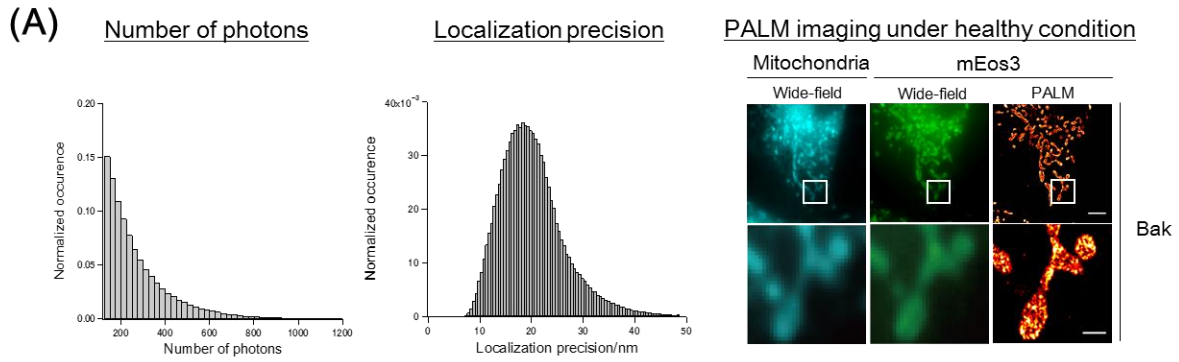

(B)

Construct	Number of photons	Localization precision (nm)	Density (molecules/μm^2)
mEos3-Bak	256	19.6 ± 6.2	(1.55 ± 0.23) × 10^3

Figure 3-5. The localization precision and the molecular density.

(**A**) Distribution of total photon numbers per burst and the localized precision in the engineered cell line expressing mEos3-Bak. For the analyses, fluorescence emission with less than 100 photons was discarded as background noise and hence not shown in the distribution. PALM images of each cell line under a healthy condition used for the analyses are shown (right). Boxed regions are magnified in the lower panels. Scale bars: 5 μm (top), 1 μm (bottom). The localization precision for each molecule was experimentally calculated as described previously[31]. (**B**) Summary of the localization precision and the molecular density of mEos3-Bak. Data are represented as mean ± s.d.

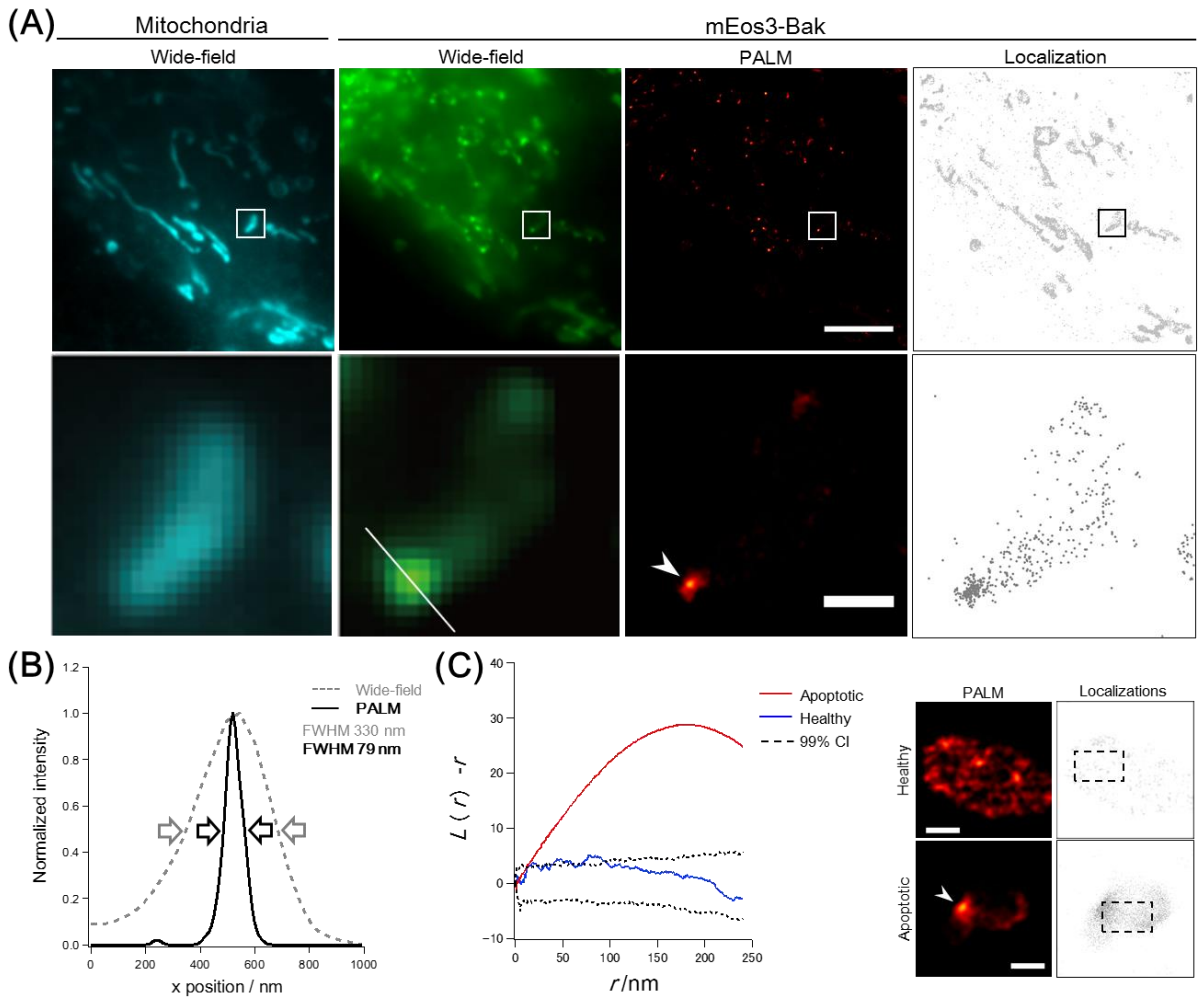

Figure 3-6. Super-resolution imaging of Bak clusters.

(**A**) The images of mitochondria (Wide-field) and mEos3-Bak (Wide-field, PALM and Localization). Mitochondria were visualized by MitoTracker Deep Red dye. Magnified images in the boxed regions are shown in lower panels. An arrowhead indicates a Bak cluster. Scale bars: 3 μm (top), 500 nm (bottom). (**B**) A line-intensity profile of a white line in (**A**). The cluster size was estimated by calculating full width half maximum (FWHM) of the profile. (**C**) Ripley's K analysis for measuring the degree of the spatial distribution of Bak molecules. $L(r)$-r was plotted as a function of a radial scale, r. The analyses were performed in the boxed regions (480 nm × 800 nm) of a heathy cell and an apoptotic cell. An arrowhead indicates a Bak cluster. CI, confidence intervals. Scale bars: 500 nm.

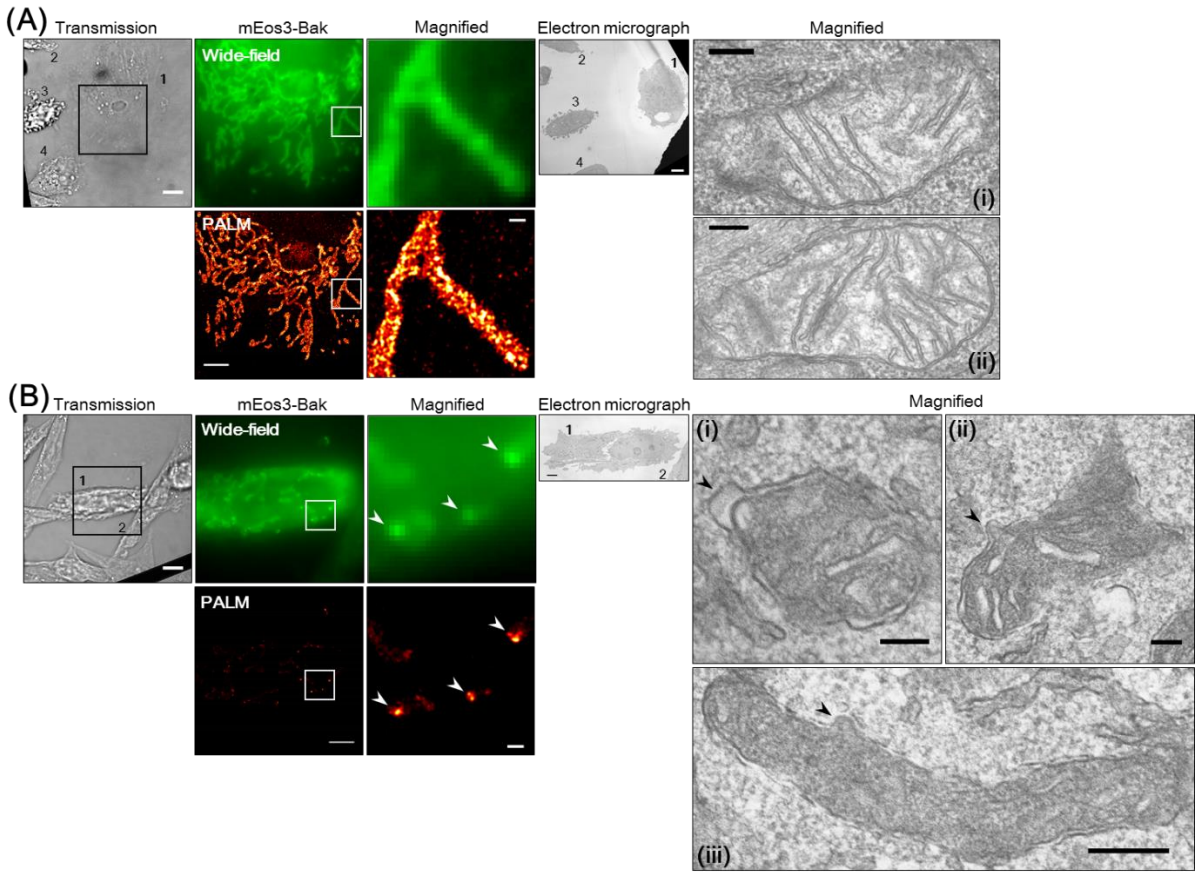

Figure 3-7. Correlative microscopy.

(**A**) PALM and electron microscopy (EM) micrograph in the cell line expressing mEos3-Bak under unstimulated conditions. The region in a black square, which belonged to cell 1, was imaged by PALM. The regions in white squares were magnified, showing a filamentous localization of mEos3-Bak. A low magnification electron micrograph represented the same field shown in the optical transmission image. The cell 1 imaged by EM with higher magnification showed a clear cristae structure (i and ii). Scale bars: 10 μm (Transmission), 3 μm (PALM), 500 nm (PALM, magnified), 5 μm (EM, low magnification), 200 nm (EM, high magnification). (**B**) PALM and EM micrograph in an apoptotic cell. Cells stimulated with UV were imaged by PALM and subsequently EM images were acquired in the same cell (cell 1). White and black arrowheads indicate the formation of Bak clusters in PALM and the distorted membrane structures in EM (i, ii and iii), respectively. Scale bars: 10 μm (Transmission), 3 μm (PALM), 500 nm (PALM, magnified), 3 μm (EM, low magnification), 200 nm (EM, high magnification), 20 nm (EM, inset).

3-3-4. Characterization of Bak clusters

I further quantitatively analyze the Bak clusters using the list of Bak localization coordinates, and not the rendered PALM image[32]. To investigate which Bak molecules constitute a cluster, I implemented a cluster analysis using an existing algorithm, DBSCAN (short for *density-based spatial clustering of application with noise*), based on the local density of proteins[24]. The clusters were identified on mitochondria (**Figure 3-8**), consistent with punctate fluorescence in PALM image.

Next, I analyzed the cluster radius and the number of Bak molecules per cluster (**Figure 3-9**). The analysis revealed that the radius (R_g) broadly distributed from 35 nm to 330 nm, resulting in the mean radius of 111 ± 50 nm (s.d.) (**Figure 3-9B**). Notably, 84% of the clusters analyzed were smaller than the diffraction limit. To rigorously quantify the number of Bak molecules, I obtained a series of imaging data until no fluorescence signal was detected (**Figure 3-10A**). Furthermore, I plotted the cumulative number of Bak molecules in each cluster, confirming that the imaging of the detectable mEos3 in each cluster was completed (**Figure 3-10B**). The mean number of blinking events per mEos3 molecule (n_{blink}), which leads to overcounting error, was 0.42 (**Figure 3-11**). Correcting the error due to blinking, I found that the number of Bak molecules per cluster (N) exhibited a wide distribution between 23 to 2,505 molecules (**Figure 3-9C**). In the distribution fitted by a single exponential decay, 63% of the detected Bak clusters contained less than τ of 330 molecules. I also observed a wide distribution of R_g and N in each cell (**Figure 3-12**), confirming that the Bak clusters in the cells were imaged at the same stage during apoptosis. To investigate a scaling relationship between R_g and N, I used a fractal analysis (**Figure 3-9D**)[25,33]. In this analysis, the scaling relationship is characterized by the fractal dimension (D_f) which corresponds to the slope of linear regression in radius-molecular number plot. The analysis on R_g and N in each Bak cluster yielded D_f of 1.80 ± 0.09 (95% confidence interval). The value D_f is close to 2, indicating that the cluster area increases linearly with number of molecules. Accordingly, the result suggests that a density of Bak molecules within clusters is homogeneous among clusters with different sizes.

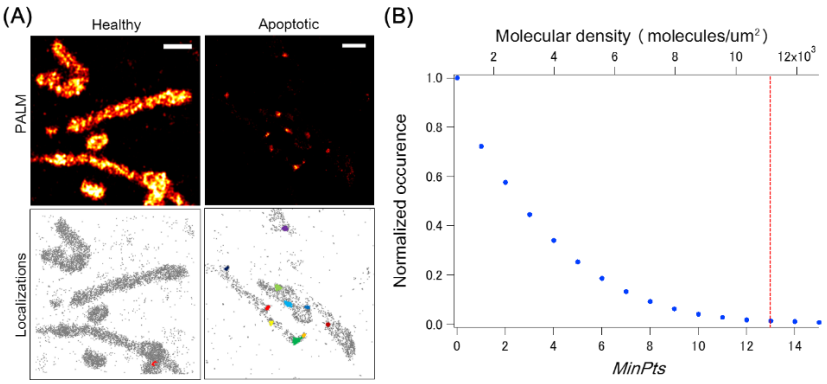

Figure 3-8. A cluster analysis to identify Bak clusters using DBSCAN.

(**A**) PALM images and mEos3-Bak localizations plotted as gray points in the cell lines expressing mEos3-Bak. Localizations defined as a cluster by DBSCAN share the same randomly chosen color. Many clusters were identified by DBSCAN in a good agreement with PALM image in apoptotic cells. Scale bars: 1 μm. (**B**) Normalized number of localizations identified as clusters in healthy cells, which do not form any functional Bak clusters, is shown as a function of *MinPts*. The molecular density was calculated as $(MinPts+1)/\pi\varepsilon^2$, where ε is a radius of a circle used in DBSCAN and equals to 20 nm. In case of *MinPts* = 13 (red line), 98.6% of localizations were removed as non-clustered noise.

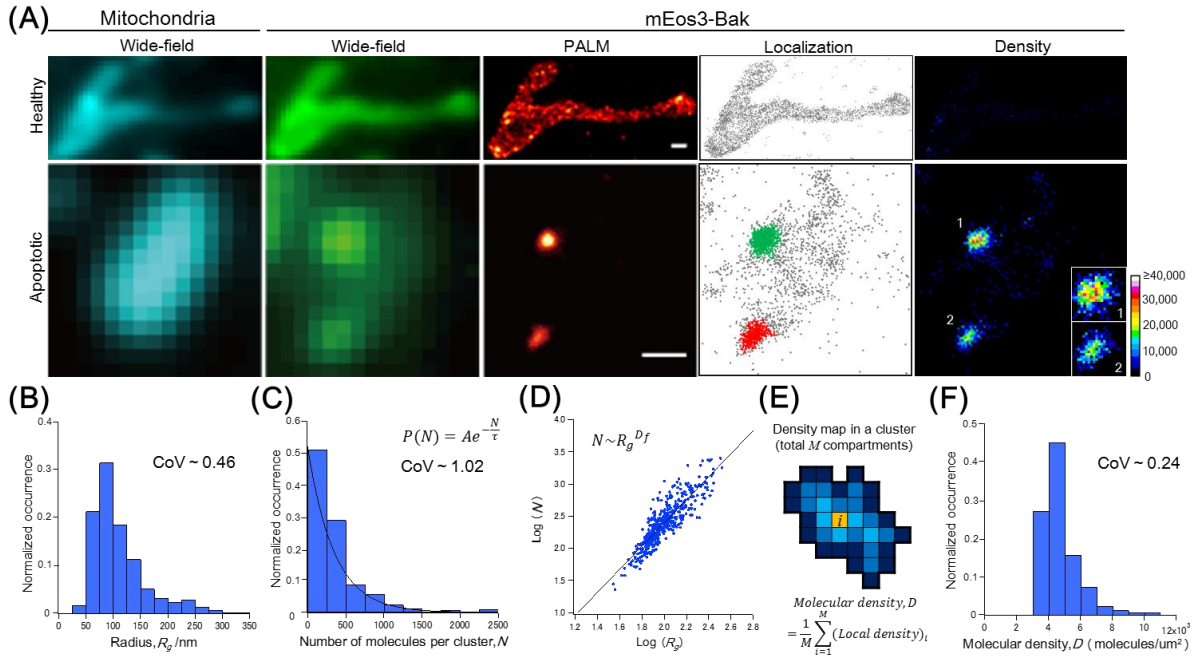

Figure 3-9. Characterization of the Bak cluster.

(**A**) The images of mitochondria (Wide-field) and mEos3-Bak (Wide-field, PALM, Localization and Density) in a healthy cell and an apoptotic cell expressing mEos3-Bak. Localizations identified as a cluster are colored (mEos3, Localization). The color bar indicates the molecular density (molecules/μm^2) in the density maps. Magnified images of the clusters were shown in the inset. Scale bars: 500 nm. (**B**) Normalized histogram of the radii (R_g) of mEos3-Bak clusters. (**C**) Normalized histogram of the number of mEos3-Bak molecules per cluster (N). The distribution was fitted by single exponential decay. (**D**) Fractal analysis. In each cluster, N was plotted as a function of R_g in logarithmic scales. Linear regression of the plot yields the slope which corresponds to the fractal dimension (D_f). (**E**) Schematic illustration of computation of the molecular density (D) in each cluster. Each local density in an area with 20 nm × 20 nm is colored according to the color bar in (A). (**F**) Normalized histogram of D. CoV indicates the coefficient of variation obtained for the respective data. N = 433 clusters from four cells.

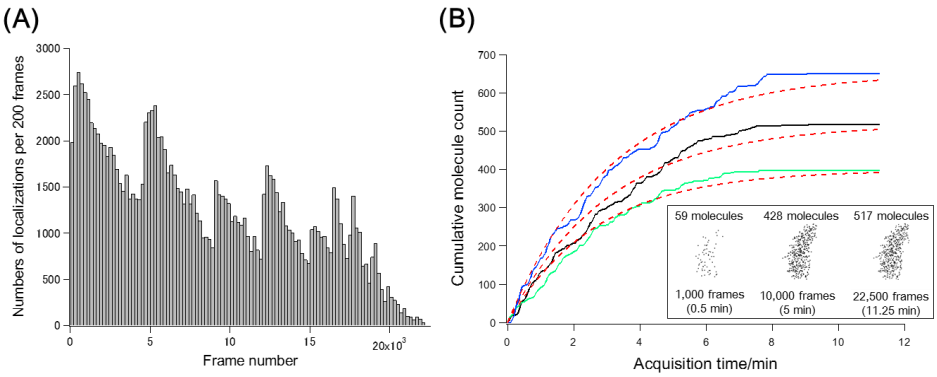

Figure 3-10. Complete PALM imaging and molecular counting in a cluster.

(**A**) Number of localizations per 200 frames were plotted as a function of frame number in a representative PALM imaging of mEos3-Bak. Occasional increases in the intensity of violet light used for photoactivation resulted in an increase in the localizations detected. At the end of the experiment (frame number 22,500), no more fluorescent signals of mEos3-Bak were detected, indicating a stoichiometric read-out. (**B**) Cumulative molecular count for three representative mEos3-Bak clusters as a function of acquisition time. The plots, which finally reached a plateau, were fitted to an exponential function (dashed red lines)[12]. The images after 0.5 min, 5 min and 11.25 min of the cluster plotted as a black line in the graph were shown in the inset.

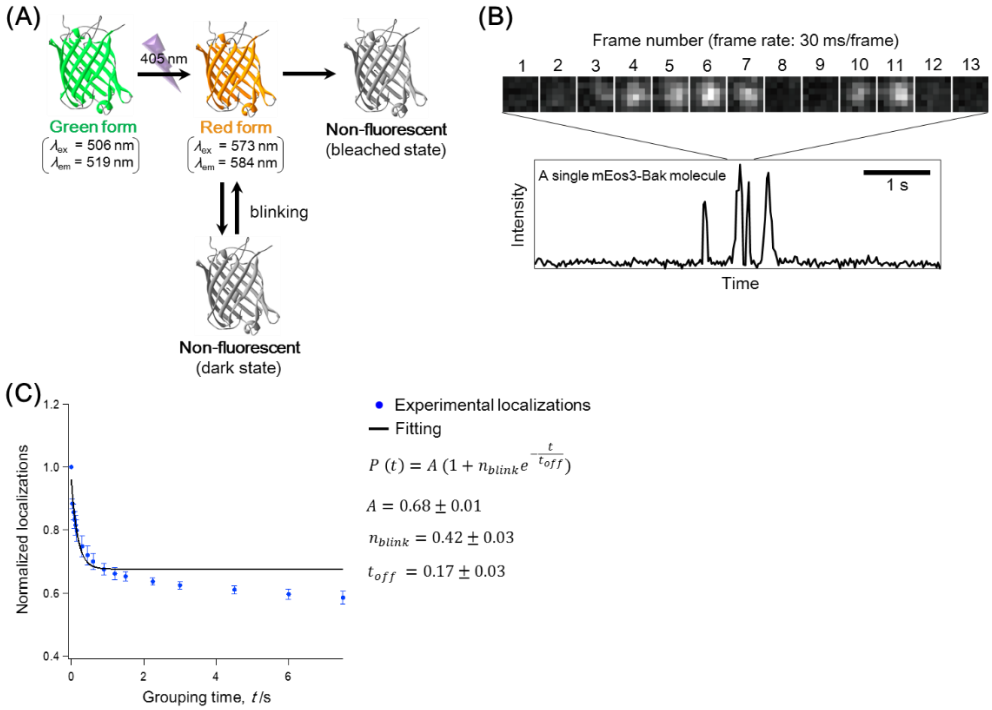

Figure 3-11. Measurement of blinking events of mEos3.

(**A**) Schematics of the fluorescent property of mEos3. Green form of mEos3 is irreversibly converted to the red form upon violet light illumination. In the presence of excitation light, the red form emits the fluorescence and can go either to dark state or to bleached state. Once the molecule become bleached, no fluorescence signal is detected. In contrast, if the red form of mEos3 goes to another non-fluorescent state, the dark state, the fluorescence signal can be detected again by returning to the red form. This phenomenon is observed as blinking. (**B**) Time trace of fluorescence intensity of a photoactivated red form of a single mEos3-Bak molecule in *bak*$^{-/-}$ *bax*$^{-/-}$ MEF transiently expressing mEos3-Bak. The trace showed that a single mEos3 molecule blinked several times and its fluorescence signal lived over multiple consecutive frames before being bleached. The upper part represents the fluorescence images of a single mEos3-Bak molecule detected in the EM-CCD camera. (**C**) The number of localizations as a function of grouping time, *t*, in *bak*$^{-/-}$ *bax*$^{-/-}$ MEF transiently transfected with *mEos3-Bak*. The measured data within the first 1.5 s was fitted by a distribution given by $P(t) = A(1+n_{blink}\,e^{-t/toff})$, where n_{blink} is the mean number of blinking events per molecule and t_{off} is the time the molecule spends in the dark state[18]. Data are represented as mean ± s.d. (n = 3 cells).

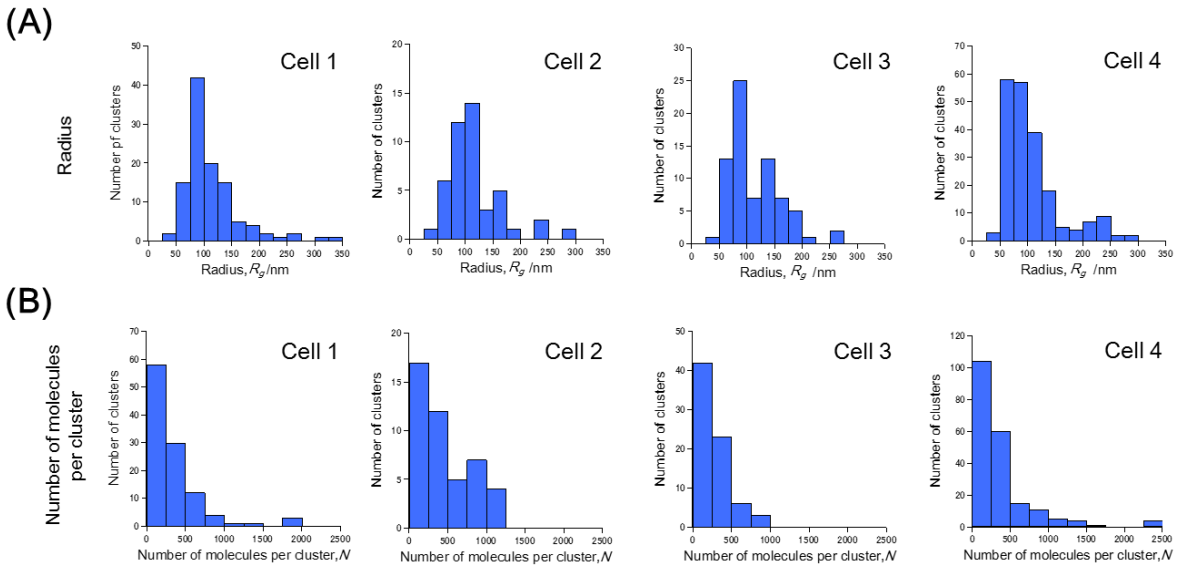

Figure 3-12. Distribution of radius and number of molecules per cluster in each cell.
Distribution of (**A**) radius (R_g) and (**B**) number of molecules per cluster (N) of mEos3-Bak clusters in each cell.

To further examine whether the density of Bak molecules within clusters is similar among individual clusters, I measured the molecular density in each Bak cluster independently of R_g and N. The molecular density (D) in each cluster was calculated by averaging the local densities (**Figure 3-9E**). The value D exhibited a distribution between 3,233 and 10,576 molecules/μm^2, resulting in the mean of 4.75 × 10^3 molecules/μm^2 (**Figure 3-9F**). Because D is 1.55 × 10^3 molecules/μm^2 in a healthy cell (**Figure 3-5B**), the analysis indicated that the density of Bak molecules in a cluster is approximately three times higher than that in a healthy cell. The coefficient of variance in D (0.24) was smaller than that in R_g (0.46) and N (1.02), demonstrating that the distribution of D showed a narrow range as compared to that of R_g and N. The narrow distribution of D indicates a similar density between individual clusters, consistent with the scaling relationship examined by the fractal analysis.

3-3-5. Characterization of Bak mutant clusters.

To further characterize the Bak cluster, I generated two cell lines stably expressing mEos3-labeled Bak mutants: mEos3-BakΔGD (**Figure 3-13**) and mEos3-BakΔN (**Figure 3-14**). BakΔGD lacks two amino acids in the Bcl-2 homology 3 (BH3) domain which is necessary for the induction of apoptosis (**Figure 3-15**)[34]. The deletion did not abrogate mitochondrial localization in the MEF cells (**Figure 3-13C**), but apoptotic function was completely lost (**Figure 3-16**). Intriguingly, mEos3-BakΔGD formed no cluster under the apoptotic condition (**Figure 3-13C**). In addition, a conformational change in BakΔGD, which is requisite for the

formation of a functional cluster, was not observed upon UV stimulation (**Figure 3-17A**). These results suggest that the deletion in the BH3 domain suppressed the activation of Bak and its subsequent clustering, leading to the loss of apoptotic function. The other Bak mutant, BakΔN, lacks 20 amino acids at the N-terminus (**Figure 3-15**). A viability test revealed that mEos3-BakΔN exhibited higher apoptotic activity than that of mEos3-Bak (**Figure 3-16**). The mutant localized uniformly on mitochondria in the unstimulated cells and formed clusters upon apoptotic stimulation (**Figure 3-14C**). Fluorescence recovery after photobleaching (FRAP) analysis revealed that mEos3-BakΔN diffused faster than mEos3-Bak in healthy cells (**Figure 3-18**). Wild-type Bak is known to form a large complex by binding anti-apoptotic proteins under unstimulated conditions[35, 36]. Based on such previous reports, the difference in diffusion rates suggests that mEos3-BakΔN may be more susceptible to apoptotic stimuli because of its low affinity to the anti-apoptotic proteins. The conformational change in BakΔN for its activation during apoptosis was observed from immunostaining analysis (**Figure 3-17B**), indicating that mEos3-BakΔN formed functional clusters responsible for apoptosis upon stimulation.

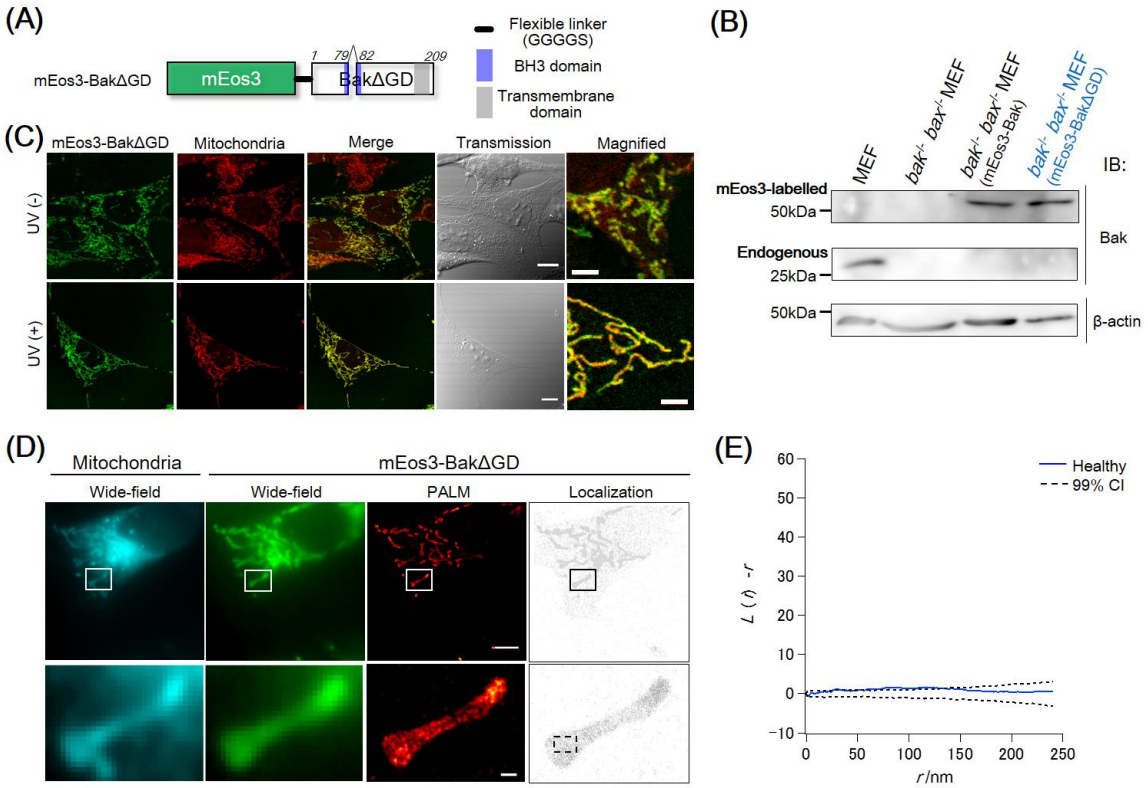

Figure 3-13. Generation of a cell line expressing mEos3-BakΔGD for PALM.

(**A**) Schematic construct of mEos3-BakΔGD. Numbers in italics show the residue of amino acids in Bak. BakΔGD mutant lacks two amino acids (Gly at 80 and Asp at 81), which were located in the BH3 domain (72–86, blue). (**B**) Western blot analysis for investigating the expression of mEos3-BakΔGD in the engineered cell line. The analysis was performed in the same membrane shown in Figure 3-14. (**C**) Fluorescence and transmission images of the cells in the presence or absence of UV irradiation. A dye of MitoTracker CMXRos was used for mitochondrial visualization. Scale bars: 10 μm (Transmission) or 2 μm (Magnified). (**D**) PALM imaging of BakΔGD in a healthy cell. Mitochondria were visualized with MitoTracker Deep Red dye under a wide-field configuration. The boxed regions are enlarged in lower panels. Scale bars: 5 μm (top) or 500 nm (bottom). (**E**) Ripley's K analysis for quantitative measurement of the degree of the spatial distribution of mEos3-BakΔGD under a healthy condition. The analysis was performed in the boxed region (480 nm × 800 nm, dotted line) of a healthy cell shown in (**D**). CI, confidence interval.

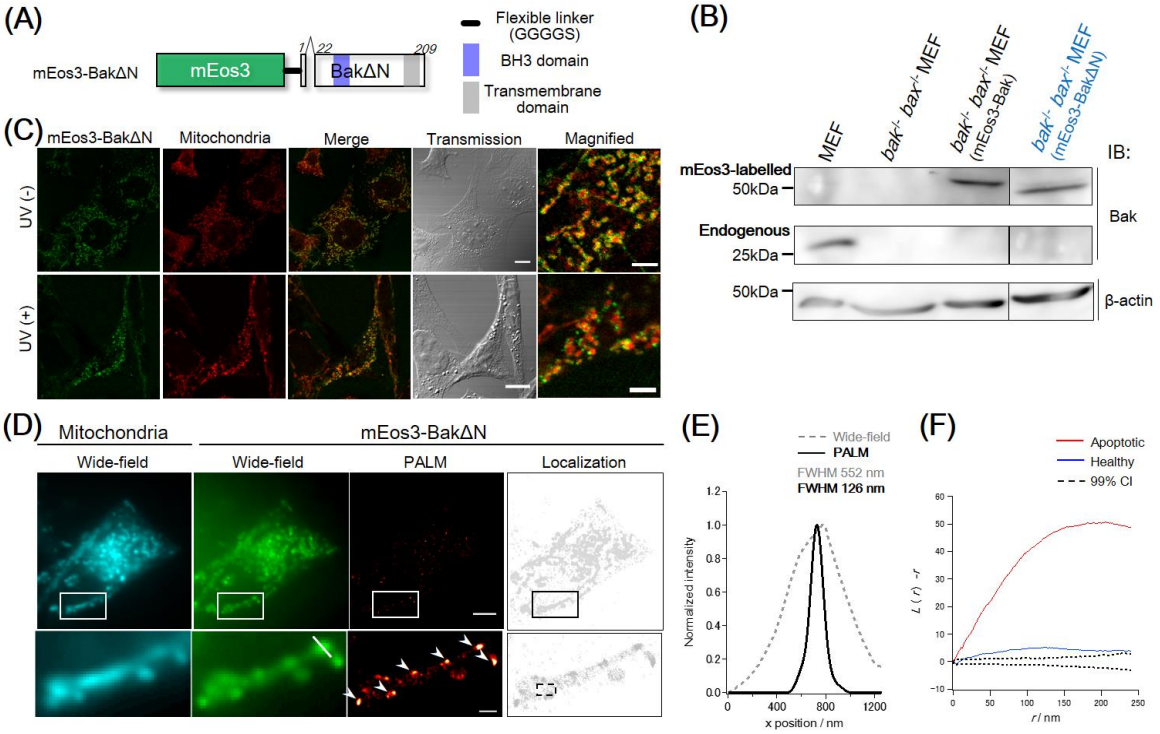

Figure 3-14. Generation of a cell line expressing mEos3-BakΔN for PALM.

(**A**) Schematic construct of mEos3-BakΔN. Numbers in italics show the residue of amino acids in Bak. BakΔN mutant lacks 20 amino acids at the N-terminus. (**B**) Western blot analysis for investigating the expression of mEos3-BakΔN in the engineered cell line. The analysis was performed in the same membrane shown in Figure 3-13. (**C**) Fluorescence and transmission images of the cells in the presence or absence of UV irradiation. MitoTracker CMXRos dye was used as a mitochondrial marker. Scale bars: 10 μm (Transmission) or 2 μm (Magnified). (**D**) PALM imaging of BakΔN clusters in a UV-stimulated cell. Mitochondria were visualized using MitoTracker Deep Red dye under a wide-field configuration. The boxed regions are enlarged (lower panels). Arrows indicate BakΔN clusters. Scale bars: 5 μm (top) or 1 μm (bottom). (**E**) Line-intensity profile from a line on a BakΔN cluster shown in (**D**). The cluster size was estimated by calculating FWHM of the profile. (**F**) Ripley's K analysis for quantitative measurement of the degree of the spatial distribution of mEos3-BakΔN. The analyses were performed in the boxed region (480 nm × 800 nm, black) of an apoptotic cell shown in (**D**) and a healthy cell (not shown). CI, confidence interval.

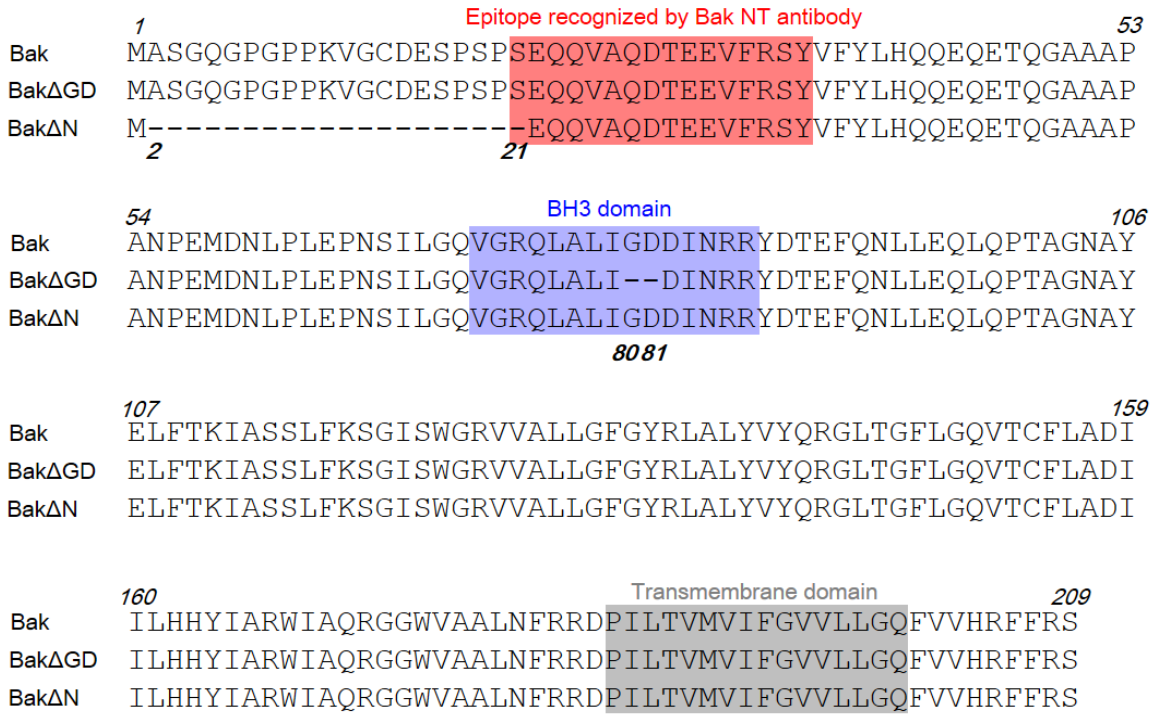

Figure 3-15. Sequences of Bak mutants.

Mouse Bak (wild type) is composed of 209 amino acids. Two (^{80}G^{81}D) and twenty (from ^{2}A to ^{21}S) amino-acid residues were deleted in BakΔGD and BakΔN, respectively. The sequence highlighted in the red box corresponds to the epitope recognized by Bak NT antibody. The deletion in BakΔGD is located in a BH3 domain, which is requisite for the induction of apoptosis[34]. The transmembrane domain indicated by gray box is anchored to the mitochondrial outer membrane, thereby allowing Bak to localize in mitochondria[3].

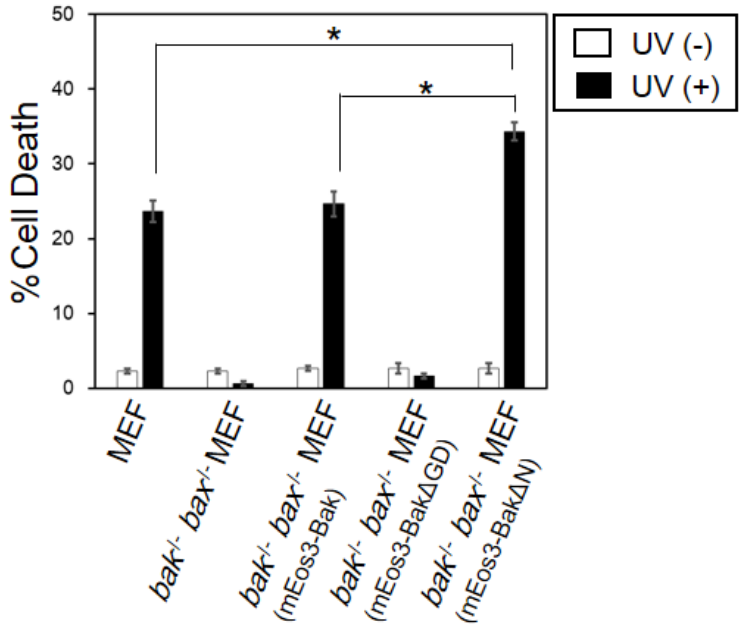

Figure 3-16. Quantification of apoptotic activity of each Bak mutant.

Trypan blue assay was performed. Data are represented as mean ± s.e.m. (n = 3). Statistical analysis was performed using one-way analysis of variance (one-way ANOVA) with the Dunnett's post hoc tests.

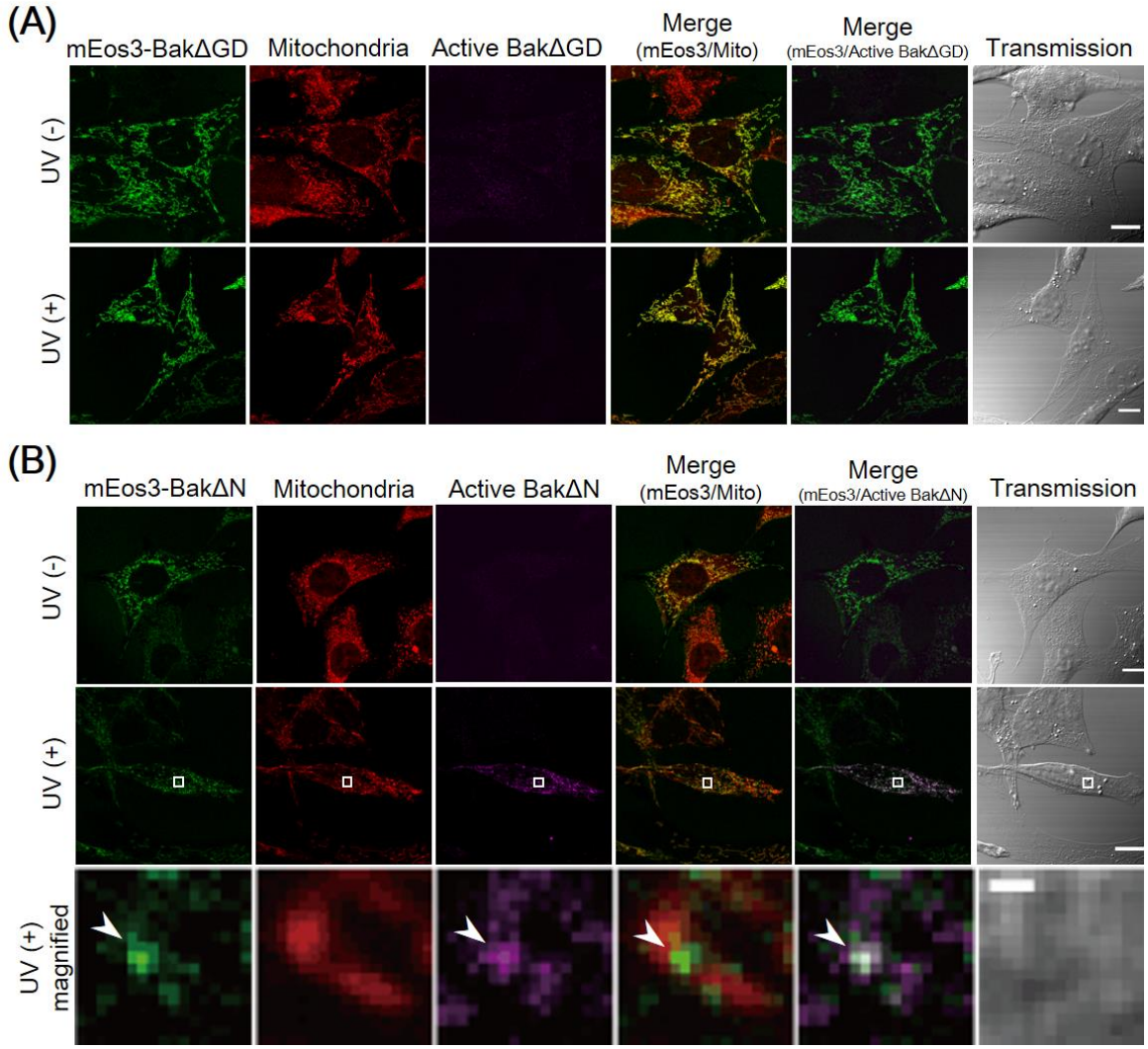

Figure 3-17. Intramolecular conformational change in mEos3-labeled Bak mutants.

(**A**) Immunostaining of the active BakΔGD connected with mEos3 in the cell. Scale bars: 10 μm. (**B**) Immunostaining of the active BakΔN connected with mEos3 in the cell. Magnified images in white boxes (middle) are shown at the bottom. Arrowheads indicate a functional BakΔN cluster. Scale bars: 10 μm (top and middle) or 0.5 μm (bottom).

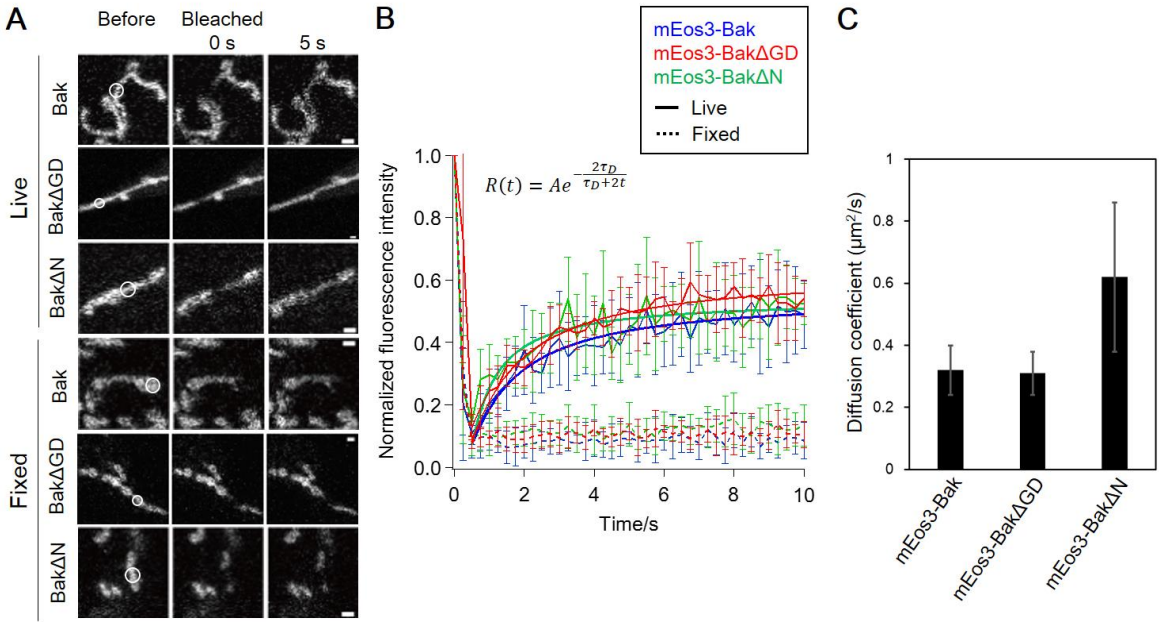

Figure 3-18. FRAP analysis.

(**A**) Fluorescence images obtained at different times during a representative FRAP experiment in cells expressing mEos3-Bak, mEos3-BakΔGD, and mEos3-BakΔN. The region in the circle was photobleached at time 0 s. Measurements of cells fixed with paraformaldehyde were performed as a negative control. Scale bars: 1 μm. (**B**) Fluorescence recovery curves. Each point is represented as mean ± s.d. (n = 6). Data were fitted by Jacobson's equation described in the figure. (**C**) Comparison of diffusion coefficients of mEos3-Bak, mEos3-BakΔGD, and mEos3-BakΔN. Error bars denote 95% confidence interval.

To investigate characteristics of the Bak mutant clusters based on their localization, I observed the BakΔN clusters with PALM at the apoptotic stage (**Figure 3-19**). Subsequently, I identified mEos3-BakΔN localizations constituting clusters using the cluster algorithm (**Figure 3-20**). Quantitative analysis of the identified BakΔN clusters revealed that the radius (R_g) was broadly distributed, 20 nm–199 nm, yielding a mean radius of 82 ± 33 nm (s.d.) (**Figure 3-19B**). The number of molecules per cluster (N) was 18–985, yielding a τ of 191 molecules (**Figure 3-19C**). The fractal analysis of BakΔN clusters revealed a fractal dimension (D_f) of 1.89 ± 0.12 (95% confidence interval) (**Figure 3-19D**). The D_f value of the BakΔN cluster was consistent with that of the wild-type Bak cluster, indicative of a similar density of mEos3-BakΔN molecules within clusters across different sizes. Finally, I measured the molecular density in each BakΔN cluster. The molecular density (D), which was calculated by averaging the local densities, exhibited a distribution between 3,154 and 10,906 molecules/μm^2, resulting in the mean of 4.54 × 10^3 molecules/μm^2 (**Figure 3-19E**). The coefficients of variation were 0.40, 0.90, and 0.21, respectively, in R_g, N, and D, indicating that the distribution of D was confined to a narrower region than that of R_g and N. The homogeneous distribution of the density shows agreement with the scaling relation characterized by D_f. Unlike R_g and N, I found no significant difference in D between Bak and BakΔN clusters (**Figure 3-21** and **Table 3-1**).

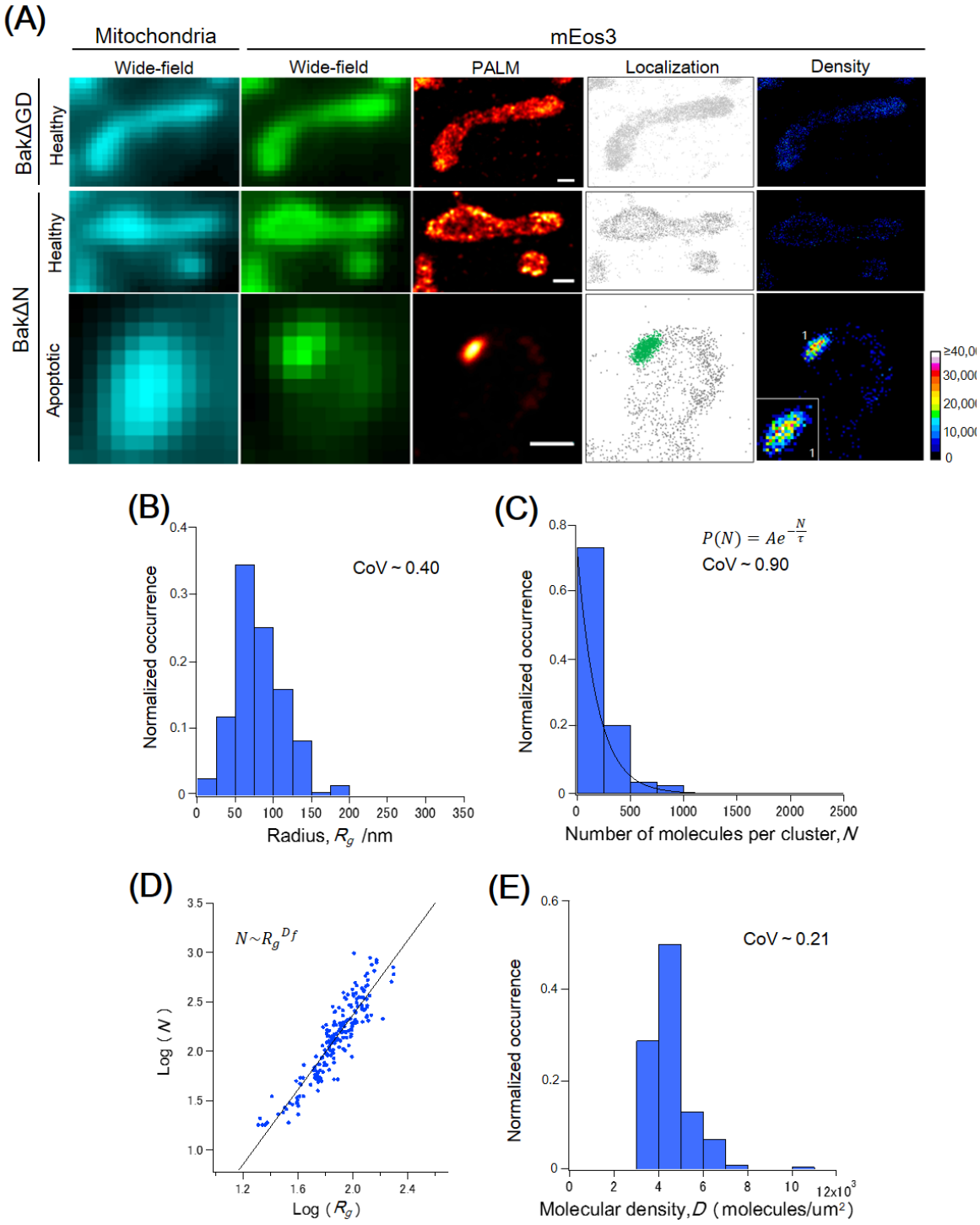

Figure 3-19. Characterization of mEos3-Bak mutant clusters.

(**A**) Images of mitochondria (Wide-field) and mEos3 (Wide-field, PALM, Localization and Density) in a healthy cell and an apoptotic cell expressing mEos3-BakΔGD or mEos3-BakΔN. Localizations identified as a cluster are colored (mEos3, Localization). The color bar indicates the molecular density (molecules/μm^2) in the density maps. A magnified image of a cluster was shown in the inset. Scale bars: 500 nm. (**B**) Normalized histogram of the radii, R_g, of mEos3-BakΔN clusters. (**C**) Normalized histogram of the number of mEos3-BakΔN molecules per cluster, N. The distribution was fitted by single exponential decay. (**D**) Fractal analysis. Linear regression of the plot yields the slope which corresponds to the fractal dimension, D_f. (**E**) Normalized histogram of the molecular densities, D, of mEos3-BakΔN clusters. CoV denotes the coefficient of variation obtained for the respective data. N = 195 clusters from five cells.

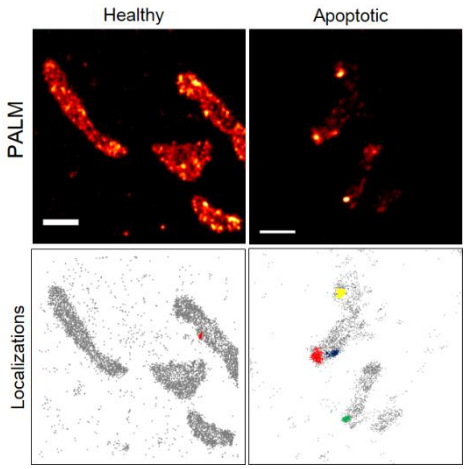

Figure 3-20. A cluster analysis to identify BakΔN clusters using DBSCAN.

PALM images and BakΔN localizations plotted as gray points in the cell lines expressing mEos3-BakΔN. Localizations defined as a cluster by DBSCAN share the same randomly chosen color. Scale bars: 1 μm.

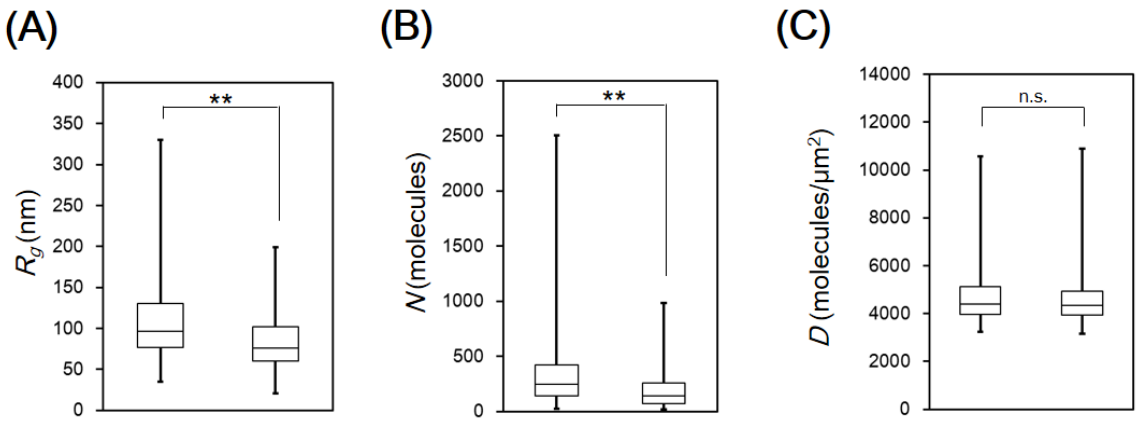

Figure 3-21. Comparison of characteristics between Bak and BakΔN clusters.

(**A**) Box plots of the radius, R_g, of Bak and BakΔN clusters. (**B**) Box plots of the number of molecules per cluster, N, of Bak and BakΔN clusters. (**C**) Box plots of the molecular density, D, of Bak and BakΔN clusters. These plots show the minimum, first quartile, median, third quartile, and maximum. Statistical analyses were performed with the Mann-Whitney test. $P > 0.05$ is indicated as not significant (n.s.). $^{**}P < 0.0001$.

Table 3-1. Summary of characteristics of the Bak and Bak-mutant cluster.

Construct	Radius R_g (nm)	Number of molecules τ (molecules)	Scaling relation D_f	Molecular density D (molecules/μm²)	Analyzed clusters
mEos3-Bak	111 ± 50	344 ± 24	1.80 ± 0.09	(4.75 ± 0.06)×10³	433 (4 cells)
mEos3-BakΔGD	No clusters detected.				
mEos3-BakΔN	82 ± 33	191 ± 5	1.89 ± 0.12	(4.54 ± 0.07)×10³	195 (5 cells)

Radii are represented as mean ± s.d. Densities are represented as mean ± s.e.m. The errors of τ and D_f are the 95% confidence interval obtained from the regression analyses.

3-4. Discussion

I used a PALM-based approach for quantitative characterization of the Bak clusters in terms of the radius and the number of molecules per cluster. Using this approach, I characterized clusters smaller than the diffraction limit (**Figure 3-9B**), which constitutes the vast majority of clusters. In addition, the present approach based on single molecule localization provided insight into the number of molecules per cluster. It has already been reported that only 40% of mEos3 in a cell are detectable by PALM because of the existence of misfolded non-fluorescent proteins[37]. However, this underestimation of mEos3 in the present study does not perturb the estimation of the distribution of the number of molecules per cluster because the degree of underestimation is constant among clusters (**Figure 3-9C**). The distribution was approximately exponential without characteristic size, suggesting that Bak proteins spontaneously oligomerized without an additional mechanism such as regulation by other mitochondrial proteins[11].

Bax, a close homolog of Bak, functions as a similar pro-apoptotic protein via clustering on mitochondria[2]. According to some previous studies[6,7], the number of Bax proteins per cluster varies considerably from 70–250 molecules to 1×10^3–2×10^4 molecules. These values were evaluated with a cell in the presence of endogenous Bax using conventional fluorescence microscopy. To count the Bax proteins, the fluorescence intensity of each cluster was measured. Then the number of fluorescent proteins in each cluster was estimated from a calibration graph using its corresponding fluorescent protein. In contrast to my evaluation of the previous approach, I emphasize that the present approach is more accurate. I replaced endogenous Bak by mEos3-labeled Bak (**Figure 3-1**) and performed *in situ* characterization of Bak clusters without any need for *in vitro* calibration (**Figure 3-9**). Considering the degree of underestimation described above, I estimated that the number of molecules per cluster was from approximately several tens to 6×10^3, whereas 90% of the clusters included fewer than 2×10^3 proteins. The present approach revealed the existence of small clusters comprising several tens of Bak proteins.

The formation of Bak/Bax clusters is primarily responsible for releasing apoptogenic proteins from mitochondria into the cytosol. Despite extensive studies on the mechanism, however, it remains unclear how these clusters permeabilize the mitochondrial outer membrane. Two models have been proposed to explain the mechanism; proteinaceous pore model[38] and lipidic pore model[39]. In the former model, Bak/Bax clusters themselves serve as a channel-like pore on mitochondrial outer membrane. Alternatively, in the lipidic pore model, the cluster formation induces a mechanical tension of the mitochondrial membrane, thereby forming lipidic pores on the membrane. As discussed above, I found that the Bak clusters consisted of approximately several tens to thousands Bak molecules in the cellular milieu. This cluster size was far larger than a typical channel such as that reconstituted into liposome[38]. Furthermore,

the pore-like structure was not observed in the distribution of Bak proteins in each cluster (**Figure 3-9A**, Localization and Density). These results suggest that the Bak cluster does not form a proteinaceous pore but induces a mechanical tension of the membrane, although the possibility of the proteinaceous pore model might still be remained. In addition, I revealed that the molecular density in the Bak clusters was homogeneous among different-size clusters (**Figure 3-9**), which was similar to that in BakΔN clusters (**Figure 3-19** and **Figure 3-21C**). Recently, it has been suggested that several amino acid regions in Bak are inserted into the mitochondrial outer membrane during its clustering, thereby increasing mechanical tension and curvature in the membrane[40,41]. Moreover, biochemical analysis using artificial membranes revealed that the pore size depends on the concentration of Bak proteins on the membrane[42]. Taken together with such previous knowledge, results suggest that the cells maintained low Bak density (1.55×10^3 molecules/μm^2, **Figure 3-5B**) under unstimulated conditions, thereby avoiding the perturbation of the integrity of mitochondrial membrane. Upon UV stimulation, Bak underwent its conformational change and the density increased locally on mitochondria, which was estimated as 4.75×10^3 molecules/μm^2 (**Table 3-1**). The local Bak clusters with the determinant density might engender mechanical stress on the mitochondrial membrane to form the lipidic pore that enabled apoptogenic proteins to be released from mitochondria to the cytosol.

3-5. Conclusion

In summary, I demonstrated an approach based on single-molecule localization to *in situ* characterization of Bak clusters essential to the induction of apoptosis. Directly visualizing each mEos3-labeled Bak in the physiologically relevant cluster with super-resolution accuracy, I demonstrated the existence of clusters smaller than the diffraction limit and quantitatively characterized their size in the cellular milieu. I provided unprecedented insight into the density of Bak proteins in each cluster, revealing that the density is homogeneous among clusters with divergent sizes. In addition, I could not find any pore-like structure of each Bak cluster on mitochondrial membrane with a resolution of 20 nm. My findings suggest that reaching a threshold of the Bak density on mitochondrial outer membrane during its clustering provokes the formation of a lipidic pores responsible for the induction of apoptosis.

References

1. Danial, N. N. & Korsmeyer, S. J. *Cell* **116**, 205–219 (2004).
2. Czabotar, P. E., Lessene, G., Strasser, A. & Adams, J. M. *Nat. Rev. Mol. Cell Biol.* **15**, 49–63 (2014).
3. Dewson, G. *et al. Mol. Cell* **36**, 696–703 (2009).
4. Dewson, G. *et al. Mol. Cell* **30**, 369–380 (2008).
5. Moldoveanu, T. *et al. Nat. Struct. Mol. Biol.* **20**, 589–597 (2013).
6. Zhou, L. & Chang, D. C. *J. Cell Sci.* **121**, 2186–2196 (2008).
7. Nechushtan, A., Smith, C. L., Lamensdorf, I., Yoon, S.-H. & Youle, R. J. *J. Cell Biol.* **153**, 1265–1276 (2001).
8. Betzig, E. *et al. Science* **313**, 1642–1645 (2006).
9. Rust, M. J., Bates, M. & Zhuang, X. *Nat. Methods* **3**, 793–796 (2006).
10. Hess, S. T., Girirajan, T. P. K. & Mason, M. D. *Biophys. J.* **91**, 4258–4272 (2006).
11. Greenfield, D. *et al. PLoS Biol.* **7**, e1000137 (2009).
12. Gunzenhauser, J., Olivier, N., Pengo, T. & Manley, S. *Nano Lett.* **12**, 4705–4710 (2012).
13. Muranyi, W., Malkusch, S., Muller, B., Heilemann, M. & Krausslich, H. G. *PLoS Pathog.* **9**, e1003198 (2013).
14. Endesfelder, U. *et al. Biophys. J.* **105**, 172–181 (2013).
15. Cisse, II *et al. Science* **341**, 664–667 (2013).
16. M. Tokunaga, N. Imamoto, K. Sakata-Sogawa, *Nat. Methods* **5**, 159−161 (2008).
17. M. Renz, B. R. Daniels, G. Vamosi, I. M. Arias, J. Lippincott-Schwartz, *Proc. Natl. Acad. Sci. USA* **109**, E2989−2997 (2012).
18. Annibale, P. Vanni, S. Scarselli, M. Rothlisberger, U. & Radenovic, A. *PLoS One* **6**, e22678 (2011).
19. S.-H. Lee, J. Y. Shin, A. Lee, C. Bustamante, *Proc. Natl. Acad. Sci. USA* **109**, 17436−17441 (2012).
20. L. Niu, J. Yu, *Biophys. J.* **95**, 2009−2016 (2008).
21. Ripley B. D., *J. R. Stat. Soc. Ser. B* **39**, 172−212 (1977).
22. G. L. W. Perry, *Environ. Model. Softw.* **19**, 559−569 (2004).
23. U. Endesfelder, K. Finan, S. J. Holden, P. R. Cook, A. N. Kapanidis, M. Heilemann,

Biophys. *J*. **105**, 172−181 (2013).

24. M. Ester, H.-P. Kriegel, J. Sander, X. Xu, *Second International Conference on Knowledge Discovery and Data Mining (KDD-96)* 226−231 (Munich, Germany, 1996).
25. G. C. Bushell, Y. D. Yan, D. Woodfield, J. Raper, R. Amal, *Adv*. *Colloid Interface Sci*. **95**, 1−50 (2002).
26. Y. Nishida, S. Arakawa, K. Fujitani, H. Yamaguchi, T. Mizuta, T. Kanaseki, M. Komatsu, K. Otsu, Y. Tsujimoto, S. Shimizu, *Nature* **461**, 654−658 (2009).
27. K. Jacobson, Z. Derzko, E. S. Wu, Y. Hou, G. Poste, *J*. *Supramol*. *Struct*. **5**, 565−576 (1976).
28. M. Zhang, H. Chang, Y. Zhang, J. Yu, L. Wu, W. Ji, J. Chen, B. Liu, J. Lu, Y. Liu, J. Zhang, P. Xu, T. Xu, *Nat*. *Methods* **9**, 727−729 (2012).
29. H. Kim, H. C. Tu, D. Ren, O. Takeuchi, J. R. Jeffers, G. P. Zambetti, J. J. Hsieh, E. H. Cheng, *Mol*. *Cell* **36**, 487−499 (2009).
30. G. Dewson, R. M. Kluck, *J*. *Cell Sci*. **122**, 2801−2808 (2009).
31. Thompson, R. E., Larson, D. R. & Webb, W. W. *Biophys*. *J*. **82**, 2775−2783 (2002).
32. D. Baddeley, M. B. Cannell, C. Soeller, *Microsc*. *Microanal*. **16**, 64−72 (2010).
33. Pippa, N., Dokoumetzidis, A., Demetzos, C. & Macheras, P. *Int*. *J*. *Pharm*. **456**, 340–352 (2013).
34. Shimizu, S. & Tsujimoto, Y. *Proc*. *Natl*. *Acad*. *Sci*. *USA* **97**, 577–582 (2000).
35. Cheng, E. H., Sheiko, T. V., Fisher, J. K., Craigen, W. J. & Korsmeyer, S. J. *Science* **301**, 513–517 (2003).
36. Leu, J. I., Dumont, P., Hafey, M., Murphy, M. E. & George, D. L. *Nat*. *Cell Biol*. **6**, 443–450 (2004).
37. Durisic, N., Laparra-Cuervo, L., Sandoval-Alvarez, A., Borbely, J. S. & Lakadamyali, M. *Nat*. *Methods* **11**, 156–162 (2014).
38. Saito, M., Korsmeyer, S. J. & Schlesinger, P. H. *Nat*. *Cell Biol*. **2**, 553–555 (2000).
39. Bleicken, S. *et al*. *J*. *Biol*. *Chem*. **285**, 6636–6647 (2010).
40. Oh, K. J. *et al*. *J*. *Biol*. *Chem*. **285**, 28924–28937 (2010).
41. Westphal, D., Kluck, R. M. & Dewson, G. *Cell Death Differ*. **21**, 196–205 (2014).
42. Bleicken, S., Landeta, O., Landajuela, A., Basanez, G. & Garcia-Saez, A. J. *J*. *Biol*. *Chem*. **288**, 33241–33252 (2013).

Chapter 4

General Conclusion

Key words throughout the dissertation are “microscopy” and “apoptosis”. Microscopy is the methodology to visualize target of interest with microscope. Apoptosis is one of the mechanisms of cell death. Apoptosis is involved in the onset of many fatal diseases including cancer, which drives researchers for the study of this intrinsic mechanism. Microscopy has been a powerful tool for the analysis of apoptosis. However, the study of apoptosis has been hampered by two major limitations of microscopy. First, there have been few methods to observe apoptosis in live multicellular organism. Second, the methodology to quantitatively analyze apoptosis with sufficient spatial resolution in the cellular milieu has been not available. In this doctoral thesis, I describe the development of fluorescent probes to overcome these limitations.

Chapter 2 describes the probe capable of detecting apoptosis as a fluorescence signal in live multicellular organism. The probe is based on spontaneous complementation of GFP fragments, $GFP_{1–10}$ and GFP_{11}. Probe molecules, Smac-GFP_{11} and $GFP_{1–10}$, are expressed in mitochondria and cytosol, respectively. Mitochondrial membrane separates these molecules, which suppresses the background fluorescence under healthy condition. Upon apoptotic stimulation, Smac-GFP_{11} is released into cytosol and complemented with $GFP_{1–10}$ to recover the fluorescence. I demonstrated that this genetically-encoded probe enabled the visualization of apoptotic cells with high signal to background ratio in live animals.

Chapter 3 depicts the probe for Bak cluster critically responsible for the induction of apoptosis. To rigorously quantify the stoichiometry of Bak molecules in each cluster, I developed a cell line expressing a Bak cluster probe in which endogenous Bak was replaced with fluorescent-labeled Bak. I showed that the probe in the cell line was able to visualize physiologically relevant Bak clusters with a resolution of 20 nm. Using the cell line, I characterized the Bak cluster and revealed that the density of Bak molecules was homogeneous among clusters with divergent sizes. I demonstrated that the probe was applicable to quantitatively characterize the Bak cluster *in situ* with a single-molecule level.

In conclusion, I developed fluorescent probes capable of analyzing apoptosis which is otherwise not able to be examined. These probes offer valuable tools to elucidate the detailed mechanism of apoptosis. For example, the apoptosis probe based on spontaneous GFP complementation is applicable to various animals such as mouse. Further application of the probe to mammalian animals will expand our knowledge regarding apoptosis in higher eukaryote. The Bak cluster probe, on the other hand, allows an investigation of correlation between the cluster characteristics and mitochondrial membrane. The investigation will provide unprecedented insight into the enigmatic mechanism how the cluster permeabilizes the mitochondrial membrane to release pro-apoptotic proteins. Prospective applications of the developed probes in this dissertation will lead to a deeper understanding of apoptosis, paving the way for development of novel therapies for apoptosis-related diseases.